NANYANG TECHNOLOGICAL UNIVERSITY

SINGAPORE

ADVANCED ARCHITECTURES OF GAN-BASED LIGHT-EMITTING DEVICES FROM BLUE TO UV

ZHENG HAIYANG

SCHOOL OF ELECTRICAL & ELECTRONIC ENGINEERING

2020

ADVANCED ARCHITECTURES OF GAN-BASED LIGHT-EMITTING DEVICES FROM BLUE TO UV

ZHENG HAIYANG

School of Electrical & Electronic Engineering

A thesis submitted to the Nanyang Technological University
in partial fulfillment of the requirement for the degree of
Doctor of Philosophy

2020

Statement of Originality

I hereby certify that the work embodied in this thesis is the result of original research, is free of plagiarised materials, and has not been submitted for a higher degree to any other University or Institution.

19/08/2019 ....
Date

Zheng Haiyang ....
Zheng Haiyang

Supervisor Declaration Statement

I have reviewed the content and presentation style of this thesis and declare it is free of plagiarism and of sufficient grammatical clarity to be examined. To the best of my knowledge, the research and writing are those of the candidate except as acknowledged in the Author Attribution Statement. I confirm that the investigations were conducted in accord with the ethics policies and integrity standards of Nanyang Technological University and that the research data are presented honestly and without prejudice.

21/08/2019
....
Date

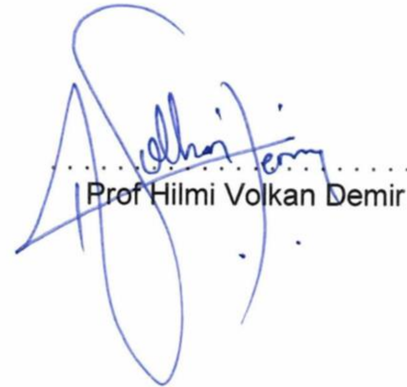

....
Prof Hilmi Volkan Demir

Authorship Attribution Statement

This thesis **does not** contain any materials from papers published in peer-reviewed journals or from papers accepted at conferences in which I am listed as an author.

19/08/2019
Date

Zheng Haiyang
Zheng Haiyang

Acknowledgments

I feel very proud to have had the opportunity to study at Nanyang Technological University in Singapore because of its intensive research excellence and openness to the world. It has been a long journey to this moment in my academic career, and I wish to express my thanks to *LUMINOUS!* Centre of Excellence for providing me with this opportunity to perform my research work on *Advanced Architectures of GaN-Based Light-Emitting Devices from Blue to UV*. Furthermore, I would like to express my appreciation to the following people for supporting my research and making my PhD studies a rewarding experience.

First of all, I wish to acknowledge and express my sincere respect for my PhD supervisor, Professor Hilmi Volkan Demir, for providing me with the opportunity to pursue my PhD studies. His patience in supervising me has focused my interest on the scientific and engineering world, and his extensive and professional knowledge in the scientific field has inspired me. Moreover, his extensive guidance and support have led me toward the completion of my PhD studies step by step.

Second, I wish to express my sincere gratitude to Dr. Tan Swee Tiam for his kind support throughout my PhD studies. His excellent support in our metal-organic chemical vapour deposition (MOCVD) growth team has guaranteed the running and growth of the MOCVD system for my research purposes. Moreover, I wish to thank Dr. Tsai Ping Chieh for his expertise in the MOCVD growth process. His professional knowledge has helped me throughout my research experiments. Moreover, I would like to thank Dr. Vijay Kumar Sharma for his kind support of my research on cathodoluminescent ultraviolet devices.

Third, working with a strong and collaborative MOCVD team at the LUMINOUS! Research Centre has been an excellent opportunity; therefore, I wish to extend thanks to my other MOCVD team members including Mr. Zhang Xueliang, Dr. Lu Shunpeng, and Dr. Zhang Yiping for their assistance in troubleshooting and fabrication optimizations. My LED device would not have worked properly without their training me in photolithography, reactive-ion etching, inductively coupled plasma, e-beam deposition, rapid thermal annealing, and photoluminescence and electroluminescence measurements.

Furthermore, I would like to give special thanks to my mother and father, and even more to my wife, for their moral support and encouragement throughout my PhD studies.

Finally, I wish to express my appreciation for the generous financial support I have received from Nanyang Technological University for my PhD studies.

Table of Contents

Acknowledgments I

Table of Contents .... - 3 -

Summary .... - 6 -

List of Figures .... - 10 -

List of Tables .... - 15 -

Chapter 1 Introduction .... - 16 -

1.1 Introduction to GaN-based LEDs .... - 16 -

1.1.1 History of GaN-based LEDs .... - 16 -

1.1.2 Basics of GaN-based LEDs .... - 20 -

1.1.3 Advantages of GaN-based LEDs—blue to UV .... - 24 -

1.1.4 Application of GaN-based LEDs—blue to UV .... - 24 -

1.2 Background knowledge .... - 26 -

1.2.1 Properties of Ga(In, Al)N material .... - 26 -

1.2.2 Polarization effects and the quantum-confined Stark effect in GaN-based LEDs .... - 30 -

1.2.3 Efficiency of GaN-based LEDs .... - 34 -

1.2.4 Efficiency road map and technical issues of GaN-based UV LEDs .... - 36 -

1.3 Challenges, motivation, and objectives .... - 39 -

1.4 Major contributions of the thesis .... - 40 -

1.5 Organization of the thesis .... - 42 -

Chapter 2 Epitaxial Growth and Wafer-Level Characterization of GaN-Based Blue and Near-UV LEDs .... - 44 -

2.1 Metal-organic chemical vapor deposition system .... - 44 -

2.2 Epitaxial growth and layer structure of GaN LED wafers .... - 47 -

2.2.1 GaN blue LED Wafer .... - 47 -

2.2.2 GaN near-UV LED wafers .... - 48 -

2.3 Wafer-level characterization .... - 49 -

2.3.1 GaN blue LED Wafer .... - 49 -

2.3.2 GaN near-UV LED wafers .... - 50 -

2.4 Summary .... - 55 -

Chapter 3 Device Fabrication and Chip-Level Characterization of GaN-Based Blue and Near-UV LEDs .... - 56 -

3.1 Device fabrication .... - 56 -

3.1.1 Device structures for lateral, flip-chip, and vertical GaN-based blue and near-UV LEDs .... - 56 -

3.1.2 Fabrication process for lateral GaN-based blue and near-UV LEDs .... - 57 -

3.1.3 Fabrication process for flip-chip GaN-based blue and near-UV LEDs .... - 58 -

3.1.4 Fabrication process for vertical GaN-based blue and near-UV LEDs .... - 59 -

3.2 Chip-level characterization of lateral, flip-chip, and vertical GaN-based blue and near-UV LEDs .... - 61 -
3.2.1 GaN-based blue LEDs .... - 61 -
3.2.2 GaN-based UV LEDs .... - 63 -
3.3 Discussion .... - 66 -
Chapter 4 Efficiency Droop and Electrical Characteristic Dependence of GaN-Based Blue LEDs on Chip Mesa .... - 68 -
4.1 Introduction .... - 68 -
4.2 Experiments .... - 69 -
4.3 Results and discussion .... - 70 -
4.4 Summary .... - 75 -
Chapter 5 Near-UV Micro-LEDs for Enhanced Efficiency and Reduced Droop - 77 -
5.1 Introduction .... - 77 -
5.2 Experimental and simulation conditions .... - 78 -
5.3 Results and discussion .... - 80 -
5.4 Summary .... - 90 -
Chapter 6 Influence of AlN Composition in Quantum Barriers on the Performance of Near-UV LEDs .... - 91 -
6.1 Introduction .... - 91 -
6.2 Experiments .... - 92 -
6.3 Results and discussion .... - 93 -
6.3.1 GaN-delta-AlGaN QBs for QB6–QB8 .... - 93 -
6.3.2 AlN step composition QBs for QB6–QB8 .... - 97 -
6.3.3 GaN/AlGaN last QB .... - 101 -
6.3.4 Extending AlN composition from QB6–QB8 to QB1–QB5 .... - 105 -
6.3.5 AlN composition graded AlGaN ILs .... - 109 -
6.4 Summary .... - 113 -
Chapter 7 Correlation Between Carrier Diffusion and Efficiency of Deep-UV Structures Based on E-Beam Pumped Deep-UV MQWs .... - 115 -
7.1 Introduction .... - 115 -
7.2 Experiments .... - 117 -
7.3 Results and discussion .... - 119 -
7.4 Summary .... - 127 -
Chapter 8 Conclusions and Recommendations .... - 128 -
8.1 Conclusion .... - 128 -
8.2 Recommendations for further research .... - 130 -
Author's contributions to literature .... - 132 -
Bibliography .... - 132 -

Summary

In the past few decades, remarkable progress has been made in the research and development of gallium nitride (GaN)-based light sources. Among them, GaN-based blue and ultraviolet (UV) light-emitting diodes (LEDs) have achieved great success and attracted considerable attention in a wide range of applications. GaN-based blue LEDs are highly efficient and reliable visible light sources, and thus have found broad applications in solid-state lighting (SSL), automobile headlights, LED displays, liquid crystal display (LCD) backlights, flash units, and compact projectors and scanners. Also, GaN-based UV LEDs are energy efficient and robust UV light sources, and they have great potential in UV curing, counterfeit detection, UV lithography, photocatalysis, air purification and tanning (UV-A or near-UV), medical phototherapy, protein analysis and drug discovery (UV-B), water/air disinfection, and bioagent-sensing (UV-C or deep-UV). In this thesis, leveraging on the GaN-based blue LED materials and device platform that we developed, we extended our work beyond the visible and ventured into the ultraviolet. We aimed to establish a robust GaN-based UV LED materials and device platform through designing and implementing novel structural and device solutions, including size effect, Al incorporated quantum barriers (QBs), and electron beam (e-beam) pumping.

For this thesis, various GaN-based LED structures were designed, grown, and fabricated for the performance enhancement of the InGaN/(Al)GaN blue and near-UV LEDs. InGaN/(Al)GaN multiple-quantum-well (MQW) blue and near-UV LED epitaxial wafers were grown along the c-axis on sapphire wafers with designed structures using a commercial metal-organic chemical vapour deposition (MOCVD) system. Furthermore, the fabrication process of these LED devices was designed, optimized

through iteration, and tested on the grown epitaxial LED wafers. Based on this platform, novel structures have been designed for the performance enhancement of InGaN/(Al)GaN blue and near-UV LEDs.

It is well known that shrinking the size of an LED device will improve its radiative recombination rate, enhance its light extraction efficiency (LEE), and reduce its current-spreading and thermal effects. In this study, the size effect has been investigated on the efficiency droop of the InGaN/GaN blue LEDs. We compared the efficiency droop trends for GaN-based blue LED devices with different mesa dimensions, and found that the external quantum efficiency (EQE) and wall-plug efficiency (WPE) droop started at higher current injections for an LED device with a larger mesa dimension because of the reduced injection current density; however, the EQE droop began at a lower injection current density for an LED with a larger mesa dimension because of increased current crowding. Moreover, the WPE droop began at a slightly higher injection current density as the mesa dimension of the LED was further enlarged. This was ascribed to the shallow slope of the I-V characteristics around the position of the EQE peak. Furthermore, the series resistance (SRRS) and ideality factor were derived for LED devices with different mesa dimensions by fitting the measured I-V characteristics to a diode I-V model. Both the SRRS and ideality factor decreased as the mesa dimension of the LEDs increased. This suggested that the I-V characteristics of a real LED approached that of an ideal LED as its mesa dimension increased.

In addition, size shrinking has proved effective at reducing current crowding, enhancing the output power density, and increasing the power roll-over current density in UV micro-LEDs. We systematically investigated the size effect on the electrical and optical

characteristics of these near-UV micro-LEDs. We observed that the EQE was enhanced as the size decreased, but such enhancement became marginal as the size reduced from $50 \times 50\ \mu m^2$ to $25 \times 25\ \mu m^2$. Moreover, the efficiency droop reduction reversed as the size decreased from $50 \times 50\ \mu m^2$ to $25 \times 25\ \mu m^2$. In addition to the current spreading effect, the strain relaxation, sidewall defect, and p-contact resistance were found to be the root causes of the size effect. We demonstrated that the $50 \times 50\ \mu m^2$ micro-LED exhibited the highest performance in terms of the efficiency and droop, which provided the design rules of thumb for near-UV LEDs.

The structure of MQWs is a critical factor determining the performance of a near-UV LED. As the emission wavelength shifts from blue to near-UV, the *In* incorporation in the MQWs decreases, and thus the quantum wells (QWs) become shallow. This weakens the carrier confinement of the MQWs and increases the carrier overflow. For these reasons, incorporating *Al* into the quantum well barriers (QBs) is necessary, which increases the confinement of the MQWs. Therefore, in this thesis, the influence of Al composition in the AlGaN QBs on the performance of near-UV LEDs was systematically studied by adopting multilayer QB structures. In addition to the electrical characteristics, both the efficiency levels and efficiency droop trends were compared for LED devices with different QB structures.

As the emission wavelength shifts further from the near-UV to the deep-UV, the performance of the GaN-based UV LEDs is held back by the low doping efficiency of p-AlGaN (p-type doped AlGaN), and thus non-Ohmic p-contact and electron leakage. Therefore, e-beam pumping has been proposed as a potential technique for the next-generation of UV light sources with great environmental and economic benefits. We

started developing e-beam pumped cathodoluminescence (CL) structures in the near-UV range and applied our findings to deep-UV CL structures based on e-beam pumping. The cathodoluminescence characteristics of the near-UV InGaN/AlGaN MQW structures with 8, 10, 15, and 20 QWs were systematically studied and the acceleration voltages were recorded when the CL power efficiency (PE) reached the maximum value. We established the relationship between the acceleration voltage and QW number by introducing the contribution to MQW region's absorption from carriers generated within the diffusion length below the MQWs. This new understanding will help in designing efficient CL-based UV structures. In the work conducted for this thesis, we also tested and demonstrated GaN-based deep-UV structures, which is critical for the development of efficient deep-UV emitters.

The findings of this thesis from blue to UV contribute to both materials level and device level understanding of III-N material systems and device platforms for applications ranging from artificial lighting to curing and disinfection.

List of Figures

Figure 1-1 Summary of the key nodes for the efficient blue LED. .... - 17 -

Figure 1-2 Close-up images of a (a) bare and (b) packaged GaN-based blue LED. .... - 21 -

Figure 1-3 (a) Schematic sketch of a GaN LED under forward bias. Schematic diagram of carrier injection and radiative recombination in (b) homojuction and (c) DH LEDs. .... - 22 -

Figure 1-4 Schematic of carrier injection and radiative recombination of (a) MQW blue GaN LEDs and (b) MQW UV GaN LEDs. .... - 23 -

Figure 1-5 Advantages of GaN LEDs—blue to UV. .... - 24 -

Figure 1-6 Application of GaN LEDs—beyond the blue. .... - 25 -

Figure 1-7 Potential applications of UV-A-UV-C LEDs. .... - 26 -

Figure 1-8 Prime unit cell of wurtzite crystal structure bulk Ga(In, Al)N with lattice constants of a and c, and c-axis points to the Ga face (0001). .... - 27 -

Figure 1-9 (a) Bandgap energy vs. lattice constant of an $Al_xIn_yGa_{1-x-y}N$ material system with (b) GaN and (c) AlN energy band diagrams on each side. ...... - 29 -

Figure 1-10 (a) Spontaneous polarization of Ga-face and N-face GaN grown bulk GaN substrate. Piezoelectric polarization of (b) Ga-face and (c) N-face Al(In)GaN grown on GaN substrate or buffer layer. .... - 32 -

Figure 1-11 Calculated spontaneous, piezoelectric, and total polarization for AlGaN and InGaN ternary alloys grown on relaxed GaN. .... - 33 -

Figure 1-12 Schematic band diagram of active regions: (a) w/o (b) w/ polarization field. .... - 34 -

Figure 1-13 (a) Current EQE status of GaN-based UV LEDs, and (b) WPE road map projection for 265, 285, and 310 nm GaN-based UV LEDs. .... - 37 -

Figure 1-14 Schematic structure of a typical flip chip GaN-based UV LED below 360 nm with major technical issues that limit its efficiency. .... - 39 -

Figure 2-1 Schematic sketch of the MOCVD growth process for III-nitrides. - 45 -

Figure 2-2 Schematic of a MOCVD system .... - 46 -

Figure 2-3 (a) AIXTRON® MOCVD system and (b) susceptor holding wafers in the reactor chamber. .... - 46 -

Figure 2-4 Eptitaxial growth process flow for GaN-based blue LED wafers: (a) sapphire nitridation, (b) amorphous GaN deposition, (c) crystlization, (d) GaN island growth & coalescence, and growth of (e) u-GaN, (f) n-GaN and InGaN/GaN MQWs, (g) AlGaN EBL, and p-GaN and p^+-GaN layers. .... - 48 -

Figure 2-5 (a) Photograph of our GaN blue LED epi-wafer under direct current injection; (b) EL spectrum of the blue LED under different current injections; (c) peak emission wavelength mapping; and (d) FWHM mapping of the LED wafer. .... - 50 -

Figure 2-6 (a) QW peak emission wavelength and (b) FWHM obtained from EL and PL spectra as a function of the QW growth temperature; (c) FWHM extracted from (a) and (b) as a function of peak wavelength. .... - 52 -

Figure 2-7 (a) EL spectrum of the near-UV LED with a peak emission wavelength of 394.6 nm, (b) peak emission wavelength mapping and (c) FWHM mapping of the UV LED wafer. .... - 54 -

Figure 2-8 EL spectrum of the near-UV LED with a peak emission wavelength of 387.5 nm, (b) peak emission wavelength mapping, and (c) FWHM mapping of the UV LED wafer. .... - 54 -

Figure 2-9 EL spectrum of the near-UV LED with a peak emission wavelength of 378.4 nm, (b) peak emission wavelength mapping, and (c) FWHM mapping of the UV LED wafer. .... - 55 -

Figure 3-1 Schematic structural sketch of (a) lateral, (b) flip chip, and (c) vertical LED devices. .... - 56 -

Figure 3-2 Fabrication process flow for a lateral LED device: (a) bare wafer cleaning, (b) CSL deposition, (c) mesa definition, (d) passivation deposition, (e) electrode definition, and (f) N and P contact formation. .... - 58 -

Figure 3-3 Fabrication process flow for a flip-chip LED device: (a) bare wafer cleaning, (b) mirror deposition, (c) mesa definition, (d) passivation deposition, (e) electrode definition, and (f) N and P contact formation. .... - 59 -

Figure 3-4 Fabrication process flow for a vertical LED device: (a) bare wafer cleaning, (b) isolation etching, (c) mesa definition, (d) mirror definition, (e) passivation definition, (f) copper plating and P contact formation, (g) sapphire laser liftoff (LLO), and (h) u-GaN etching & N contact formation. .... - 60 -

Figure 3-5 (a) Spectrum of a lateral 06 × 13 mil^2 GaN-based blue LED with a peak emission wavelength of 455 nm, (b) current dependent LOP and I-V characteristics for the lateral blue LED device on wafer after fabrication, (c) EQE of the lateral device (inset: the fabricated 06 × 13 mil^2 lateral blue LED device on wafer). .... - 62 -

Figure 3-6 (a) Current dependent LOP and I-V characteristics for a flip-chip GaN-based blue LED device on wafer after fabrication, (b) EQE of the flip chip device (inset: the fabricated 20 × 40 mil^2 flip-chip LED device on wafer). ... - 63 -

Figure 3-7 (a) Current dependent LOP and I-V characteristics for a vertical GaN-based blue LED device on wafer after fabrication, (b) EQE of the vertical LED device (inset: the fabricated 45 × 45 mil^2 vertical LED device on wafer). .... - 63 -

Figure 3-8 (a) Spectrum of a lateral 07 × 09 mil^2 GaN-based near-UV LED with a peak emission wavelength of 393 nm, (b) L-I-V characteristics for the lateral near-UV LED device after fabrication, (c) EQE of the LED device (inset: the fabricated 07 × 09 mil^2 LED device). .... - 64 -

Figure 3-9 (a) L-I-V characteristics for a flip-chip 15 × 30 mil^2 GaN-based 395 nm LED device after fabrication, (b) EQE of the LED device (inset: the fabricated 15 × 30 mil^2 LED device). .... - 65 -

Figure 3-10 (a) L-I-V characteristics for a vertical 43 × 43 mil^2 GaN-based 395

nm LED device after fabrication, (b) EQE of the LED device. .... - 65 -

Figure 3-11 (a) Spectrum of a lateral 07 × 09 mil^2 GaN-based near-UV LED with a peak emission wavelength of 384 nm, (b) L-I-V characteristics for the lateral near-UV LED device after fabrication, (c) EQE of the LED device. .. - 66 -

Figure 4-1 Nomalized EQE as a function of (a) injection current and (b) injection current density for the 08 × 20 mil^2, 10 × 30 mil^2, and 20 × 40 mil^2 blue LED samples. Normalized WPE as a function of (c) injection current and (d) injection current density for the three LED samples. .... - 71 -

Figure 4-2 (a) Injection current and (b) injection current density positions of the EQE and WPE peaks as a function of the chip mesa area ratio for the 08 × 20 mil^2, 10 × 30 mil^2, and 20 × 40 mil^2 blue LED samples .... - 72 -

Figure 4-3 (a) Differential resistance (DFRS) as a function of injection current for the 08 × 20 mil^2, 10 × 30 mil^2, and 20 × 40 mil^2 blue LED samples; (b) fitted series resistance (SRRS) and ideality factor as a function of mesa area ratio for the three LED samples. .... - 74 -

Figure 5-1 Forward voltage as a function of the injection current density for (a) experimental measurement and (b) numerical simulation of the micro-LEDs with increasing mesa side lengths. .... - 80 -

Figure 5-2 (a) Schematic micro-LED structure with current spreading and (b) corresponding equivalent circuit. .... - 81 -

Figure 5-3 Re-simulated forward voltage as a function of the injection current density with p-contact resistance considered. .... - 84 -

Figure 5-4 LOPD and EQE as a function of the injection current density for (a) experimental measurement and (b) numerical simulation of the micro-LEDs with increasing mesa side lengths. .... - 85 -

Figure 5-5 Re-simulated LOPD and EQE as a function of the injection current density with (a) strain relaxation and (b) strain relaxation plus sidewall defect considered. .... - 88 -

Figure 5-6 Simulated (a) electron concentration, (b) hole concentration and (c) radiative recombination along the MQWs under an injection current density of 200 A/cm^2. .... - 89 -

Figure 6-1 Schematics of the studied near-UV LED structures with different QB structures for QB6-QB8: Reference device used GaN as QBs; Device A adopted GaN-delta-AlGaN QBs with AlGaN grown at a TMAl flow of 5 sccm; and Device B used a similar QBs structure but with AlGaN grown at a TMAl flow of 10 sccm. .... - 93 -

Figure 6-2 Schematic energy band diagrams for (a) Reference device, (b) Device A; and (c) Device B. .... - 94 -

Figure 6-3 Measured (a) forward voltage and (b) LOPD and EQE as a function of injection current density for the Reference device, Device A, and Device B. .- 97 -

Figure 6-4 Schematics of the studied near-UV LED structures with different QB structures for QB6–QB8: Reference device used GaN-delta-AlGaN QBs

with AlGaN grown at a TMAl flow of 5 sccm; Device A adopted AlN step composition QBs with AlGaN grown at a TMAl flow of 5 sccm; Device B used similar QBs but with AlGaN grown at a TMAl flow of 10 sccm; and Device C used AlGaN QBs with AlGaN grown at a TMAl flow of 5 sccm. .... - 98 -

Figure 6-5 Schematic energy band diagrams for (a) Reference device, (b) Device A, (c) Device B, and (d) Device C. .... - 99 -

Figure 6-6 Measured (a) forward voltage and (b) LOPD and EQE as a function of injection current density for the Reference device, Device A, Device B, and Device C. .... - 101 -

Figure 6-7 Schematics of the studied near-UV LED structures with different QB structures for the last QB: Reference device used GaN last QB; Device A adopted GaN/AlGaN last QB with AlGaN grown at a TMAl flow of 5 sccm in the last 130 s; and Device B used similar last QB but with AlGaN grown in the last 330 s. .... - 102 -

Figure 6-8 Schematic energy band diagrams for (a) Reference device, (b) Device A; and (c) Device B.. - 103 -

Figure 6-9 Measured (a) forward voltage and (b) LOPD and EQE as a function of injection current density for the Reference device, Device A, and Device B. .- 105 -

Figure 6-10 Schematics of the studied near-UV LED structures with different QB structures: Reference device used AlGaN as QBs for QB6-QB8; Device A adopted AlN step composition QBs with AlGaN grown at a TMAl flow of 5 sccm for QB3–QB5 and AlGaN QBs for QB6–QB8; and Device B used the AlGaN QB structure with AlGaN grown at a TMAl flow of 5 sccm for QB1–QB8.. .... - 106 -

Figure 6-11 Schematic energy band diagrams for (a) Reference device, (b) Device A, and (c) Device B.. - 107 -

Figure 6-12 Measured (a) forward voltage and (b) LOPD and EQE as a function of injection current density for the Reference device, Device A, and Device B. .... - 109 -

Figure 6-13 Schematics of the studied near-UV LED structures with different QB structures: Reference device used the AlGaN QB structure with AlGaN grown at a TMAl flow of 5 sccm for QB1–QB8; Device A incorporated AlN composition graded AlGaN ILs with graded AlGaN ILs grown at temperature ramp up from QWs to QBs for QB6–QB8; Device B also incorporated AlN composition graded AlGaN ILs but with graded AlGaN ILs grown both at a temperature ramp up from QWs to QBs and ramp down from QBs to QWs for QB6–QB8; and Device C incorporated AlN composition graded AlGaN ILs with graded AlGaN ILs grown at a temperature ramp up from QWs to QBs for QB2 to the last QB. .... - 110 -

Figure 6-14 Schematic energy band diagrams for (a) Reference device, (b) Device A, (c) Device B, and (d) Device C. .... - 111 -

Figure 6-15 Measured (a) forward voltage and (b) LOPD and EQE as a function of injection current density for the Reference device, Device A, Device

B, and Device C.. - 113 -

Figure 7-1 Schematic of (a) CL measurement setup, (b) InGaN/AlGaN MQW structures on sapphire substrate and (c) system setup. .... - 118 -

Figure 7-2 Measured CL spectra as a function of acceleration voltage for the MQW structure with eight pairs of QWs at irradiated current of 5 μA. .... - 120 -

Figure 7-3 (a) Measured CL PE as a function of acceleration voltage at an irradiated current of 50 μA for the four MQW structures with 8, 10, 15, and 20 pairs of QWs, and (b) extracted maximum PE and turning acceleration voltages as a function of QW number. .... - 121 -

Figure 7-4 (a) Simulated absorbed energy as a function of acceleration voltage for the MQW structure with eight pairs of QWs. The vertical dashed line marks the bottom of the MQWs; (b) simulated depth profiles of the cumulative absorbed energy from the MQWs' top....................................... - 122 -

Figure 7-5 (a) Simulated absorbed energy as a function of acceleration voltage for the MQW structure with eight pairs of QWs with and without diffusion lengths, and (b) turning acceleration voltage as a function of diffusion length… ....- 123 -

Figure 7-6 (a) Simulated depth profiles of the cumulative absorbed energy from the MQWs' top at acceleration voltages of 5, 8, 9, and 10 kV. The first vertical dashed line marks the depth of the MQWs and the rest extends an additional 120, 160, and 200 nm in diffusion length, respectively; (b) extracted cumulative absorbed energy at these locations for acceleration voltages of 5, 8, 9, and 10 kV.. - 124 -

Figure 7-7 (a) Simulated absorbed energy as a function of acceleration voltage for the MQW structure with 8, 10, 15, and 20 pairs of QWs with diffusion length, and (b) extracted turning acceleration voltage as a function of QW number along with the experimental data from Figure 7-1 (b). .... - 125 -

Figure 7-8 Measured CL light output power and PE as a function of irradiated power for the 280 nm deep-UV reference and etched wafer samples. ...... - 126 -

List of Tables

Table 1-1 Significant milestones in the history of GaN-based LEDs that led to white LEDs. .... - 16 -

Table 1-2 Brief research development of GaN-based UV LEDs.................. - 17 -

Table 1-3 Lattice constants and bandgap energies of bulk wurtzite Ga(In, Al)N and ternary alloys. .... - 28 -

Chapter 1 Introduction

1.1 Introduction to GaN-based LEDs

1.1.1 History of GaN-based LEDs

In the past few decades, remarkable progress has been made in the research and development of gallium nitride (GaN)-based light sources.[1-21] Table 1-1[1] lists a brief overview of significant milestones in the history of GaN-based light-emitting diodes (LEDs), which ultimately led to the demonstration of the first high efficiency white LEDs. Figure 1-1[1] presents a summary of key nodes for the inventions and development that led to efficient blue LEDs.

Table 1-1 Significant milestones in the history of GaN-based LEDs that led to white LEDs.[1]

Material	Year	Achievement	Reference
GaN	1969	GaN epitaxial layer by HVPE	Maruska and Tieljen (1969)
	1973	First blue Mg-doped GaN MIS LED	Maruska, Stevenson, and Pankove (1973)
	1983	High quality GaN using AlN buffer by MBE	Yoshida, Misawa, and Gonda (1983)
	1985	High quality GaN using AlN buffer by MOCVD	Amano *et al.* (1986)
	1989	p-type GaN using LEEBI (low hole concentration) First p-n homojunction GaN LED Invention of two-flow MOCVD	Amano *et al.* (1989) Nakamura, Harada, and Seno (1991)
	1991	GaN growth using GaN buffer by MBE High quality GaN using GaN buffer by MOCVD	Lei *et al.* (1991) Nakamura (1991) and Nakamura, Mukai, and Senoh (1992)
	1992	p-type GaN using thermal annealing (high hole concentration) Discovery of hydrogen passivation	Nakamura, Mukai, Senoh, and Iwasa (1992) Nakamura *et al.* (1992)
InGaN	1972	InGaN growth using electron beam plasma	Osamura *et al.* (1972) and Osamura, Naka, and Murakami (1975)
	1989	InGaN growth by MOCVD	Nagatomo *et al.* (1989)

	1992	InGaN layers with RT band-to-band emission	Nakamura and Mukai (1992)
	1994	Efficient blue InGaN DH LED (1 Candela)	Nakamura, Senoh, and Mukai (1993), and Nakamura, Mukai, and Senoh (1994)
	1995	Efficient yellow, green, and blue InGaN DH QW LEDs First pulsed violet InGaN DH MQW LDs	Nakamura *et al.* (1995a, 1995b) Nakamura *et al.* (1996b)
	1996	First CW violet InGaN DH MQW LDs Commercialization of white LEDs using InGaN DH blue LEDs	Nakamura *et al.* (1996a) Bando *et al.* (1996)

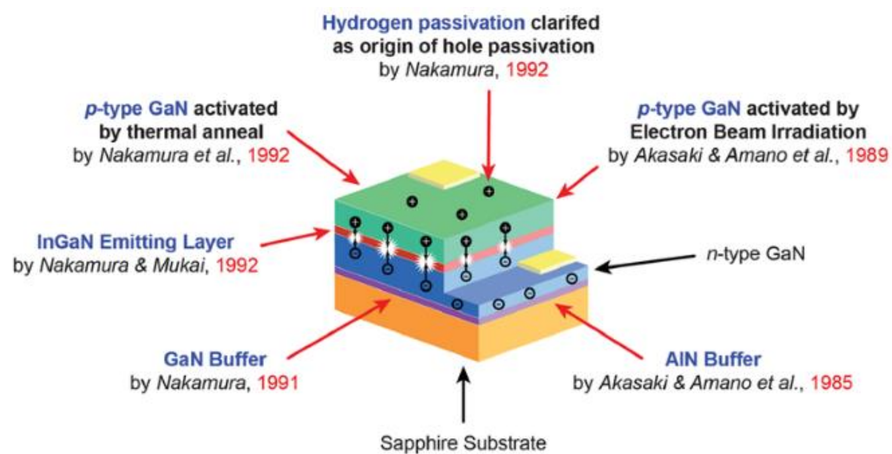

Figure 1-1 Summary of the key nodes for the efficient blue LED.[1]

Table 1-2 Brief research development of GaN-based UV LEDs.

Active region	Year	Advancement	Reference
InGaN	1993	400–425 nm emission	Nakamura *et al.*, 1993a, b, 1994
	1998	InGaN/AlGaN DH and 371 nm emission	Mukai *et al.*, 1998
AlGaN	1998	353.6 nm emission and 13 μW @ 20 mA	Han *et al.*, 1998

	2000	SiC substrate, Mg-doped GaN/AlGaN superlattice hole conductive layer, and 333.0 nm emission	Kinoshita *et al.*, 2000
	2001	Thick bulk GaN substrate, 352 nm emission, and ≥ 3 mW @ 100 mA	Nishida *et al.*, 2001
	2004	Sapphire substrate, 269 nm emission, and EQE 0.32% @ 10mA DC	Adivarahan *et al.*, 2004
	2007	Low TDD AlN buffers on sapphire substrates and 231–261 nm emission	Hirayama *et al.*, 2007
InAlGaN	2009	Quaternary InAlGaN MQWs and 280–284 nm emission	Hirayama *et al.*, 2009
AlGaN	2010	MQB EBL, AlN/sapphire template, and 250–262 nm emission	Hirayama *et al.*, 2010
	2011	Single crystal AlN (sublimation method), 260 nm emission, and 9.2mW @ 100 mA	Grandusky *et al.*, 2011
	2012	Single crystal AlN (HVPE) layer on PVT AlN substrate, 268 nm emission, and 28 mW @ 250 mA	Kinoshita *et al.*, 2012
	2012	10-μm-thick high-quality AlN layer, Mg doped p-AlGaN top contact layer, UV reflective p-metal, 278 nm emission, and EQE 10.4% @ 20 mA	Shatalov *et al.*, 2012

	2013	Transparent p-AlGaN contact layer, highly reflective Ni (1nm)/Al p-type electrode, and 265–288 nm emission	Maeda *et al.*, 2013

As shown in Table 1-2, the invention of the first GaN-based UV LED can be traced back to 1993 and had an InGaN active region emitting at wavelengths ranging from 400 to 425 nm.[2] In 1998, Mukai *et al.* reported the design of an early GaN-based UV LED with an InGaN/AlGaN double heterostructure (DH) emitting at 371 nm.[3] As for GaN-based UV LEDs that emit at wavelengths shorter than 360 nm, they have AlGaN or $Al_xGa_{1-x}N/Al_yGa_{1-y}N$ multiple quantum well (MQW) active regions. In 1998, Han *et al.* reported a GaN-based quantum well UV LED with a peak emission at 353.6 nm and a light output power 13 μW with current injection of 20 mA.[4] In 2000, Kinoshita *et al.* demonstrated a GaN-based UV LED grown on a silicon carbide (SiC) substrate with $Al_{0.03}Ga_{0.97}N/Al_{0.25}Ga_{0.75}N$ MQWs and an Mg-doped GaN/AlGaN superlattice (SL) hole conductive layer emitting at 333 nm.[5] In 2001, Nishida *et al.* reported a GaN-based UV LED grown on thick bulk GaN substrate with a light output power exceeding 3 mW at a current injection of 100 mA and peak emission of 352 nm.[6] In 2004, Adivarahan *et al.* demonstrated a GaN-based UV LED grown over sapphire substrate with a peak emission of 269 nm and external quantum efficiency (EQE) of 0.32% at 10 mA of direct current (DC) pump.[7] In 2007, Hirayama *et al.* reported AlGaN MQW LEDs grown on low-threading dislocation density (TDD) aluminum nitride (AlN) buffers on sapphire substrates with emissions ranging from 231 to 261 nm.[8] In 2009, Hirayama *et al.* demonstrated quaternary InAlGaN MQW UV LEDs with emissions in the range of 280–284 nm.[9]

In 2010, Hirayama *et al.* realized a high-electron injection efficiency (EIE) AlGaN MQW LED with emissions of 250–262 nm grown on an AlN/sapphire template, which they achieved through introducing a multi-quantum barrier (MQB) as an electron blocking layer (EBL).[10] In 2011, Grandusky *et al.* developed a pseudomorphic UV LED grown on a single-crystal AlN substrate using the sublimation method; it had an emission of 260 nm and light output power of 9.2 mW at a 100-mA current injection.[11] In 2012, Kinoshita *et al.* demonstrated a GaN-based UV LED grown on a single-crystal AlN substrate prepared by growing a thick hydride vapor phase epitaxy (HVPE) AlN layer on physical vapor transport (PVT) AlN substrate; it had an emission of 268 nm and light output power of 28 mW at a 250-mA current injection.[12] In the same year, Shatalov *et al.* reported an AlGaN MQW LED with enhanced internal quantum efficiency (IQE) and light extraction efficiency (LEE). The IQE was improved by introducing a 10-μm-thick high-quality AlN layer to reduce the TDD, and the LEE was boosted by introducing an Mg doped p-AlGaN top contact layer and UV reflective p-metal. This allowed the LED's EQE to reach 10.4% at a 20-mA current injection and the emission peaked at 278 nm.[13] In 2013, Maeda *et al.* also demonstrated an LEE-enhanced AlGaN MQW LED using a similar structure.[14]

1.1.2 Basics of GaN-based LEDs

GaN-based LEDs are electroluminescent devices. The first efficient GaN blue LED was created by Nakamura *et al.* in 1993.[15] Figure 1-2 presents close-up images of (a) bare and (b) packaged GaN-based blue LEDs.[1]

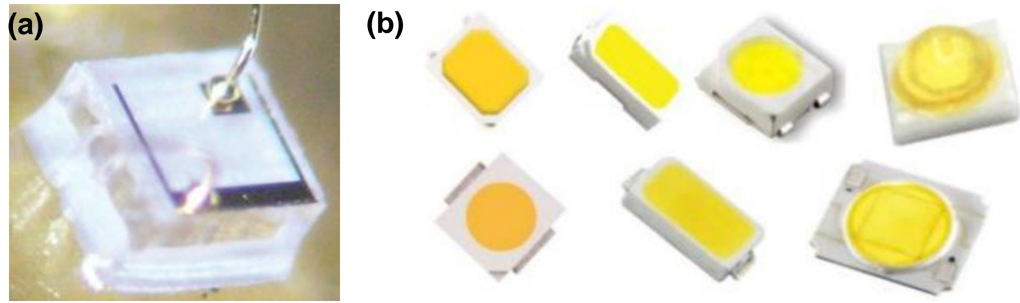

Figure 1-2 Close-up images of (a) bare[1] and (b) packaged GaN-based blue LEDs.

The basic structure of a GaN LED is composed of an active/emitting layer sandwiched by n-type and p-type GaN layers which are abundant in electrons and holes, respectively, as shown in Figure 1-3 (a).[1] Under forward bias, electrons and holes are injected into the active/emitting layer from the cladding layers and recombine radiatively, transferring their energy to emitted photons. As a result, these photons end up with energy equal to the bandgap of the active-layer material. However, as shown in Figure 1-3 (b), the electrons and holes diffuse into the opposite conductive-type regions and distribute over a distance within their diffusion length; their concentration decreases exponentially because of carriers recombining as they diffuse.[1] As a result, for a homojunction LED, carriers recombine along a large distance with decreasing concentrations, yielding low radiative recombination rates and thus low efficiency in a homojunction LED. Therefore, LEDs with higher efficiency contain a DH structure, which consists of a narrow-bandgap active layer sandwiched by two wide-bandgap barrier layers, as shown in Figure 1-3 (c).[1] In the DH structure LEDs, Most carriers injected into the active layer will be essentially confined in the well created by heterojunction potential abruption, which is determined by conduction or valence band offsets between the two bandgap materials. As a result, carriers recombine only within the thickness of the well rather than the region of carrier's carrier diffusion lengths.

Therefore, radiative efficiency increases significantly as the carrier concentration increases in the active region, thereby yielding a much higher radiative recombination rate, and thus higher efficiency of the LEDs.

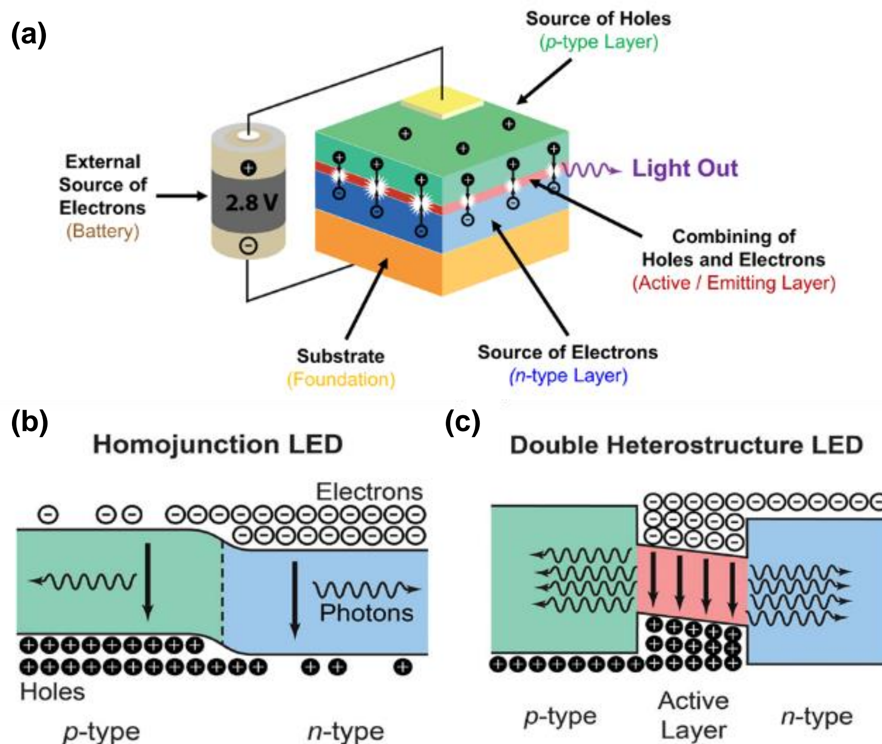

Figure 1-3 (a) Schematic sketch of a GaN LED under forward bias. Schematic diagram of carrier injection and radiative recombination in (b) homojunction and (c) DH LEDs.[1] [Ref. 1]

However, DH LEDs suffer severe carrier overflow.[16] Carriers escape from the active region at high current injections. Furthermore, the femi level rises with an increasing number of carriers being injected into the active region and even to the top of the barrier at sufficiently high carrier injection. As the injection current further increases, the optical density saturates because of carriers flooding into the active region. This issue is more severe in LEDs with a small-volume active region, particularly single quantum wells. Therefore, high power LEDs typically feature an MQW active region and a large chip size. As shown in Figure 1-4 (a),[17] the MQW active region comprises alternating

layers of wide and narrow bandgap semiconductor materials such as GaN and $In_xGa_{1-x}N$. Once the electrons and holes are injected into the MQWs from the n-type and p-type GaN injection layers respectively, they diffuse along the active region and fall into the quantum wells with decreasing carrier concentrations. As a result, the electrons and holes are confined in isolated quantum wells, which reduces the carrier concentration in a single quantum well, and thus also the carrier overflow. Therefore, most of the carriers injected into the active region recombine and emit photons, yielding a higher radiative efficiency.

With $In_xGa_{1-x}N/GaN$ MQWs, GaN-based LED emission can cover the whole visible spectrum, even UV-A with wavelengths above 360 nm. However, for even shorter wavelengths, finding wider-bandgap quantum wells and barriers to confine the injected carriers is necessary. Therefore, $Al_xGa_{1-x}N/Al_yGa_{1-y}N$ MQWs' structure is widely accepted as the active region of GaN-based UV LEDs and their emission can reach as deep as 200 nm, which is roughly the bandgap of AlN, as shown in Figure 1-4 (b).

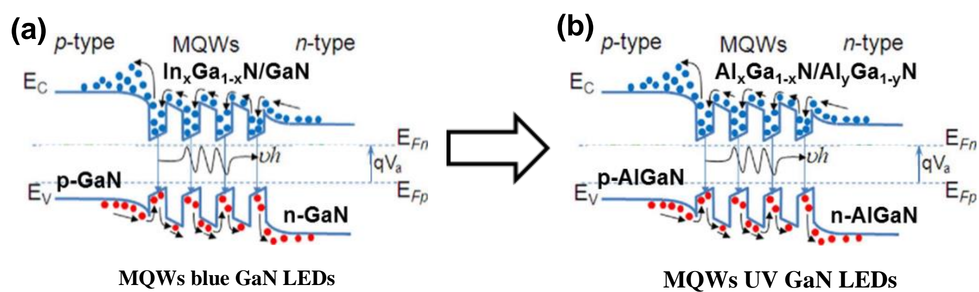

Figure 1-4 Schematic of carrier injection and radiative recombination of (a) MQW blue GaN LEDs[17] and (b) MQW UV GaN LEDs.

1.1.3 Advantages of GaN-based LEDs—blue to UV

GaN-based white LEDs are replacing conventional incandescent and fluorescent lamps as the next-generation solid state lighting (SSL) solution. This is because of their unparalleled advantages, including high brightness, high energy conversion efficiency, low cost, shock resistance, durability, compact size, and fast response compared with incandescent and fluorescent lamps,[18] as shown in Figure 1-5. Similarly, GaN-based UV LEDs are set to replace conventional UV lamps. They are superior because of their low power consumption, short standby time, low thermal dissipation, narrow spectrum, and compact size over conventional UV lamps, and they are more environmentally friendly,[19] as shown in Figure 1-5. Moreover, compared with conventional UV lamps, they exhibit extended life spans, more stable output light intensity, and greater control flexibility.[19] Therefore, GaN UV LEDs are expected to continue to replace conventional UV light sources in the UV market and have a dominant market share in the future.

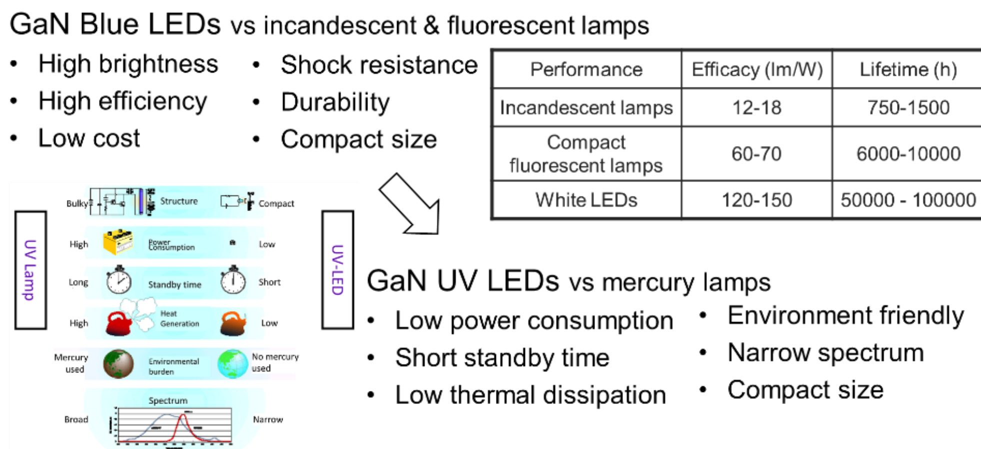

Figure 1-5 Advantages of GaN LEDs—blue to UV.[18,19]

1.1.4 Application of GaN-based LEDs—blue to UV

GaN-based blue and UV LEDs have achieved great success and attracted considerable attention in a wide range of applications, as illustrated in Figure 1-6 and Figure 1-7. GaN-based blue LEDs emit blue rays with a spectrum in the range of 450–480 nm. They

are highly efficient and reliable visible light sources. As such, they can be found in diverse applications such as in indicators, SSL, automobile headlights, three dimensional (3D) LED displays, liquid crystal display (LCD) backlights, flash units, compact projectors, and compact scanners.[20-21] As for UV LEDs, their emission wavelengths extend from 200 to 400 nm. UV radiation is subdivided into UV-A (315–400 nm), UV-B (280–315 nm), and UV-C (100–280 nm), which can penetrate the Earth's atmosphere and are partially and mostly absorbed by the Ozone layer.[22] GaN-based UV LEDs are energy efficient and robust UV light sources, and thus have potential applications in UV curing, counterfeit detection, UV lithography, photocatalysis, air purification, and tanning (UV-A); medical phototherapy, protein analysis, and drug discovery (UV-B); and water/air disinfection and bioagent sensing (UV-C).[23-24] With continual advancements in the research and development of GaN-based blue and UV LEDs, such LEDs have been used to replace conventional light sources.

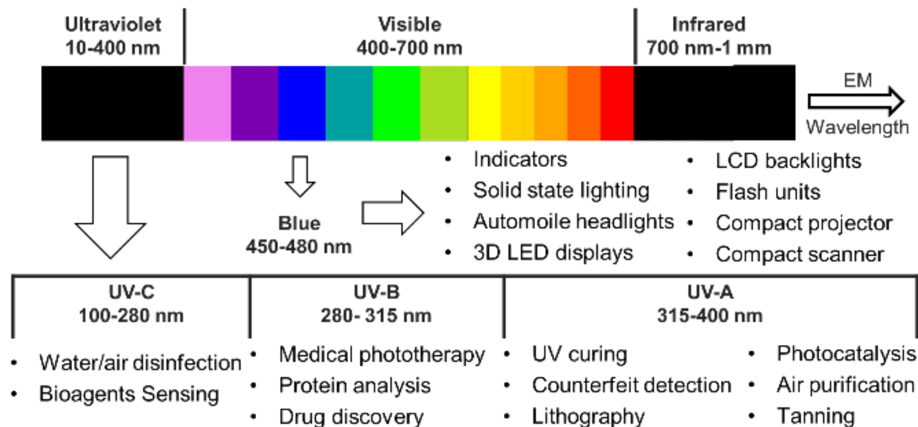

Figure 1-6 Application of GaN LEDs—beyond the blue.[20-24]

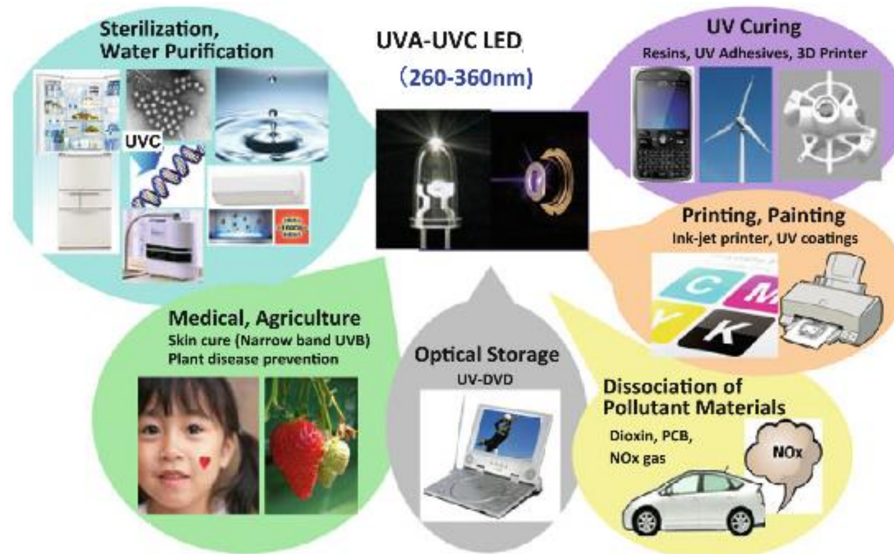

Figure 1-7 Potential applications of UV-A-UV-C LEDs.[23-24]

1.2 Background knowledge

1.2.1 Properties of Ga(In, Al)N material

The great success of GaN-based blue and UV LEDs originates from the unique physical properties of GaN as well as its ternary alloys InGaN and AlGaN. GaN is a binary III-nitride compound semiconductor, as are InN and AlN. Under ambient conditions, bulk Ga(In, Al)N has three crystal structure forms, namely wurtzite, zincblende, and rock salt, but only the wurtzite structure is thermodynamically stable, as shown in Figure 1-8.[25-26] The structure consists of intertwined hexagonal sublattices of Ga(In, Al) and N atoms, offset along the *c* axis by 5/8 of the length of *c*. Bi-atomic close packed planes of Ga(In, Al) and N stack in an *ABAB*… sequence along the *c*-axis. Lattice constants and bandgap energies of bulk wurtzite Ga(In, Al)N are listed in Table 1-3,[25-26] as are those of their ternary alloys. The lattice constants of composition-dependent $In_xGa_{1-x}N$ and $Al_xGa_{1-x}N$ alloys follow Vegard's law:[25-26]

$$a_{In_xGa_{1-x}N} = xa_{InN} + (1-x)a_{GaN} \quad (1\text{-}1)$$

$$a_{Al_xGa_{1-x}N} = xa_{AlN} + (1-x)a_{GaN} \quad (1\text{-}2)$$

where a_{InN}, a_{AlN}, and a_{GaN} are lattice constants of InN, AlN, and GaN, respectively, and x is a molar fraction of InN or AlN. Their fundamental bandgap energies are calculated from empirical expressions as follows:[25-26]

$$E_{In_xGa_{1-x}N}(x) = xE_{InN} + (1-x)E_{GaN} - b_{InGaN}x(1-x) \quad (1\text{-}3)$$

$$E_{Al_xGa_{1-x}N}(x) = xE_{AlN} + (1-x)E_{GaN} - b_{AlGaN}x(1-x) \quad (1\text{-}4)$$

where E_{InN}, E_{AlN}, and E_{GaN} are the bandgap energies of InN, AlN, and GaN, respectively, and b_{InGaN} and b_{AlGaN} is bowing parameter accounting for the bowing nonlinearity of the composition-dependent energy bandgap curves.

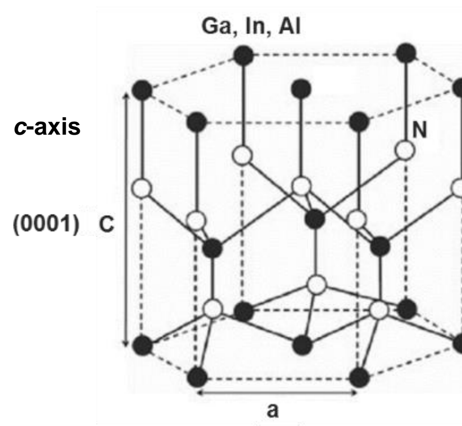

Figure 1-8 Prime unit cell of wurtzite crystal structure bulk Ga(In, Al)N with lattice constants of *a* and *c*, and *c*-axis points to the Ga face (0001).[25-26]

As shown in Table 1-3, at room temperatures, the bandgap energy is 3.425 eV (0.77 eV, 6.28 eV) for Ga(In, Al)N, respectively, and ternary alloys; bandgap energies can be calculated using Equations (1-3) and (1-4). Therefore, emissions from $In_xGa_{1-x}N$ LEDs can cover the whole visible spectrum, whereas those from $Al_xGa_{1-x}N$ LEDs span most of the UV spectrum and can reach as deep as 200 nm, as shown in Figure 1-9.[27-28] Moreover, UV emissions from $Al_xGa_{1-x}N$ LEDs can be precisely controlled simply by engineering the bandgap energy of $Al_xGa_{1-x}N$ through composition modulation.

Table 1-3 Lattice constants and bandgap energies of bulk wurtzite Ga(In, Al)N and ternary alloys.[25-26]

Wurtzite (300 K)	GaN	InN	AlN	$In_xGa_{1-x}N$	$Al_xGa_{1-x}N$
Lattice constant (Å)	a = 3.191 c = 5.185	a = 3.545 c = 5.703	a = 3.112 c = 4.982	$a = 3.545x + 3.191(1-x)$ $c = 5.703x + 5.185(1-x)$	$a = 3.112x + 3.191(1-x)$ $c = 4.982x + 5.185(1-x)$
Energy bandgap (eV)	3.425	0.77	6.28	$0.77x + 3.425(1-x) – 1.43x(1-x)$	$6.28x + 3.425(1-x) – x(1-x)$

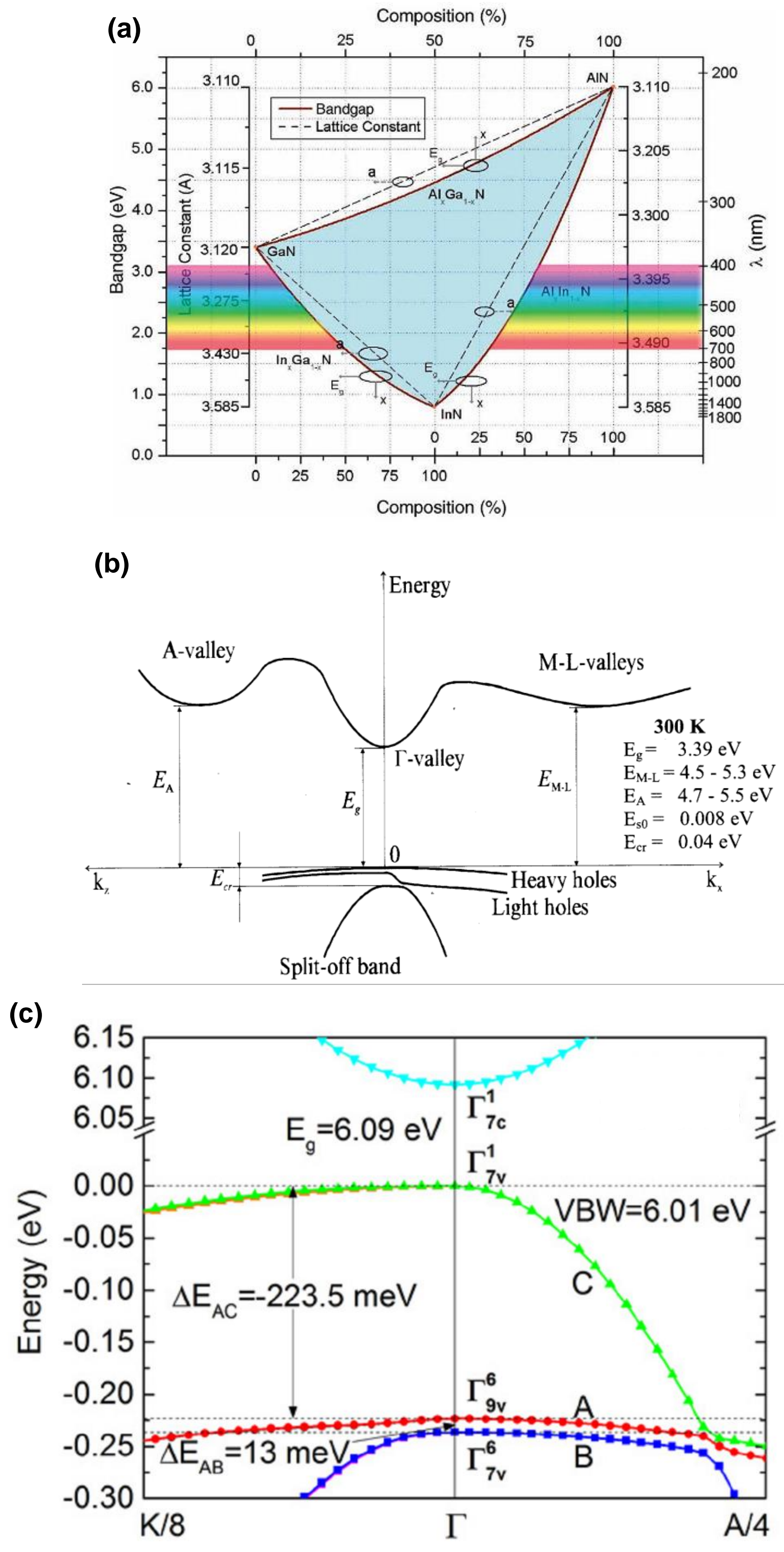

Figure 1-9 (a) Bandgap energy vs. lattice constant of an $Al_xIn_yGa_{1-x-y}N$ material system with[25-26] (b) GaN[27] and (c) AlN[28] energy band diagrams on each side.

1.2.2 Polarization effects and the quantum-confined Stark effect in GaN-based LEDs

GaN-based LEDs are commonly grown epitaxially layer by layer along the c-axis of wurtzite Ga(Al)N. Along this orientation, pronounced polarization charges accumulate at each of the two opposite surfaces of a layer. These polarization charges originate from the partial ionicity of the covalent bond between Ga(In, Al) and N atoms and noncentrosymmetric wurtzite crystal structures.[25-26] Therefore, these polarization charges are divided accordingly into spontaneous and piezoelectric polarization charges. As shown in Figure 1-10 (a),[29] alternating layers of Ga and N atoms are arranged along the *c*-axis. The covalent bonds connecting Ga and N atoms are partially ionic, and thus the geometric centers of positive and negative charges are separated, leading to spontaneous polarization along the *c*-axis. The polarity of the polarization charges is opposite to the orientation of the *c*-axis. When single bonds are directed from Ga to N atoms, the polarity is referred to as the Ga-polarity and the *c*-axis points from the N-face to the Ga-face, or (0001), whereas the spontaneous polarization points to (000-1).[25-26] Otherwise, the polarity is N-polarity and spontaneous polarization points to (0001). The Ga-face carries negative charges, whereas the N-face is positively charged. According to Bernardini and Fiorentini, spontaneous polarization of Al(In)GaN ternary alloys is formulated as[25-26]

$$P^{sp}_{In_xGa_{1-x}N} = xP^{sp}_{InN} + (1-x)P^{sp}_{GaN} - b_{In_xGa_{1-x}N}x(1-x) \qquad (1\text{-}5)$$

$$P^{sp}_{Al_xGa_{1-x}N} = xP^{sp}_{AlN} + (1-x)P^{sp}_{GaN} - b_{Al_xGa_{1-x}N}x(1-x) \qquad (1\text{-}6)$$

where P^{sp}_{InN}, P^{sp}_{AlN}, and P^{sp}_{GaN} are the spontaneous polarization of InN, AlN, and GaN, and b_{InGaN} and b_{InGaN} are the bowing parameters accounting for the nonlinearity in composition-dependent spontaneous polarization.

A ternary epitaxial layer grown along the c-axis on a thick relaxed GaN buffer (substrate) can experience in-plane biaxial compressive or tensile strain caused by lattice mismatch between the epitaxial layer and buffer, as shown in Figure 1-10 (b) and (c).[16] Furthermore, AlGaN (InGaN) film experiences tensile (compressive) strain when it is grown on GaN buffer because of its smaller (larger) top lattice compared with that of the buffer, which leads to piezoelectric polarization. Such polarization points from the N-face to the Ga-face for InGaN, whereas it points from the Ga-face to the N-face for AlGaN epilayer. Surface charges, and thus internal electric fields, are also indicated in the figure. The internal electric field is antiparallel to piezoelectric polarization, and the magnitude of piezoelectric polarization follows Vegard's law:[25-26]

$$P^{pe}_{In_xGa_{1-x}N} = xP^{pe}_{InN}\left(\varepsilon_{In_xGa_{1-x}N}\right) + (1-x)P^{pe}_{GaN}\left(\varepsilon_{In_xGa_{1-x}N}\right) \qquad (1\text{-}7)$$

$$P^{pe}_{Al_xGa_{1-x}N} = xP^{pe}_{AlN}\left(\varepsilon_{Al_xGa_{1-x}N}\right) + (1-x)P^{pe}_{GaN}\left(\varepsilon_{Al_xGa_{1-x}N}\right) \qquad (1\text{-}8)$$

$$\varepsilon_{In_xGa_{1-x}N} = \frac{a_{In_xGa_{1-x}N} - a_{GaN}}{a_{GaN}} \qquad (1\text{-}9)$$

$$\varepsilon_{Al_xGa_{1-x}N} = \frac{a_{Al_xGa_{1-x}N} - a_{GaN}}{a_{GaN}} \qquad (1\text{-}10)$$

where $P^{pe}_{InN}\left(\varepsilon_{In_xGa_{1-x}N}\right)$ and $P^{pe}_{GaN}\left(\varepsilon_{In_xGa_{1-x}N}\right)$ are piezoelectric polarization for InN and GaN under in-plane biaxial strain experienced by the InGaN ternary alloy, and similarly, $P^{pe}_{AlN}\left(\varepsilon_{Al_xGa_{1-x}N}\right)$, $P^{pe}_{GaN}\left(\varepsilon_{Al_xGa_{1-x}N}\right)$, and $\varepsilon_{Al_xGa_{1-x}N}$ are piezoelectric polarization for the AlGaN ternary alloy.

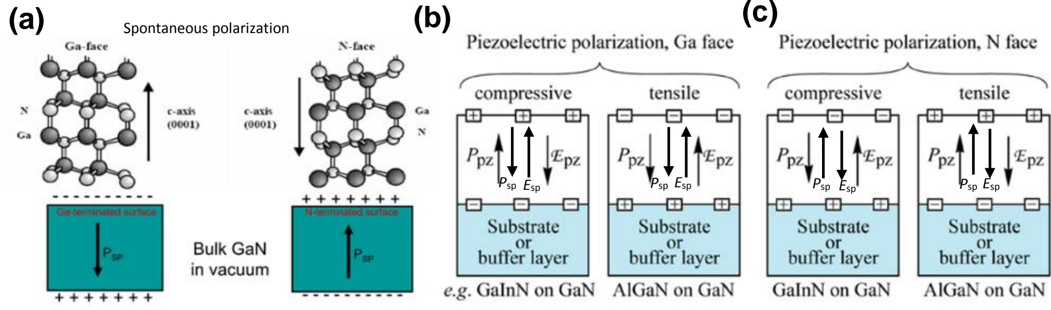

Figure 1-10 (a) Spontaneous polarization of Ga-face and N-face GaN grown on bulk GaN substrate.[29] Piezoelectric polarization of the (b) Ga-face and (c) N-face Al(In)GaN grown on GaN substrate or a buffer layer.[16]

Therefore, the total magnitude of polarization is the sum of spontaneous and piezoelectric polarization for InGaN and AlGaN ternary alloys epilayers:

$$P^{tot}_{In_xGa_{1-x}N} = P^{sp}_{In_xGa_{1-x}N} + P^{pe}_{In_xGa_{1-x}N} \quad (1\text{-}11)$$

$$P^{tot}_{Al_xGa_{1-x}N} = P^{sp}_{Al_xGa_{1-x}N} + P^{pe}_{Al_xGa_{1-x}N} \quad (1\text{-}12)$$

Figure 1-11 shows the calculated results for AlGaN and InGaN ternary alloys grown on relaxed GaN.[30]

This total polarization has a significant effect on the optoelectronic properties of GaN-based blue and UV LEDs through inducing a polarization field in the quantum well active region of the LEDs. This internal electric field tilts the energy band, spatially separates the electrons and holes, and pushes them to the opposite side of the quantum well, as shown in Figure 1-12 (b). By contrast, electron and hole wave functions overlap very well in the space within the quantum well without a polarization field, as shown in Figure 1-12 (a). According to Fermi's golden rule,

$$r_{sp} \propto < \psi_e | H' | \psi_h > \quad (1\text{-}13)$$

where r_{sp} is the spontaneous emission rate, H' is Hamiltonian perturbation, and ψ_e and ψ_h are electron and hole wave functions. Therefore, the reduction of carriers' spatial

overlapping because of the polarization field in the quantum wells suppresses the quantum wells' spontaneous emissions. Furthermore, the polarization field in the quantum well reduces its radiative recombination efficiency. Moreover, polarization field-induced band tilt narrows the effective bandgap energy, yielding a red shift in its emission wavelength, which is known as the quantum-confined Stark effect (QCSE). The QCSE can be alleviated by maintaining the quantum well layer as thin as possible (i.e., 2–3 nm).[16] This polarization field can be screened using a high injection current, resulting in a blue shift in the emission wavelength with increasing injection currents.

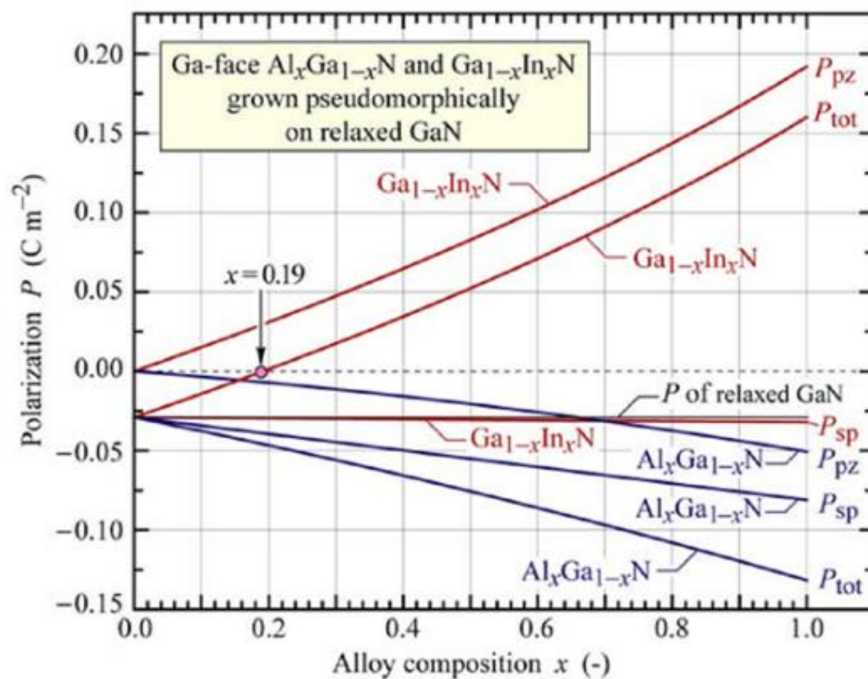

Figure 1-11 Calculated spontaneous, piezoelectric, and total polarization for AlGaN and InGaN ternary alloys grown on relaxed GaN.[30]

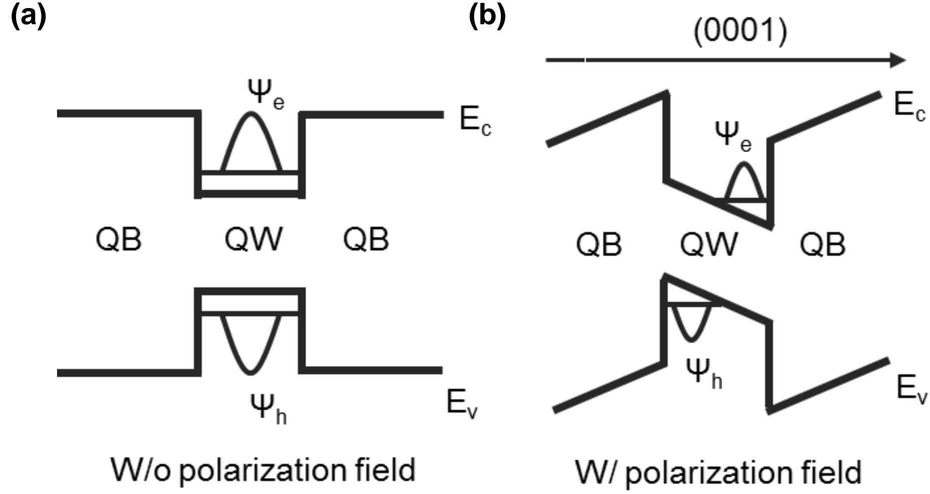

Figure 1-12 Schematic band diagram of active region (a) w/o (b) w/ polarization fields.

1.2.3 Efficiency of GaN-based LEDs

Ideally, GaN-based LEDs emit one photon for every electron injected in the LEDs, thereby yielding a unit external quantum efficiency (EQE); however, in reality, this eficiency is always smaller than 100% and it is defined as follows:[16,31]

$$\eta_{EQE} = \frac{number\ of\ photons\ emitted\ out\ of\ LED\ per\ second}{number\ of\ electrons\ injected\ into\ LED\ per\ second} = \frac{P_{out}/_{h\nu}}{I_{in}/_{e}} \qquad (1\text{-}14)$$

where P_{out} is the light output power from LEDs and I_{in} is the LED injection current. This efficiency measures the quantum efficiency of electron-to-photon conversion by LEDs. During this conversion, the electrons injected are first converted to photons in the MQW active region, and then those photons attempt to escape to free space from the LEDs. The efficiency related to the first process is described as the internal quantum efficiency (IQE), which is defined as follows:[16,31]

$$\eta_{IQE} = \frac{number\ of\ photons\ emitted\ from\ active\ region\ per\ second}{number\ of\ electrons\ injected\ into\ LED\ per\ second} = \frac{P_{active}/_{h\nu}}{I_{in}/_{e}} \qquad (1\text{-}15)$$

where P_{active} is the optical power emitted from the MQW active region. During this process, the electrons injected are first transported to the MQW active region where they

are converted to photons. The efficiency related to the former proces is injection efficiency (IJE), which is defined as follows:[31]

$$\eta_{INJ} = \frac{number\ of\ electrons\ injected\ into\ active\ region\ per\ second}{number\ of\ electrons\ injected\ into\ LED\ per\ second} = \frac{I_{active}/e}{I_{in}/e} \quad (1\text{-}16)$$

where I_{active} is the current injected into the MQW active region. The latter process is radiative efficiency (RDE), which is defined as follows:[31]

$$\eta_{RAD} = \frac{radiative\ total\ recombination\ rate}{total\ recombination\ rate} = \frac{R_{rad}}{R_{rad}+R_{non-rad}} \quad (1\text{-}17)$$

where R_{rad} and $R_{non\text{-}rad}$ are radiative and nonradiative recombination rates, respectively. Therefore, IQE can be aternatively expressed as[31]

$$\eta_{IQE} = \eta_{INJ}\eta_{RAD} \quad (1\text{-}18)$$

After the photons are emitted from the quantum well, they attempt to escape into free space; accordingly, light extraction efficiency (LEE) describes the fraction of photons that manage to escape, which is defined as follows:[16,31]

$$\eta_{LEE} = \frac{number\ of\ photons\ emitted\ out\ of\ LED\ per\ second}{number\ of\ photons\ emitted\ from\ active\ region\ per\ second} = \frac{P_{out}/h\nu}{P_{active}/h\nu} \quad (1\text{-}19)$$

The EQE can also be expessed as

$$\eta_{EQE} = \eta_{IQE}\eta_{LEE} = \eta_{INJ}\eta_{RAD}\eta_{LEE} \quad (1\text{-}20)$$

Moreover, the wall-plug efficiency (WPE) of LEDs measures the LEDs' power efficiency and is defined as follows:[16,31]

$$\eta_{wall-plug} = \frac{light\ power\ output\ from\ LED}{electrical\ power\ fed\ to\ LED} = \frac{P_{out}}{I_{in}V} \quad (1\text{-}21)$$

where V is the forward bias voltage applied across the LEDs. WPE can also be expressed as

$$\eta_{wall-plug} = \eta_{EQE}\frac{h\nu}{eV} = \eta_{IQE}\eta_{LEE}\frac{h\nu}{eV} = \eta_{INJ}\eta_{RAD}\eta_{LEE}\eta_{VTG} \quad (1\text{-}22)$$

where the voltage efficiency (VTE) η_{VTG} measures the electrical potential energy loss before electrons are injected into the MQW active region. The VTE is defined as[31]

$$\eta_{VTG} = \frac{energy\ of\ photons\ emitted\ from\ LED}{energy\ of\ electrons\ fed\ to\ LED} = \frac{h\nu}{eV} \quad (1\text{-}23)$$

1.2.4 Efficiency road map and technical issues of GaN-based UV LEDs

In the past decade, considerable effort has been devoted to improving the performance of the GaN-based UV LEDs.[32-59] Consequently, the EQE of GaN UV LEDs below 360 nm has been boosted from below 0.1% to a few percent depending on the wavelength, as shown in Figure 1-13 (a).[59] Furthermore, it seems that this trend may continue, as implied by the road map projection in Figure 1-13 (b),[60] where the WPE continues to improve until 2025 for 265, 285, and 310 nm LEDs. However, it is challenging for the EQE of UV LEDs below 360 nm to achieve the targets set for practical application in Figure 1-13 (a). This is because of the difficulty of improving the EQE related to the intrinsic material properties of AlGaN in a UV LED structure.[24,61]

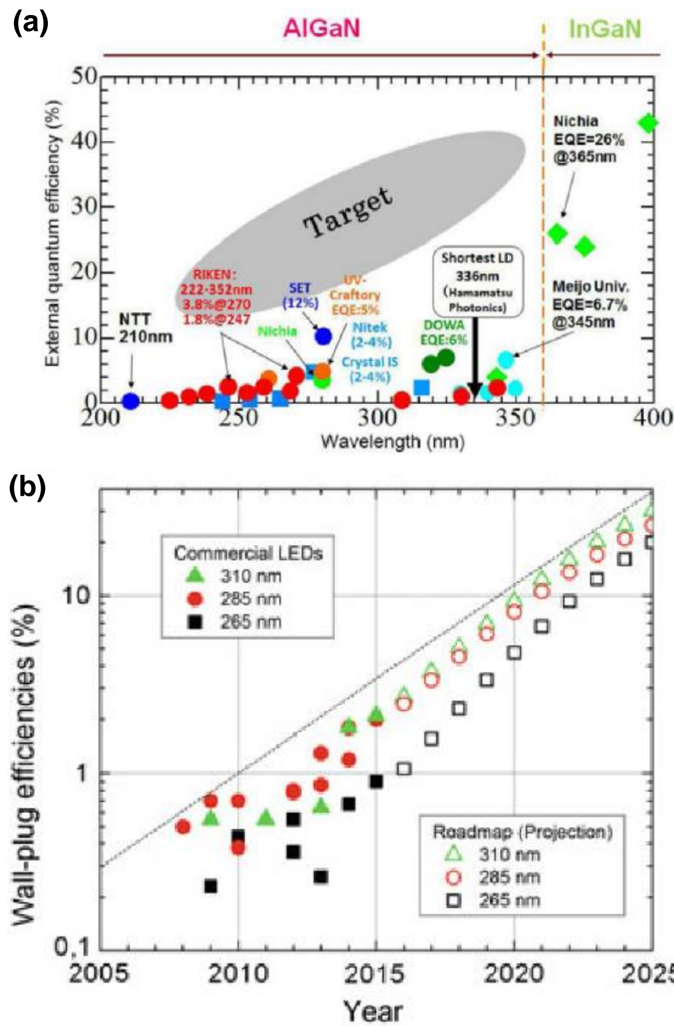

Figure 1-13 (a) Current EQE status of GaN-based UV LEDs,[32] and (b) WPE road map projection for 265, 285, and 310 nm GaN-based UV LEDs.[33]

The crystal quality of AlGaN epilayers is poor, especially with high Al molar fraction incorporation. This is caused by the large lattice and thermal expansion mismatch between the AlGaN epilayers and sapphire substrate, resulting in a low IQE.[16] Moreover, the doping efficiency of $Al_xGa_{1-x}N$ is low because of the high ionization energies of the dopants. In particular, the activation energy of Mg acceptor climbs from 170 meV in GaN to 630 meV in AlN,[62] far beyond the 26 meV thermal energy at an ambient temperature. Hence, realizing practical p-type conductivity in Al-rich AlGaN is rather challenging. As a result, non-Ohmic contact is normally formed between the p-electrode

and highly resistive p-AlGaN, thereby leading to a high operation voltage and thus poor VTE, as shown in Figure 1-14. In addition, the p-type doping efficiency of AlGaN is much lower than its n-type doping efficiency,[62-64] and thus yields a much higher concentration of electrons in n-AlGaN than that of holes in p-AlGaN. In addition to slower mobility of holes than that of electrons, this disparity in carrier concentration leads to electron leakage, and thus to the low IJE.[65] Moreover, the resistive p-AlGaN localizes the current path and induce a current crowding effect, thereby reducing the RDE.[16]

To circumvent the p-type doping of AlGaN, a p-GaN layer is employed on top to facilitate the Ohmic p-contact and enhance the hole injection. However, this p-GaN top layer strongly absorbs the UV emissions from the AlGaN MQWs because the bandgap energy of GaN is lower than the photon energy of the emissions, leading to a poor LEE. This problem can be partially alleviated by adopting a bottom emission flip-chip structure with a reflective mirror on top of the p-GaN layer, which redirects the LED's UV emissions from an upward direction to a downward one.[31] However, this imperfect mirror still engenders optical loss to the LEDs, and thus suppresses the LEE. In addition, because of strong anisotropic emissions from Al-rich AlGaN MQWs,[66] most of the light emitted from them propagates in the emission plane, where it is reabsorbed and converted into heat.[10] Hence, the LEE of UV LEDs drops. All of the aforementioned technical problems limit the efficiency of GaN-based UV LEDs below 360 nm. To solve these problems—and thus improve these LEDs' efficiency—numerous techniques have been proposed.[10,60,67]

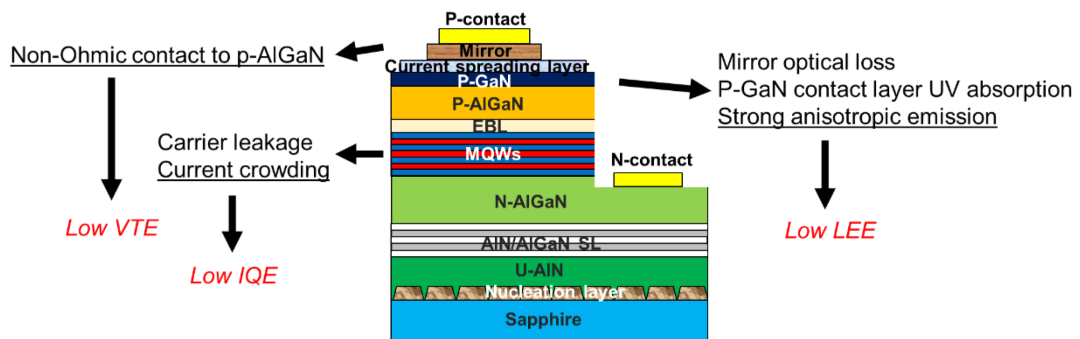

Figure 1-14 Schematic structure of a typical flip-chip GaN-based UV LED below 360 nm with major technical issues that limit its efficiency.

1.3 Challenges, motivation, and objectives

To date, a considerable amount of research has contributed to improving the efficiency of the GaN-based UV LEDs. As a result, the EQE of UV LEDs has been enhanced from below 0.1 % to approximately 1–10% depending on the emission wavelength. However, compared with GaN-based blue LEDs, GaN-based UV LEDs still suffer low efficiency. Therefore, improving the efficiency of GaN-based UV LEDs is necessary before they impact the consumer market and replace traditional UV light sources.

For this thesis, we began the discussion from the design, growth, fabrication, and characterization of the GaN-based blue LEDs. With the GaN-based blue LED platform we developed, we extended our work to the design, growth, fabrication, and characterization of the GaN-based near-UV LEDs and toward UV-C research. We aimed to improve the performance of GaN-based UV LEDs through novel structural and device solutions, including the size effect, Al incorporated quantum barriers (QBs), and electron beam (e-beam) pumping.

The main objectives of this thesis can be summarized as follows:

I. To understand the LED structure and operation of InGaN/GaN and InGaN/AlGaN MQW LEDs.

II. To design, grow, and characterize InGaN/GaN and InGaN/AlGaN MQW epitaxial LED wafers.
III. To achieve high-quality and uniform emission wavelength across 2-inch epitaxial LED wafers.
IV. To fabricate and characterize high-performance InGaN/GaN and InGaN/AlGaN MQW lateral, flip-chip, and vertical LED devices.
V. To study LED theoretical physical models, involving the band structure, carrier transportation and injection, carrier concentration distribution, and carrier recombination and photon generation processes.
VI. To investigate the efficiency droop and electrical characteristic dependence of GaN-based blue LEDs on chip mesa.
VII. To enhance the efficiency and reduce the droop of near-UV micro-LEDs through size shrinking.
VIII. To investigate the influence of AlN composition in QBs on the performance of near-UV LEDs.
IX. To probe the correlation between carrier diffusion and the efficiency of light sources based on e-beam pumped MQWs.

1.4 Major contributions of the thesis

In the study conducted for this thesis, various GaN-based LED structures were designed, grown, and fabricated to enhance the performance of InGaN/(Al)GaN blue and near-UV LEDs. High crystal quality and uniform emission wavelengths were achieved and demonstrated successfully on 2-inch epitaxial LED wafers in the near-UV range. Thereafter, the LED device fabrication was designed, optimized, and tested for the grown epitaxial LED wafers. Based on this platform, novel structures were designed for

the performance enhancement of InGaN/(Al)GaN blue and near-UV LEDs.

Furthermore, the size effect on the efficiency droop of InGaN/GaN blue LEDs was investigated. The EQE and WPE droop started at a higher current injection for an LED device with a larger mesa dimension, which was because of the reduced injection current density. However, the EQE droop began at a lower injection current density for an LED device with a larger mesa dimension because of increased current crowding. Moreover, the WPE droop began at a slightly higher injection current density when the mesa dimension of the LEDs was further enlarged. This was ascribed to the shallow slope of the I-V characteristics around the position of the EQE peak. Moreover, both the series resistance (SRRS) and ideality factor decreased as the mesa dimension of the LEDs increased. This suggested that the I-V characteristics of a real LED approach those of an ideal LED as the mesa dimension of LEDs increases.

In addition, the size effect was studied on the electrical and optical characteristics of near-UV micro-LEDs. The EQE enhanced as their size decreased, but the enhancement became marginal as the size reduced from 50×50 μm^2 to 25×25 μm^2. Moreover, the efficiency droop reduction reversed as the size decreased from 50×50 μm^2 to 25×25 μm^2. In addition to the current spreading effect, strain relaxation, sidewall defects, and p-contact resistance were found to be the root causes of the size effect. The 50×50 μm^2 micro-LED produced the highest performance in terms of efficiency and droop, which provided design rules of thumb for UV LEDs.

The low confinement capability of near-UV MQWs, and thus low carrier injection, were alleviated by incorporating Al into the QBs and increasing the composition of AlN. The

influence of AlN composition in QBs on the performance of near-UV LEDs was systematically studied by adopting multilayer QB structures. Based on our study, we designed, grew, and fabricated an optimized near-UV LED device with a QB structure of AlGaN QBs in QB1 to the last QB and incorporating AlN composition graded AlGaN ILs with graded AlGaN ILs grown with a temperature ramp up from QWs to QBs for QB2 to the last QB.

Furthermore, e-beam pumped UV structures were successfully demonstrated. The cathodoluminescence (CL) characteristics of near-UV InGaN/AlGaN MQW structures with 8, 10, 15, and 20 QWs were systematically studied. The relationship between the acceleration voltage and QW number was established by introducing the contribution to MQW absorption from carriers generated within the diffusion length below the MQWs. This new understanding will assist researchers in designing efficient e-beam pumped UV structures. Moreover, e-beam pumped deep-UV structures were tested and demonstrated, which will be critical for the development of efficient deep-UV emitters.

1.5 Organization of the thesis

This thesis begins with the introduction in Chapter 1, including an overview of GaN-based LEDs, challenges, motivation and objectives as well as the major contributions and organization of the thesis. Throughout this thesis, all the epitaxial wafers of the GaN-based epitaxial structures were prepared using our MOCVD system and Chapter 2 covers epitaxial growth and subsequent wafer level characterization of these GaN-based epi-structures.

In chapter 3, LED device fabrication is described. Based on this epitaxial growth, using

the same device fabrication process flow and characterization approaches, novel structures have been studied for the GaN-based blue and near-UV LED in Chapters 4-6. In our blue LED work (Chapter 4), we investigated the WPE efficiency droop behavior, differential resistance, parasitic series resistance, ideality factor of the InGaN/GaN blue LEDs with varying chip mesa dimension. In our near-UV micro-LED work (Chapter 5), we investigated and designed the near-UV micro-LEDs to enhance the efficiency and reduce the efficiency droop, when we reduced the chip mesa dimensions. Next, again using the same near-UV structures, in our study on the near-UV LEDs (Chapter 6) this time, we systematically studied the influence of AlN composition in the QBs on the performance of the near-UV LEDs, which was an unclear critical parameter for our near-UV epi-structures all along.

Finally, as the emission wavelength is shifted further from near-UV to deep-UV, the performance of GaN-based UV LEDs has been held back by low doping efficiency of p-AlGaN (p-type doped AlGaN) and thus non-Ohmic p-contact and electron leakage. Therefore, as an extension of our work on III-N, we investigated e-beam pumping as a potential technique for the next-generation UV light source with great environmental and economic benefits. In Chapter 7, we therefore started developing e-beam pumped III-N epi-structures in the near-UV range and applied our findings to deep-UV structures based on e-beam pumping. As a result, we successfully enhanced the light output power substantially.

Following then Chapter 8 recaps all of the research work completed in this thesis and put in a perspective and concludes the thesis with recommendations for further research.

Chapter 2 Epitaxial Growth and Wafer-Level Characterization of GaN-Based Blue and Near-UV LEDs

2.1 Metal-organic chemical vapor deposition system

Today, most GaN-based LEDs are grown on sapphire substrate using the popular metal-organic chemical vapor deposition (MOCVD) method. MOCVD, also known as metalorganic vapour phase epitaxy (MOVPE) or organometallic vapour phase epitaxy (OMVPE), is a common chemical vapor deposition (CVD) method for growing single crystal thin films on crystal substrate with atomic layer precision. Compared to molecular beam epitaxy (MBE) and atom layer deposition (ALD), MOCVD growth is much faster (up to a few microns per hour) and capable of upscaling, which are favored for industrial mass production. Moreover, the MOCVD growth process allows wide-range temperature control (up to 1600°C) and is thermodynamically favorable for high quality AlGaN growth. Figure 2-1 illustrates the MOCVD epitaxial growth process for III-nitrides, which follows several reaction steps: (a) the transport of precursors of metalorganics (MO) trimethylgallium (TMGa) (trimethylaluminium [TMAl], trimethylindium [TMIn], triethylgallium [(TEGa]) and hydride (ammonia [NH_3]) sources in the gas phase to the substrate via hydrogen/nitrogen (H_2/N_2) carrier gas; (b) the diffusion of precursor molecules into the boundary layer; (c) the absorption of precursor molecules onto the heated substrate's surface; (d) the surface diffusion of precursor molecules into the reaction sites as well as the pyrolysis of molecules into Ga (Al, In) adatoms under high temperature heating; (e) the surface reaction of Ga (Al, In) and N adatoms, producing GaN (InGaN, AlGaN), and then crystalization of products at the reaction sites; and (f) the desorption and diffusion of by-products past the boundary layer before they are carried out with the gas flow. Moreover, dopant precursors such as silane (SiH_4) and bis(cyclopentadienyl)magnesium (Cp_2Mg) follow the same reaction

steps and provide n- and p-type dopants.

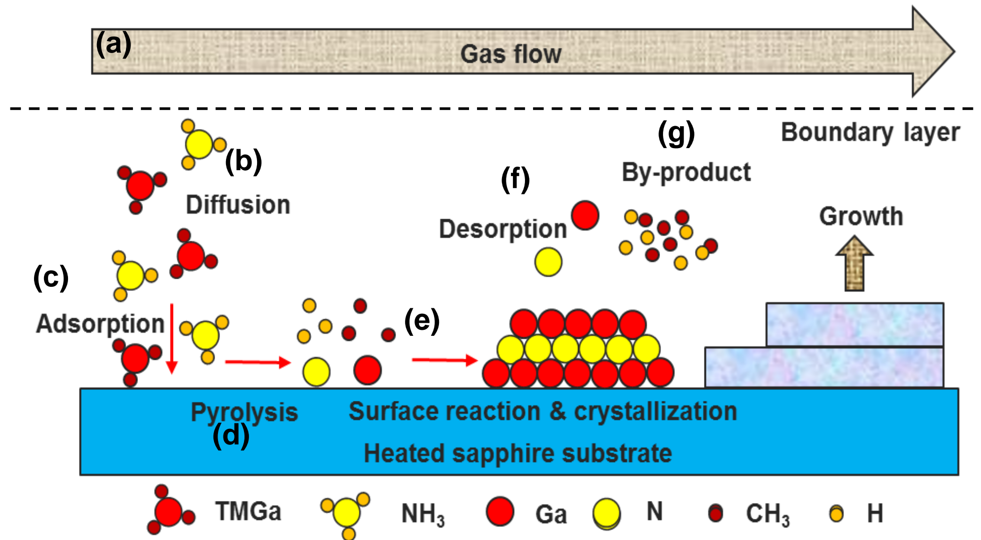

Figure 2-1 Schematic sketch of the MOCVD growth process for III-nitrides.

This III-nitride MOCVD growth process can be described using the following chemical reaction:

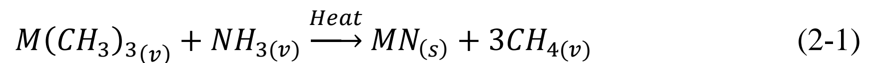

$$M(CH_3)_{3(v)} + NH_{3(v)} \xrightarrow{Heat} MN_{(s)} + 3CH_{4(v)} \tag{2-1}$$

where M denotes Ga, In, and Al elements.

Figure 2-2 presents a schematic sketch of an MOCVD system. During MOCVD epitaxial growth, MO (TMGa, TMAl, TMIn) and hydride (NH_3) sources supplied with H_2/N_2 carrier gas are first mixed in the gas mixing system and then fed into the reactor chamber through the showerhead. Substrate wafers are placed on a graphite susceptor with tungsten heaters below. The chemical reaction (2-1) proceeds until the end of the growth process in the reactor chamber. Furthermore, the susceptor continuously rotates throughout the process to ensure uniform heating across the wafers. The chamber is also connected to a pump system.

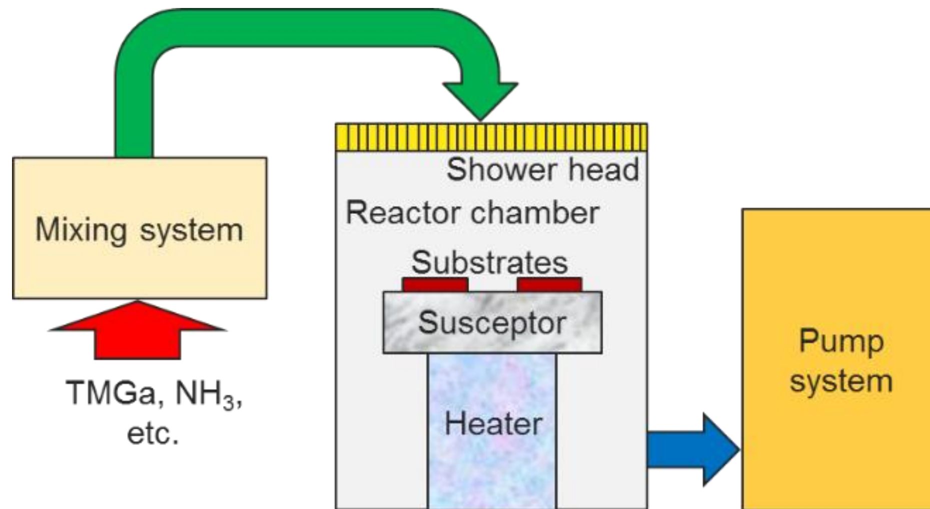

Figure 2-2 Schematic of an MOCVD system.

In the present study, all the epitaxial wafers of GaN-based blue LEDs were prepared using an AIXTRON® close couple showerhead (CCS) MOCVD system. This system can process three 2-inch wafers simultaneously. Figure 2-3 (a) and (b) are photographs of this system and the susceptor holding wafers in the reactor chamber. Blue LED wafers were grown epitaxially along the c-axis on c-plane sapphire substrates with MO (TMIn, TMGa, TMAl) and hydride (NH_3) sources as group III and V precursors, respectively.

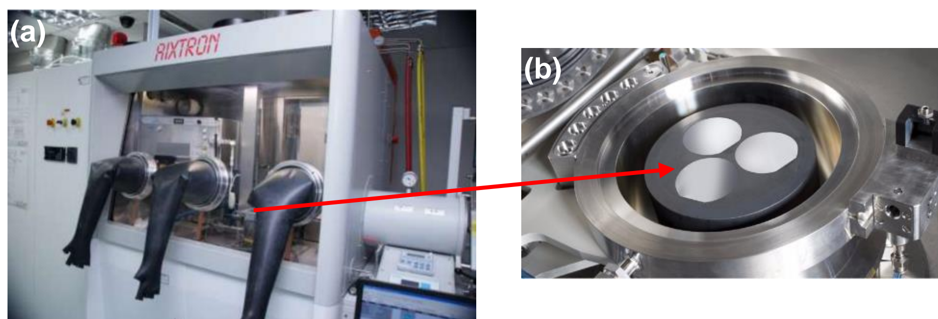

Figure 2-3 Photographs of (a) the AIXTRON® MOCVD system, and (b) the susceptor holding wafers in the reactor chamber.

2.2 Epitaxial growth and layer structure of GaN LED wafers

2.2.1 GaN blue LED Wafer

Figure 2-4 illustrates the epitaxial growth process of GaN-based blue LED wafers, which follows several steps: (a) First, sapphire substrate is treated with thermal annealing in H_2 under a high temperature followed by nitridation in NH_3, resulting in an AlN or AlO_xN_{1-x} strain relaxation top layer; (b) an amorphous GaN layer with a thickness between 20 and 25 nm is grown at low temperatures (typically 550–600°C) as nucleation layer; (c) recrystallization of the GaN nucleation layer occurs at an elevated temperature of 1050°C, which transforms the amorphous GaN layer into crystal GaN islands with 30° *c*-axis rotation; (d) the GaN islands grow and coalesce into GaN film with TMGa and NH_3 feeding in; (e) the 3D growth mode gives way to a 2D growth mode and an unintentionally doped GaN (u-GaN) layer is formed; (f) Si dopant is introduced to the reactor chamber by diluted SiH_4 gas, forming an Si doped n-type GaN (n-GaN), following which InGaN/GaN MQWs are grown with periodical In incorporation by TMIn; (g) TMAl and Cp2Mg are introduced into the chamber as Al and p dopants, respectively, and then an Mg doped p-type $Al_xGa_{1-x}N$ (p-AlGaN) layer is grown as EBL; and (h) Mg doped p-type GaN (p-GaN) and last p^+-GaN heavily doped layers are formed for hole injection and p-type Ohmic contact.

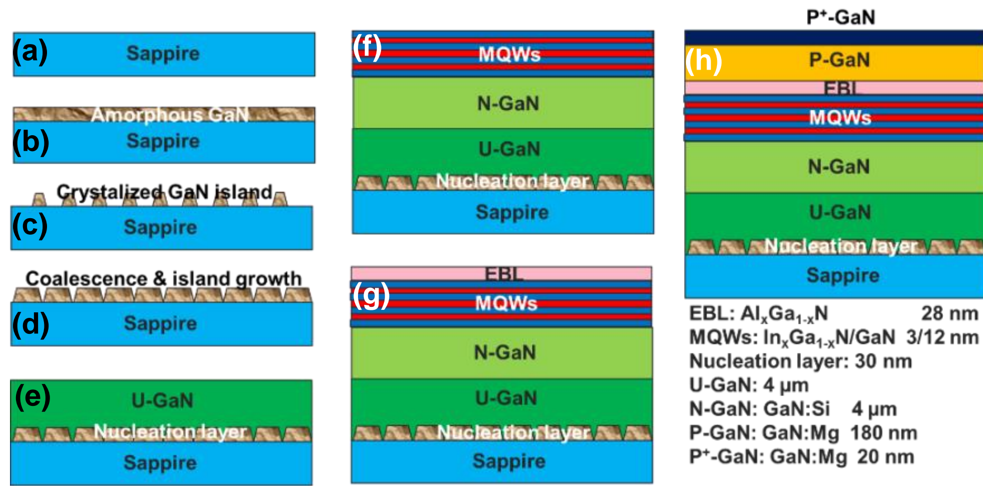

Figure 2-4 Epitaxial growth process flow for GaN-based blue LED wafers: (a) sapphire nitridation, (b) amorphous GaN deposition, (c) crystallization, (d) GaN island growth & coalescence, and growth of (e) u-GaN, (f) n-GaN and InGaN/GaN MQWs, (g) AlGaN EBL and p-GaN and p^+-GaN layers.

Figure 2-4 (h) shows the complete epitaxial structure of a GaN blue LED, which consists of a 30-nm-thick nucleation layer; a 4-µm-thick u-GaN layer; a 4-µm Si-doped n-GaN layer with a doping concentration of 5×10^{18} cm^{-3}; several pairs of InGaN/GaN MQWs with 3-nm-thick InGaN quantum wells and 12-nm-thick GaN quantum barriers, respectively; a 28-nm-thick p-AlGaN EBL with a doping concentration of 1×10^{17} cm^{-3}; a 180-nm-thick Mg-doped p-GaN with a doping concentration of 3×10^{17} cm^{-3} and 20-nm-thick heavily doped p^+-GaN with a doping concentration of 1×10^{18} cm^{-3}.

2.2.2 GaN near-UV LED wafers

Based on the epitaxial growth process of blue LED wafers, the emission wavelength is shifted from blue to near-UV through increasing the QW growth temperature. As the QW growth temperature increases, *In* incorporation is suppressed in the QWs, and thus the *In* content is reduced.[68-69] Therefore, the QW bandgap increases and the emission wavelength shifts from a long wavelength to a shorter one. The relationship between the

bandgap of unstrained InGaN and the alloy composition can be seen in Equation 1-3, Table 1-3, and Figure 1-9. Moreover, as the *In* incorporation in the QWs decreases, the QWs become shallower. This weakens the confinement of the MQWs and increases the carrier overflow. For these reasons, it is necessary to incorporate Al into the QBs to increase the confinement of the MQWs. The effect of Al incorporation on the performance of near-UV LEDs was systematically investigated, and this investigation is presented in Chapter 6.

2.3 Wafer-level characterization

2.3.1 GaN blue LED Wafer

After the epitaxial growth, a blue LED wafer was applied with DC bias through indium balls at nine locations across the whole wafer surface and emitted blue light, as shown in Figure 2-5 (a). This emission was also observed in the electroluminescence (EL) spectrum (Figure 2-5 (b)); it peaked at a wavelength of 449.07 nm with a full width at half maximum (FWHM) of 23.67 nm at a 20-mA current injection. Moreover, the emission peak shifted to a shorter wavelength at higher current injections, as expected. Furthermore, the emission peak moved to 447.5 nm at a 100-mA current injection, and this 1.57-nm blue shift in the emission peak was attributted to screening of the polarization field by a high carrier concentration at a high current injection.[70] However, at even higher current injections, the emission peak shifted back instead. At a 350-mA current injection, the emission peak returned to 449.07 nm, which was ascribed to bandgap-narrowing caused by self-heating during the LED operation under continuous current injection.[71] The emission FWHM increased with elevated current injections as follows: 23.67 nm at 20 mA, 25.958 nm at 100 mA, and 29.358 nm at 350 mA. This spectrum broadening was also attributed to self-heating during LED operation.

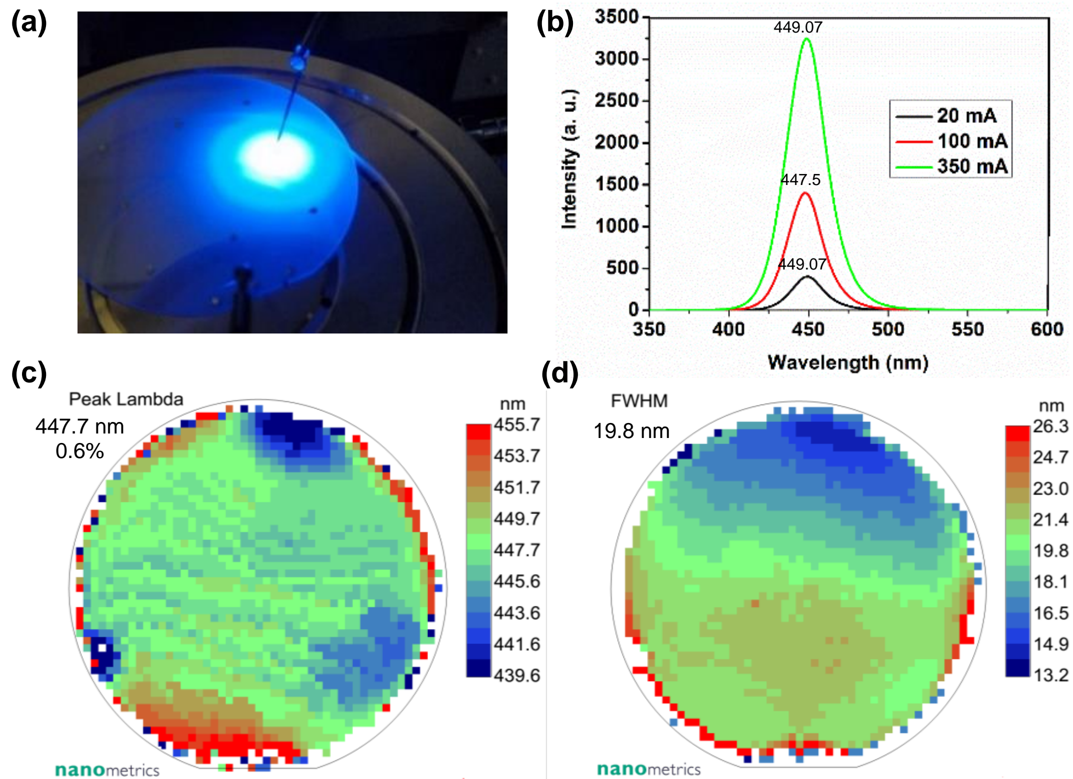

Figure 2-5 (a) Photograph of our GaN blue LED epi-wafer under direct current injection; (b) EL spectrum of the blue LED under different current injections; (c) peak emission wavelength mapping; and (d) FWHM mapping of the LED wafer.

This epitaxial wafer was subjected to a uniformity test, in which both the peak emission wavelength and FWHM at any location on the epi-wafer were recorded with a photoluminescence (PL) mapping system (Nanometrics® RPM-2000). As shown in Figure 2-5 (c) and (d), the wafer exhibited an average peak wavelength of 447.7 nm with a standard deviation of 0.6%, as well as an FWHM of 19.8 nm with a standard deviation of 11%. This much larger standard deviation with FWHM could be ascribed to non-uniform alloy broadening across the wafer, which is caused by non-uniform QWs growth temperature across the wafer.

2.3.2 GaN near-UV LED wafers

In addition, the EL and PL spectra were collected using the same characterization

systems for the near-UV LED wafers. Figure 2-6 (a) shows the peak emission wavelength obtained from EL and PL spectra as a function of the QW growth temperature. Both the EL and PL measurements indicated the same trend: higher QW growth temperatures reduced the peak emission wavelength. Explicitly, the PL measurement showed that as the QW growth temperature increased from 890°C to 940°C, the peak wavelength blue shifted from 450.6 nm to 393.6 nm, and further raising the QW growth temperature to 955°C shifted the peak wavelength to 378 nm. Compared with PL, the EL measurement exhibited similar but longer peak wavelengths, probably because of bandgap narrowing caused by self-heating.[71] The peak emission wavelength of an LED can be expressed as[72]

$$\lambda_{peak}(T) = \frac{hc}{E_{bandgap}(0) - \frac{\gamma T^2}{T+\theta} - \frac{\sigma^2}{kT}} \qquad (2\text{-}2)$$

where h is the Planck's constant; c is the speed of light in a vacuum; $E_{bandgap}$ (0) is the bandgap of the LED at 0 K; k is the Boltzmann constant; T is the environment temperature; γ and θ are the Varshni's coefficients and positive for InGaN alloy; and σ accounts for the degree of the localization effect. As this equation indicates, the peak emission wavelength red shifts to longer wavelengths when self-heating increases the temperature of the LED. Self-heating also broadens the EL spectra, as shown in Figure 2-6 (b). The FWHM is obtained from EL and PL spectra as a function of the QW growth temperature. Additionally, compared with PL, the EL measurement exhibited similar but broader spectrum linewidths. Notably, the EL and PL measurements indicated the same trend: higher QW growth temperatures decreased the emission linewidth. Explicitly, the PL measurement revealed that as the QW growth temperature increased from 890°C to 940°C, the FWHM decreased from 18.5 nm to 11.0 nm, and further raising the QW growth temperature to 955°C reduced the FWHM to 5.2 nm. This observation could be explained by plotting the FWHM against the peak emission

wavelength, as shown in Figure 2-6 (c); the same samples are indicated with the same color. Similar to Figure 2-6 (a) and (b), the self-heating blue-shifted the peak wavelength and broadened the linewidth.

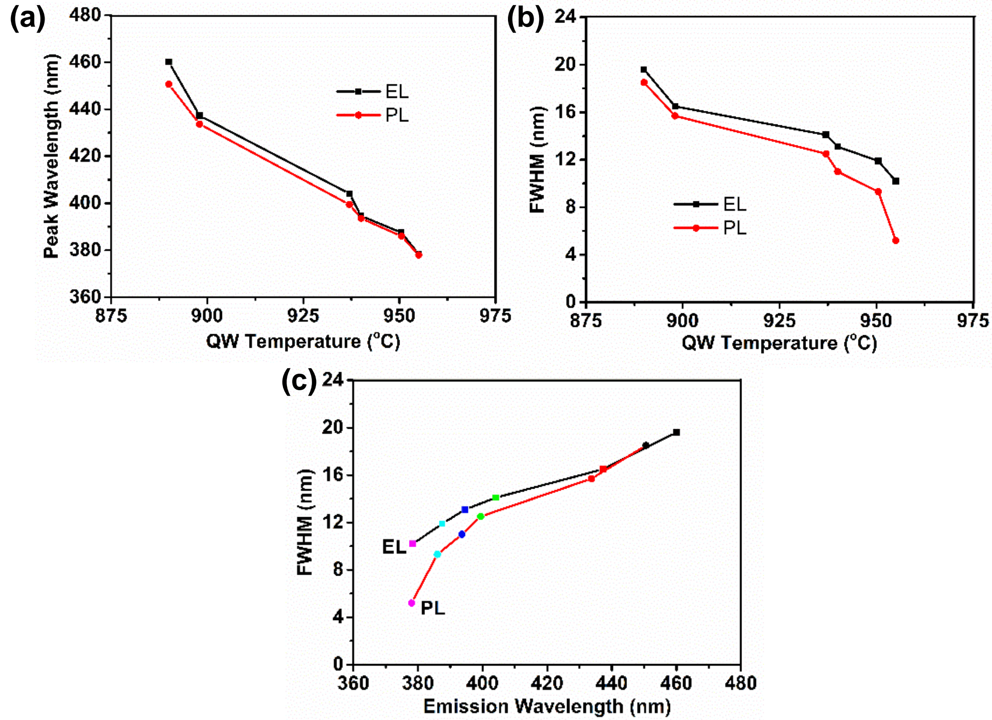

Figure 2-6 (a) QW peak emission wavelength and (b) FWHM obtained from EL and PL spectra as a function of the QW growth temperature; (c) FWHM extracted from (a) and (b) as a function of the peak wavelength.

The FWHM emission of an LED can be expressed as[16]

$$FWHM = \frac{1.8kT\lambda_{peak}^2}{hc} \tag{2-3}$$

where h is the Planck's constant; c is the speed of light in a vacuum; λ_{peak} is the peak emission wavelength; k is the Boltzmann constant; and T is environment temperature. As this equation indicates, the FWHM is proportional to the environment temperature and the square of the peak emission wavelength of the LED. Therefore, raising the QW growth temperature decreases the peak emission wavelength, thereby reducing the emission linewidth. In addition to Equation (2-3) which describes thermal broadening,

alloy broadening should also be taken into consideration. Raising the QWs growth temperature suppresses the In incorporation in the QWs and thus the In content is reduced. As a result, the peak emission wavelength decreases with the decreasing In composition. Besides, alloy broadening is also mitigated, which reduces the emission linewidth. Therefore, raising the QWs growth temperature could reduce the emission linewidth by a combination of these two mechanisms.

Similar to the characterization of the blue LED wafers, the near-UV LED wafers also underwent an EL test; DC bias was applied through indium balls and the emission was observed in the EL spectra, as shown in in Figures 2-7 (a), 2-8 (a), and 2-9 (a). At a 20-mA current injection, the EL spectra peaked at a wavelength of 394.6 nm with an FWHM of 13.1 nm; a wavelength of 387.5 nm with an FWHM of 11.9 nm; and a wavelength of 378.4 nm with an FWHM of 10.2 nm, respectively. Furthermore, these epitaxial wafers were subjected to a uniformity test using a PL mapping system. Both the peak emission wavelength and FWHM at any location on the epi-wafer were recorded. As shown in Figures 2-7 (b) and (c), 2-8 (b) and (c), and 2-9 (b) and (c), the wafers exhibited an average peak wavelength of 393.6 nm with a standard deviation of 0.492% and an FWHM of 11.0 nm with a standard deviation of 5.978%; an average peak wavelength of 386 nm with a standard deviation of 0.582% and FWHM of 9.3 nm with a standard deviation of 9.997%; and an average peak wavelength of 378.0 nm with a standard deviation of 1.445% and an FWHM of 5.2 nm with a standard deviation of 86.99%.

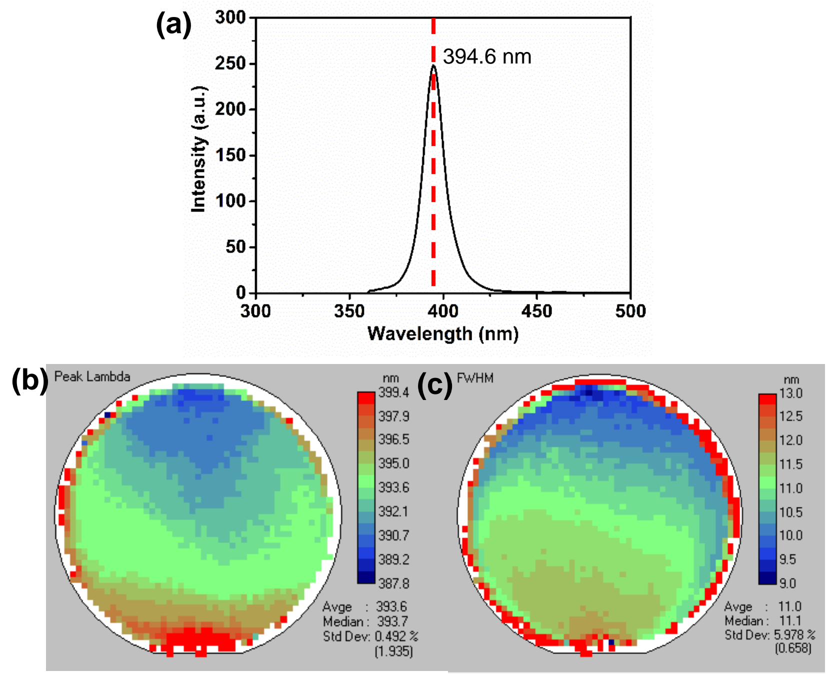

Figure 2-7 (a) EL spectrum of the near-UV LED with a peak emission wavelength of 394.6 nm, (b) peak emission wavelength mapping, and (c) FWHM mapping of the UV LED wafer.

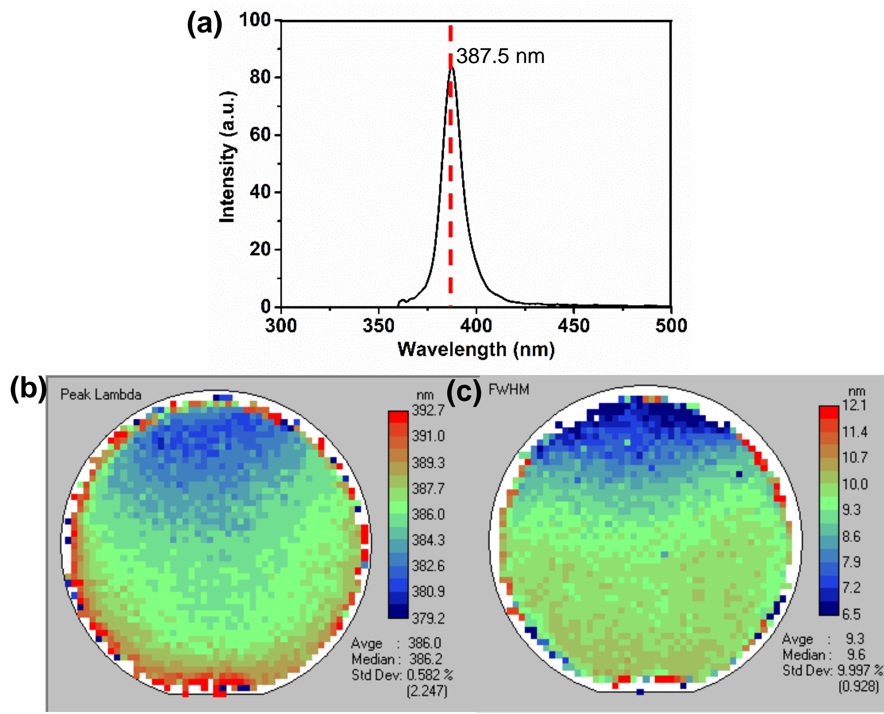

Figure 2-8 EL spectrum of the near-UV LED with a peak emission wavelength of 387.5 nm, (b) peak emission wavelength mapping, and (c) FWHM mapping of the UV LED wafer.

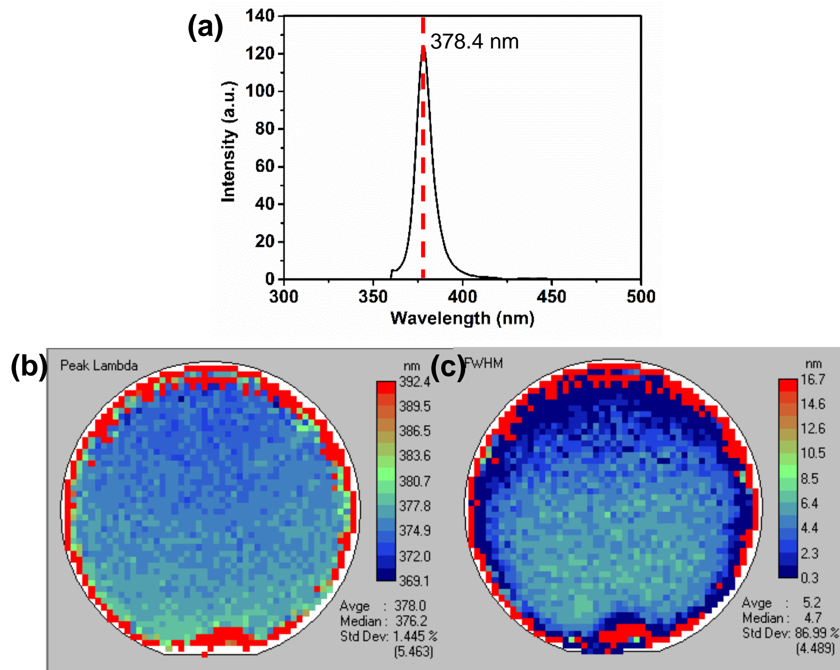

Figure 2-9 EL spectrum of the near-UV LED with a peak emission wavelength of 378.4 nm, (b) peak emission wavelength mapping, and (c) FWHM mapping of the UV LED wafer.

2.4 Summary

In summary, this chapter introduces the MOCVD epitaxial growth process and the MOCVD system, followed by the epitaxial growth process of the GaN-based blue LED wafers and its complete epitaxial structure. Based on the epitaxial growth process of the blue LED wafers, the GaN-based near-UV LED wafers were grown by increasing the QW growth temperature. Electrical and optical characterization were performed at wafer level for the epitaxial GaN-based blue and near-UV LED epitaxial structures. High crystal quality and uniform emission wavelength have been achieved and demonstrated successfully on 2-inch epitaxial LED wafers from blue to the UV, with high uniformity of 0.6% at 447.7 nm, 0.492% at 393.6 nm, 0.582% at 386 nm, and 1.445% at 378 nm. In the next chapter, the LED device fabrication was designed and tested for the grown epitaxial LED wafers.

Chapter 3 Device Fabrication and Chip-Level Characterization of GaN-Based Blue and Near-UV LEDs

3.1 Device fabrication

3.1.1 Device structures for lateral, flip-chip, and vertical GaN-based blue and near-UV LEDs

After epitaxial growth, the GaN-based blue LED wafers proceeded to the device fabrication stage along with the near-UV LED wafers. Three LED device configurations are favored in industrial mass production, namely lateral, flip chip, and vertical structures, as shown in Figure 3-1 (a)–(c). Light is extracted from the top surface of lateral and vertical LED devices but from the bottom of flip-chip LED devices. The n and p contacts are on the same side for lateral and flip-chip LED devices, whereas they are on the opposite side for vertical LED devices.

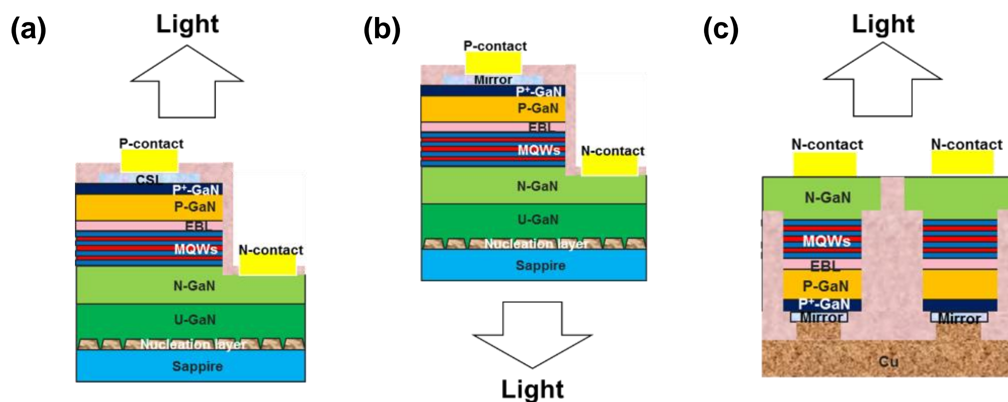

Figure 3-1 Schematic structural sketch of a (a) lateral, (b) flip chip, and (c) vertical LED devices.

3.1.2 Fabrication process for lateral GaN-based blue and near-UV LEDs

Lateral LED devices feature a simple structure and are convenient for low power applcations. Figures 3-2 shows the LED fabrication process flow for lateral GaN-based blue and near-UV LED devices fabrications, which follows:

(a) Bare wafer cleaning: The epitaxial wafers are first immersed in a solution of H_2SO_4 and H_2O_2 at a ratio of 5:1, and then cleaned using IPA acetone in an ultasonic bath; next, the wafers are rinsed with deionized (DI) water and baked in the oven at 110°C.

(b) Current spreading layer (CSL) deposition and patterning: The wafers are spin-coated with AZ5214 photoresist at 2000 rpm for 60 s and then dehydrated on a hot plate at 110°C for 105 s before being exposed to UV light. Subsequently, they are developed in a solution of AZ developer and DI water at a ratio of 1:2. After the photoresist is hard-baked, sputtered indium tin oxide (ITO) or e-beam deposited alloyed Ni/Au layers are used for CSL, followed by the removal of the photoresist and CSL annealing.

(c) Mesa definition: After the photoresist preparation process, which is similar to the spin-coating, baking, UV exposure, and development in CSL patterning, the mesa are defined through the dry etching of inductively coupled plasma (ICP) with Cl_2 gas, followed by ultrasonic cleaning with acetone to remove residues.

(d) Passivation deposition: The samples are coated by SiO_2 using plasma-enhanced chemical vapor deposition (PECVD).

(e) Electrode definition: The n-contact and p-contact patterns are defined on the CSL and n-GaN following a similar sample-cleaning and photoresist-preparation process.

(f) N- and P-contact formation: Following a similar sample-cleaning and photoresist-preparation process, Ti/Au are deposited by e-beams as the N and P contacts.

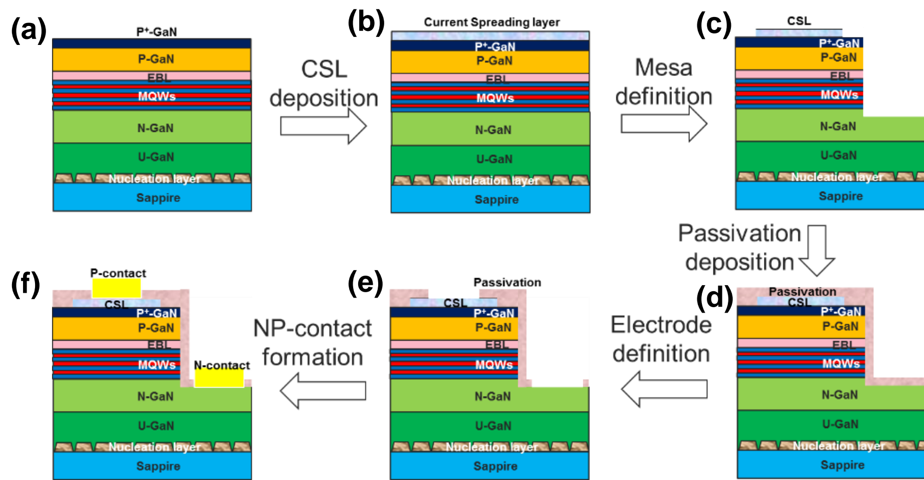

Figure 3-2 Fabrication process flow for lateral structure LED devices: (a) bare wafer cleaning, (b) CSL deposition, (c) mesa definition, (d) passivation deposition, (e) electrode definition, and (f) N and P contact formation.

3.1.3 Fabrication process for flip-chip GaN-based blue and near-UV LEDs

Flip-chip LED devices exhibit high light extraction performance, and thus are desirable for high power applications. Their fabrication process is shown in Figure 3-3, which follows six steps: (a) bare wafer cleaning, (b) mirror deposition, (c) mesa definition, (d) passivation deposition, (e) electrode definition, and (f) N and P contact formation. The photolithography process is similar to that of lateral LED devices, including photoresist spin-coating, baking, UV exposure, and development. The key difference between the fabrication processes is the choice of contact-reflector, which satisfies both high refelectivity and low contact resistance.

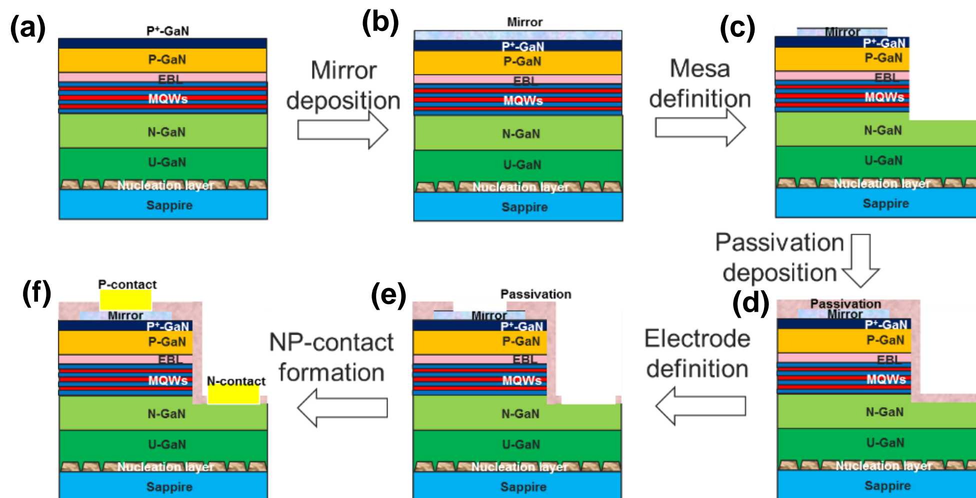

Figure 3-3 Fabrication process flow for flip-chip LED devices: (a) bare wafer cleaning, (b) mirror deposition, (c) mesa definition, (d) passivation deposition, (e) electrode definition, and (f) N and P contact formation.

3.1.4 Fabrication process for vertical GaN-based blue and near-UV LEDs

Vertical LED devices remove the substrate, bypass the substrate effect, and are targeted for high power applications. The fabrication process for vertical LED devices is shown in Figure 3-4, which follows eight steps: (a) bare wafer cleaning, (b) isolation etching, (c) mesa definition, (d) mirror definition, (e) passivation definition, (f) copper plating, (g) sapphire laser lift-off (LLO), and (h) u-GaN etching and N and P contact formation.

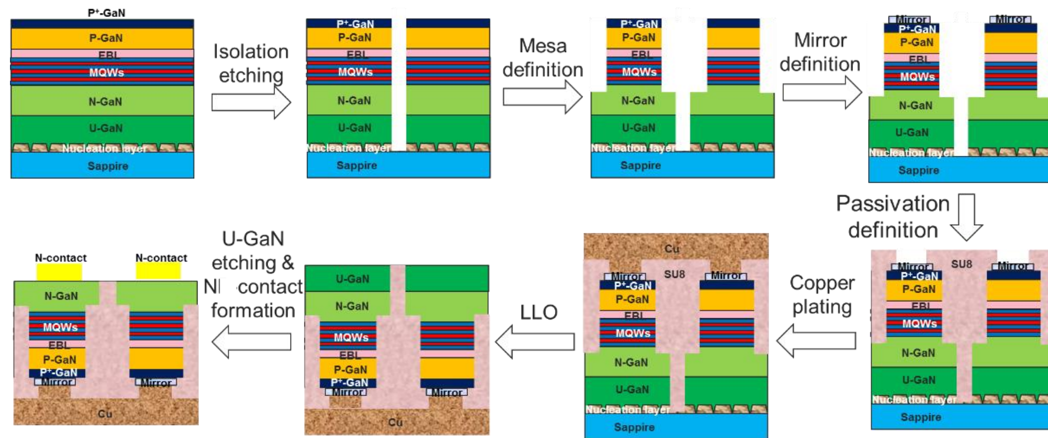

Figure 3-4 Fabrication process flow for vertical LED devices: (a) bare wafer cleaning, (b) isolation etching, (c) mesa definition, (d) mirror definition, (e) passivation definition, (f) copper plating and P contact formation, (g) sapphire laser liftoff (LLO), and (h) u-GaN etching & N contact formation.

The bare wafer cleaning process is similar to that for lateral LED devices fabrication. The isolation etching step involves the dies separation on the cleaned wafers; 2-µm-thick SiO_2 serves as an etching mask after deposition. Isolation pattern transfer using the photolithgraphy process is similar to that of lateral LED devices with reactive ion etching (RIE) dry etching. Subsequently, a 9-µm ICP dry etching process creates isolation trenches before the residues of the oxide are removed by wet etching using buffer oxide etching (BOE). The mesa, mirror, and passivation definition processes are similar to those of flip-chip LED devices, except that the LED devices were passivated with SU8 photoresist. Next, 1-µm-thick Cu is sputtered as the seed layer followed by a 180-µm-thick Cu plating as the P contact. Next, the sapphire substrate is lifted off using an excimer laser followed by HCl cleaning, which removes debris left after the lift-off process. The wafers are then turned and the n-GaN of the LED devices is exposed by ICP dry etching. The exposed surface can be textured to enhance the light extraction. Finally, an N contact is formed following a sample-cleaning and photoresist-preparation process similar to that of lateral LED devices.

In this study, all GaN-based blue and UV LED devices were fabricated in a cleanroom. Pattern definition was assisted by a Karl Suss MJB-4 exposure system. Mesa definition was achieved by etching 1 μm through p^+-GaN, p-GaN, MQWs, and part of n-GaN with ICP-RIE using an Oxford PlasmaPro100 System. The sapphire substrate was lifted off using a 248-nm excimer laser with a Lambda Physik (JPSA)/IX100 system. The metals were deposited using an Edwards_TP E-beam evaporation system.

3.2 Chip-level characterization of lateral, flip-chip, and vertical GaN-based blue and near-UV LEDs

3.2.1 GaN-based blue LEDs

After the device fabrication processes, the lateral, flip chip, and vertical GaN-based blue LED devices on the wafers were observed under an optical microscope, as shown in the insets of Figures 3-5 (c), 3-6 (b) and 3-7 (b), respectively. The chip mesa dimensions of the devices were 06 × 13 mil^2, 20 × 40 mil^2, and 45 × 45 mil^2, respectively. The chip LOPs of the LEDs were measured with an integrating sphere and I-V characteristics with a probe station. The measurement results are shown in Figures 3-5 (b), 3-6 (a) and 3-7 (a), respectively. A typical peak emission wavelength of 455 nm is shown in Figure 3-5 (a) for the lateral 06 × 13 mil^2 blue LED. At a 20-mA current injection, the LOPs were 8.06, 17.21, and 13.79 mW for the lateral, flip-chip, and vertical blue LEDs, respectively. Under the same injection current, their forward voltages were 3.38, 2.58, and 2.75 V, respectively. Furthermore, the EQE was extracted for the lateral, flip chip, and vertical LEDs, as shown in Figures 3-5 (c), 3-6 (b), and 3-7 (b), respectively. Moreover, their efficiency reached a maximum of 21.08% at 0.4 mA, 31.82% at 25 mA, and 25.17% at 40 mA, respectively. Their efficiency started to droop after reaching the

peak value, dropping to 7.60% at 150 mA for the lateral LEDs and to 27.13% and 21.78% at 350 mA for the flip-chip and vertical LEDs. The efficiency droop of LEDs can be expressed as follows:

$$Droop = \frac{\eta_{peak} - \eta_{injection}}{\eta_{peak}} \tag{3-1}$$

where η_{peak} and $\eta_{injection}$ are the peak efficiency and efficiency at the injection current, respectively. Calculated using this equation, the efficiency droop reached 63.95% at 150 mA for the lateral LEDs and 14.77% and 13.44% at 350 mA for the flip-chip and vertical LEDs.

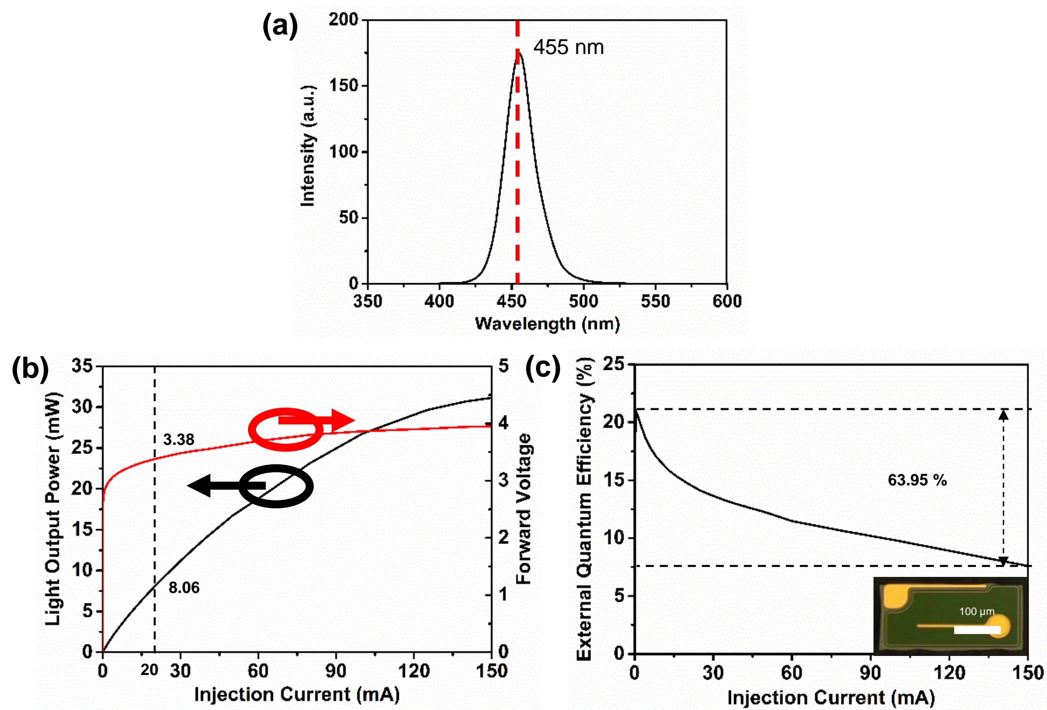

Figure 3-5 (a) Spectrum of a lateral 06 × 13 mil^2 GaN-based blue LED with a peak emission wavelength of 455 nm; (b) current dependent LOP and I-V characteristics for a lateral blue LED device on wafer after fabrication; and (c) EQE of the lateral device (inset: the fabricated 06 × 13 mil^2 lateral blue LED device on wafer).

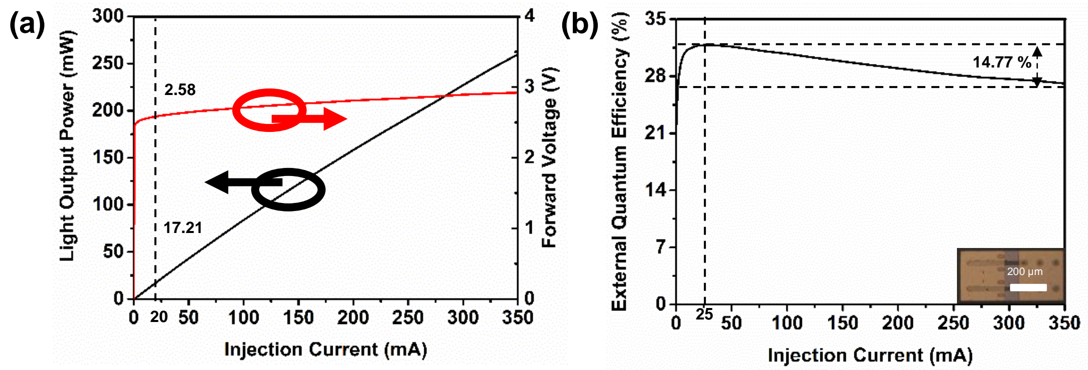

Figure 3-6 (a) Current dependent LOP and I-V characteristics for a flip-chip GaN-based blue LED device on wafer after fabrication; (b) EQE of the flip-chip device (inset: the fabricated 20 × 40 mil^2 flip chip LED device on wafer).

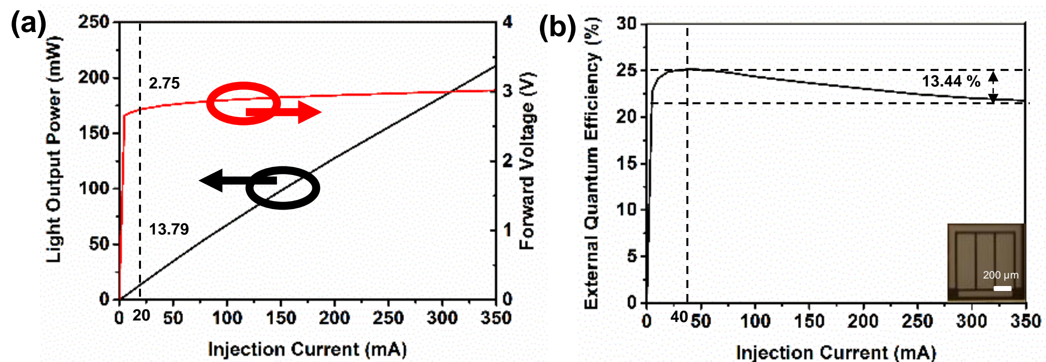

Figure 3-7 (a) Current dependent LOP and I-V characteristics for a vertical GaN-based blue LED device on wafer after fabrication; (b) EQE of the vertical LED device (inset: the fabricated 45 × 45 mil^2 vertical LED device on wafer).

3.2.2 GaN-based UV LEDs

After similar device fabrication processes, the lateral, flip chip, and vertical GaN-based near-UV LED devices were also obtained and ready for further characterization. Their chip mesa dimensions were 07 × 09 mil^2, 15 × 30 mil^2, and 43 × 43 mil^2, respectively. Their chip LOPs were measured with an integrating sphere and I-V characteristics with a probe station as well, as shown in Figures 3-8 (b), 3-9 (a) and 3-10 (a), respectively. A typical peak emission wavelength of 393 nm is shown in Figure 3-8 (a) for the lateral 07 × 09 mil^2 near-UV LEDs. At a 20-mA current injection, the LOPs were 4.61, 11.72,

and 16.53 mW for the lateral, flip chip, and vertical near-UV LEDs, respectively. Under the same injection current, their forward voltages were found to be 3.32, 2.98, and 3.09 V, respectively. The EQE was also extracted for the lateral, flip chip, and vertical LEDs, as shown in Figures 3-8 (c), 3-9 (b), and 3-10 (b), respectively. Their efficiency reached maximums of 7.40% at 13 mA, 21.71% at 80 mA, and 28.35% at 60 mA for the lateral, flip chip, and the vertical LEDs, respectively. Their efficiency started to droop after reaching the peak values, to 2.78% at 150 mA for the lateral LEDs and to 16.64% and 22.01% at 350 mA for the flip-chip and vertical LEDs, respectively. Calculated using Equation 3-1, the efficiency droop reached 62.48% at 150 mA for the lateral LEDs and 23.37% and 22.36% at 350 mA for the flip-chip and vertical LEDs, respectively. Notably, the LOP of the lateral 07 × 09 mil^2 LED rolled off at a 125-mA injection current because of thermal effects.[71]

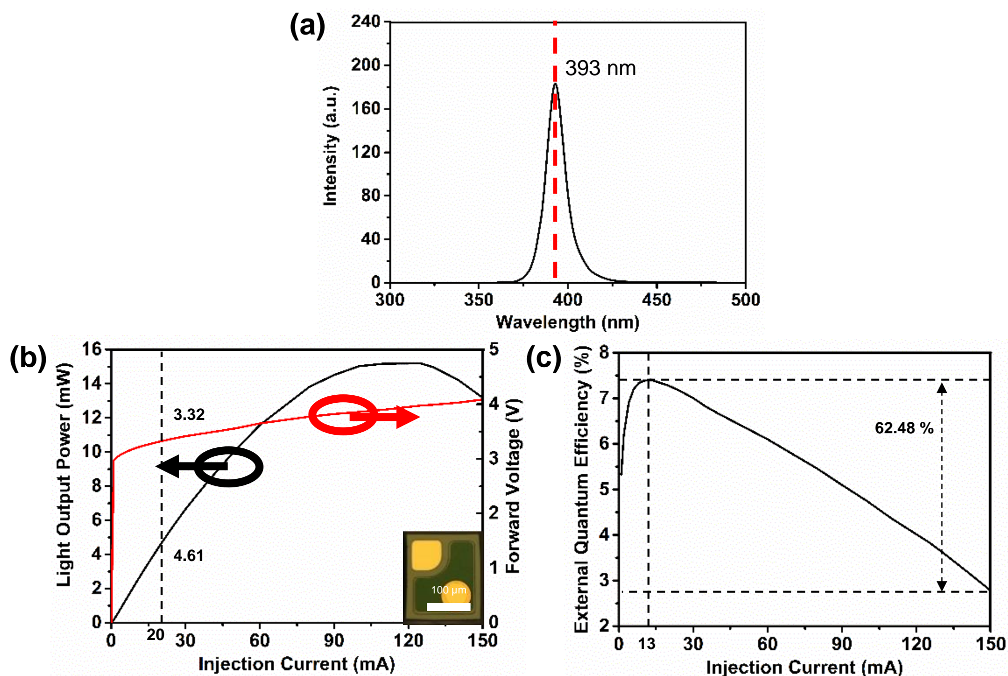

Figure 3-8 (a) Spectrum of a lateral 07 × 09 mil^2 GaN-based near-UV LED with a peak emission wavelength of 393 nm; (b) L-I-V characteristics for a lateral near-UV LED device after fabrication; and (c) EQE of the LED device (inset: the fabricated 07 × 09 mil^2 LED device).

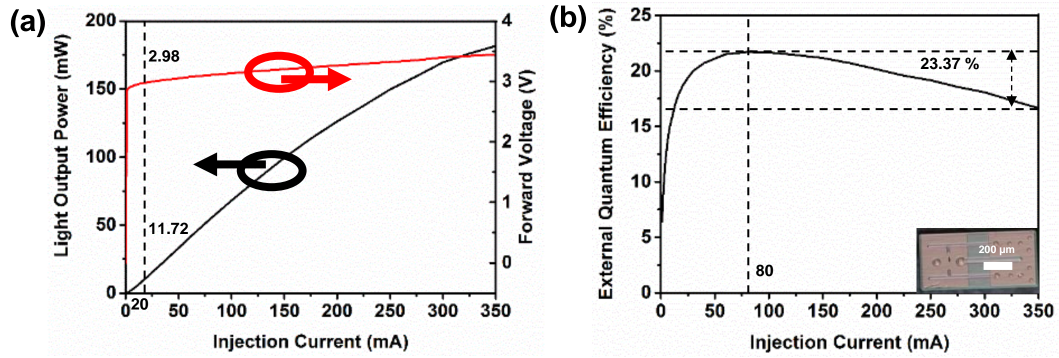

Figure 3-9 (a) L-I-V characteristics for a flip-chip 15 × 30 mil^2 GaN-based 395 nm LED device after fabrication; (b) EQE of the LED device (inset: the fabricated 15 × 30 mil^2 LED device).

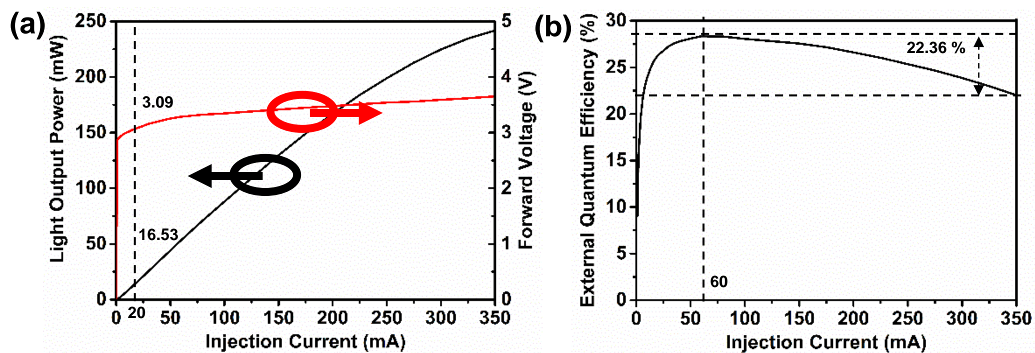

Figure 3-10 (a) L-I-V characteristics for a vertical 43 × 43 mil^2 GaN-based 395 nm LED device after fabrication; (b) EQE of the LED device.

After a similar device fabrication process, the lateral GaN-based 384 nm LED device with a chip mesa dimension of 07 × 09 mil^2 also underwent characterization. The LOP and I-V characteristics are shown in Figure 3-11 (a). At a 20-mA current injection, the LOP was 3.69 mW and the forward voltage was 3.42 V. The EQE was also extracted and is shown in Figure 3-11 (b). The efficiency reached a maximum of 6.28% at a 6-mA injection current, and thereafter the efficiency started to droop. The efficiency drooped to 0.91% at 150 mA and then reached 85.51% at 150 mA. Notably, the LOP rolled off at a 90-mA injection current because of thermal effects.[71]

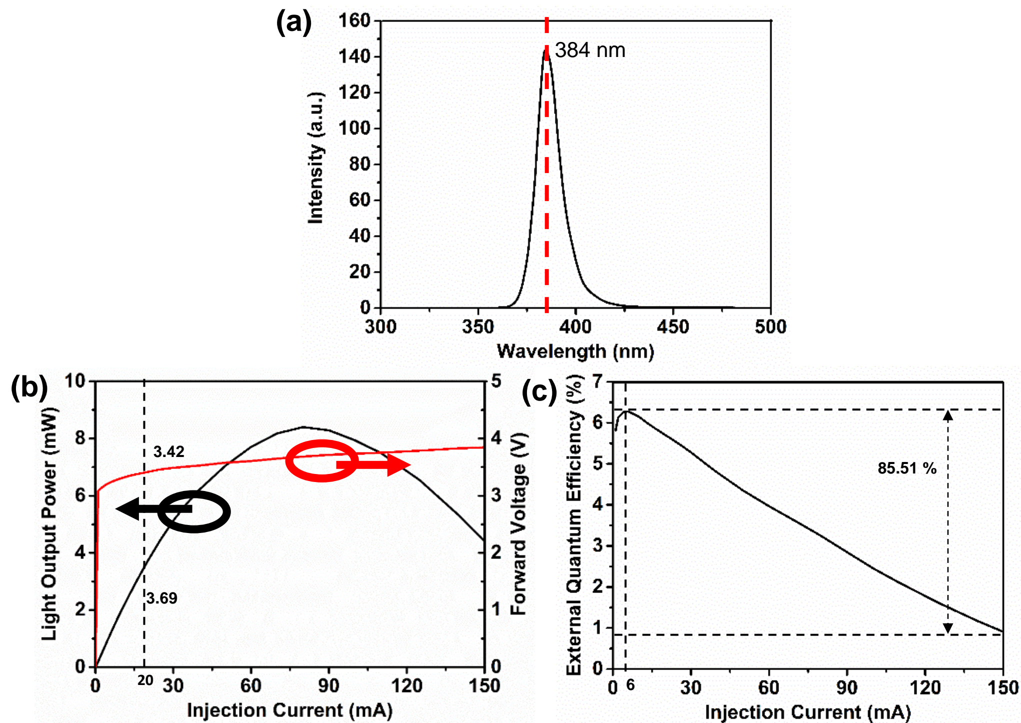

Figure 3-11 (a) Spectrum of a lateral 07 × 09 mil^2 GaN-based near-UV LED with a peak emission wavelength of 384 nm; (b) L-I-V characteristics for the lateral near-UV LED device after fabrication; and (c) EQE of the LED device.

3.3 Discussion

The device fabrication process has been introduced for the lateral, flip chip and vertical GaN-based blue and near-UV LEDs and then the electrical and optical characterization were performed at chip level for the fabricated GaN-based blue and near-UV LEDs. Our GaN-based blue and near-UV LEDs have demonstrated respectable performance compared to the industry. As shown in Figure 3-5 (c), Figure 3-6 (c) and Figure 3-7 (c), our 455 nm lateral 06 ×13 mil^2, flip chip 20 × 40 mil^2 and vertical 45 × 45 mil^2 LED devices demonstrate peak efficiency levels of 21.08%, 31.82% and 25.17%, respectively. Likewise, in Figure 3-8 (c), Figure 3-9 (c) and Figure 3-10 (c), our 393 nm lateral 07 × 09 mil^2, flip chip 15 × 30 mil^2 and vertical 43 × 43 mil^2 LED devices demonstrate peak efficiency levels of 7.40%, 21.71% and 28.35%, respectively.

Although our lateral, flip-chip and vertical structure LEDs all show performance comparable to the industry, we must take into consideration the advantages and disadvantages for each of the three LED configurations before we design novel structures for the performance enhancement of these InGaN/(Al)GaN blue and near-UV LED. Lateral structure LEDs feature a simpler structure and faster device characterization than its flip-chip and vertical counterparts but are only convenient for low-power applications. In contrast, flip-chip structure LEDs exhibit higher performance in light extraction and thus are desirable for high-power applications but are more difficult to characterize due to its bottom emission; vertical structure LEDs remove the substrate and bypass the substrate effect and thus are targeted for high-power applications but are much more difficult to fabricate due to the process controllability of laser lift-off. Therefore, we use flip-chip structure LEDs in Chapters 4-5 and lateral structure LEDs in Chapter 6.

Chapter 4 Efficiency Droop and Electrical Characteristic Dependence of GaN-Based Blue LEDs on Chip Mesa

4.1 Introduction

Compared with conventional LEDs, LED devices with shrunken sizes exhibit improved radiative recombination rates,[73] enhanced LEE,[74] increased current spreading,[75] and reduced thermal effects.[71] Therefore, the effect of chip size is a critical consideration in the design of highly efficient LEDs, and this size effect has been investigated on the efficiency of violet, blue, green, and red micro-LEDs.[71,76-81] For instance, Gong *et al.*[71] investigated the impact of chip sizes on the light output power density of violet InGaN-based LEDs, and reported that the smaller size LED delivered higher power density. Hwang *et al.*[78] investigated the size effect on the efficiency of InGaN-based blue micro-LEDs, and reported that those of smaller size exhibited decreased peak EQEs as well as less efficiency droop. This efficiency difference was attributed to etching damage and the improved current spreading of the smaller micro-LEDs. Royo *et al.*[79] investigated the size effect on the efficiency of red AlGaInP-based micro cavity LEDs and reported that smaller LEDs exhibited decreased EQE. This observation was attributed to bad current injection and electron leakage current. It would also be highly interesting to investigate both EQE and WPE efficiency droop behaviors, differential resistance, parasitic series resistance, and the ideality factor of InGaN/GaN blue LEDs with varying chip mesa dimensions.

In this study, we investigated the effect of mesa size on the performance of our fabricated flip-chip (FC) blue LEDs. The mesa geometry of the LEDs was tailored into square shapes with increasing mesa sizes of 08 × 20 mil^2, 10 × 30 mil^2, and 20 × 40 mil^2. We maintained the gaps between the n-contact pads and mesa edges of the micro-

LEDs the same through all the samples, because the current conduction between them influences the current spreading and thus the performance of LEDs.[82] The efficiency droop behaviors were compared for GaN-based blue LED devices with different mesa dimensions. Moreover, the SRRS and ideality factor were derived for the LED devices with different mesa dimensions by fitting the measured I-V characteristics to the diode I-V model.

4.2 Experiments

Blue LED epitaxial wafers were grown on c-axis sapphire substrate using the MOCVD system. The LED structure consisted of a 30-nm GaN buffer layer; a 4-μm unintentionally doped GaN (u-GaN) layer; a 4-μm Si-doped n-type GaN (n-GaN) layer with a doping concentration of 5×10^{18} cm^{-3}; five pairs of $In_{0.15}Ga_{0.85}N$/GaN MQWs with 3-nm-thick InGaN quantum wells and 12-nm-thick GaN quantum barriers; a 20-nm-thick p-type $Al_{0.15}Ga_{0.85}N$ (p-AlGaN) electron blocking layer (EBL); and then a 200-nm-thick Mg-doped p-type GaN (p-GaN) with an effective hole concentration of approximately 3×10^{17} cm^{-3}.

After MOCVD epitaxial growth, the LED wafers were further fabricated into FC blue LEDs with mesa sizes of 08×20 mil^2, 10×30 mil^2, and 20×40 mil^2 following the standard fabrication process of mesa definition, mirror formation, mirror annealing, passivation, and n–p contact definition, and n–p contact formation. The LED mesas were defined on the same wafer using a standard photolithography process, and then the patterns were transferred using ICP etching. Ni/Ag mirrors were deposited by e-beam evaporation and served as the CSL after subsequent annealing. Ti/Au served as n–p contact pads. The electrical characteristics of the LEDs were measured using an LED tester (M2442S-9A Quatek Group), whereas their electroluminescent (EL) light output

power was measured using an integrating sphere attached to an Ocean Optics spectrometer (QE65000) that had been calibrated using a standard light source.

4.3 Results and discussion

All the samples has the same LED structure except for their chip mesa dimension. Their EQE and WPE were extracted with respect to the injection current and injection current density, as shown in Figure 4-1 (a)–(d). The EQE and WPE curves were normalized by dividing their respective peak values for the 08 × 20 mil^2, 10 × 30 mil^2, and 20 × 40 mil^2 LED samples.

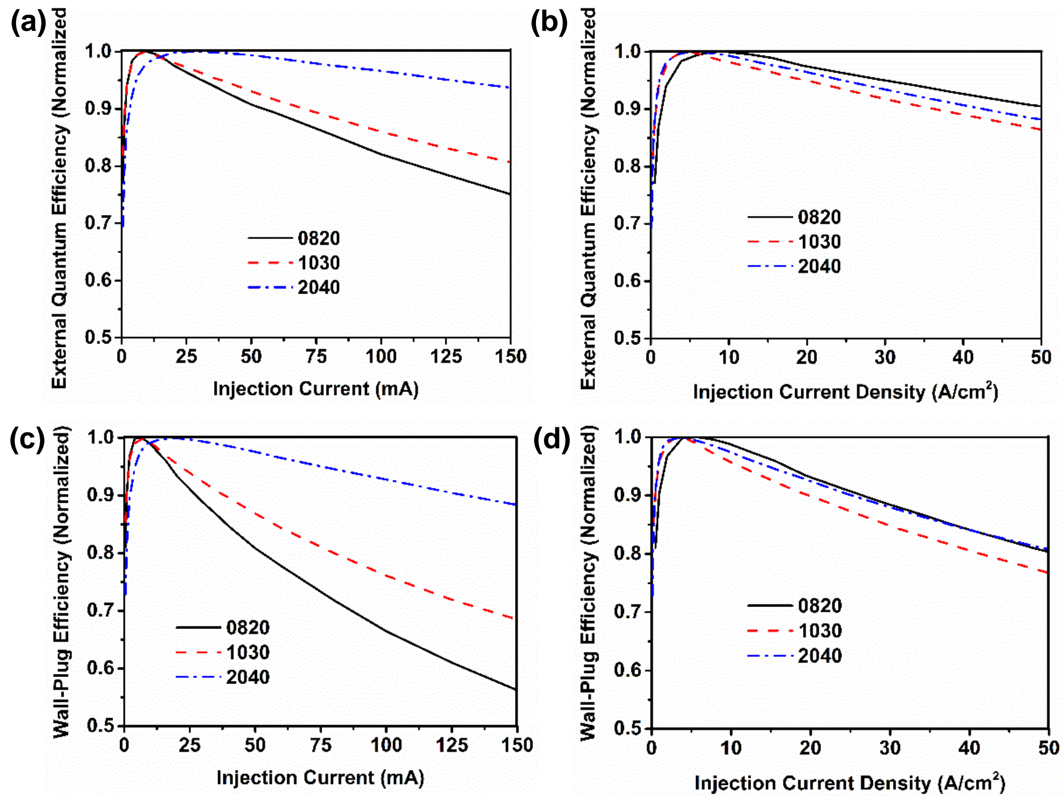

Figure 4-1 Nomalized EQE as a function of (a) injection current and (b) injection current density for the 08 × 20 mil^2, 10 × 30 mil^2, and 20 × 40 mil^2 blue LED samples. Normalized WPE as a function of (c) injection current and (d) injection current density for the three LED samples.

The injection current positions of the peak efficiency were extracted from the EQE and WPE curves and are shown in Figure 4-2 (a) as a function of the chip mesa area ratio. The mesa area of the 08 × 20 mil^2 LED sample was normalized to 1. The positions of the EQE peaks were at 10 mA, 10 mA, and 25 mA for the 08 × 20 mil^2, 10 × 30 mil^2, and 20 × 40 mil^2 LED samples, whereas the positions of the WPE peaks were at 6 mA, 6 mA, and 20 mA.

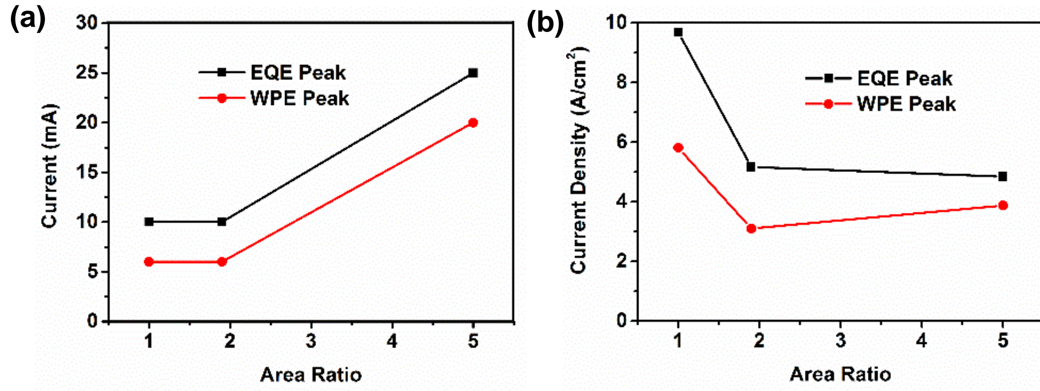

Figure 4-2 (a) Injection current and (b) injection current density positions of the EQE and WPE peaks as a function of the chip mesa area ratio for the 08 × 20 mil^2, 10 × 30 mil^2, and 20 × 40 mil^2 blue LED samples.

This indicated that the WPE drooped at a smaller current injection compared with the EQE of the same LED sample. According to (1-22):

$$\eta_{wall-plug} = \eta_{EQE} \frac{h\nu}{eV} \tag{4-1}$$

The WPE is proportional to η_{EQE}/V. The forward voltage monotonically increases as a function of the injection current. Therefore, the peak value of the WPE may occur at smaller injection currents than that of the EQE. Moreover, the difference between the positions of the EQE and WPE peak depends on the curvature of the EQE-I curve and the slope of the I-V characteristics around the position of the EQE peak. The positions of the EQE peak were the same for the 08 × 20 mil^2 and 10 × 30 mil^2 LED samples, as were those of the WPE peak. This was attributed to the balance between the benefit from the lower current density and the drawback from the poorer current spreading engendered by the enlarged mesa area. Reduced injection current density lowers the carrier leakage and Auger recombination in the MQWs, and thus alleviates the efficiency droop.[83] Poorer current spreading leads to current crowding, thereby aggravatinb the efficiency droop.[16] The positions of the EQE and WPE peaks increased to 25 mA and 20 mA, respectively, for the 20 × 40 mil^2 LED sample. This was ascribed

to the further reduction in the injection current density by the enlarged mesa area.

The effect of current spreading on efficiency droop is revealed in Figure 4-2 (b). The injection current density positions of the peak efficiency were extracted from the EQE and WPE curves and are shown as a function of mesa area ratio. The positions of the EQE peaks were 9.69 A/cm^2, 5.17 A/cm^2, and 4.84 A/cm^2 for the 08 × 20 mil^2, 10 × 30 mil^2, and 20 × 40 mil^2 LED samples, respectively, whereas the positions of the WPE peaks were 5.81 A/cm^2, 3.10 A/cm^2, and 3.88 A/cm^2.

Furthermore, the positions of the EQE and WPE peaks dropped dramatically as the mesa area doubled. This was attributed to the deterioration of current spreading for the LED sample with a larger mesa dimension. However, for the LED sample with an even larger mesa dimension, the position of the EQE peak only dropped slightly because more current spreading fingers were added to facilitate current spreading. Moreover, the WPE peak position of the 20 × 40 mil^2 LED sample exhibited a slight increase compared with that of the 10 × 30 mil^2 LED sample. This was attributed to the reduction of the I-V characteristics slope around the position of the EQE peak.

The slope of the LED I-V characteristics is differential resistance (DFRS) and can be calculated as:[16]

$$r_d = \frac{dV}{dI} \tag{4-2}$$

where r_d is the DFRS of the LED; V is the voltage applied across the LED; and I is the current injected into the LED. The DFRS was calculated as a function of the injection current for the 08 × 20 mil^2, 10 × 30 mil^2, and 20 × 40 mil^2 LED samples, and is shown in Figure 4-3 (a). The relative positions of the three curves indicate that the DFRS

reduced as the chip mesa dimension increased. At a 150-mA current injection, the DFRS values were 5.29 Ω, 2.45 Ω, and 0.929 Ω for the 08 × 20 mil^2, 10 × 30 mil^2, and 20 × 40 mil^2 LED samples, respectively. At the positions of the EQE peak efficiency, the DFRS values were 7.06 Ω and 2.33 Ω for the 10 × 30 mil^2 and 20 × 40 mil^2 LED samples, respectively. This indicated that the 20 × 40 mil^2 LED sample exhibited significant DFRS reductions at the EQE peak compared with the 10 × 30 mil^2 LED sample.

The measured I-V characteristics were also fitted to the diode I-V model:[16]

$$I - \frac{V - IR_S}{R_p} = I_s e^{\frac{e(V - IR_S)}{n_{ideal}kT}} \qquad (4\text{-}3)$$

where R_s is the parasitic SRRS of the LED; R_p is the shunt resistance of the LED; e is the elementary charge; n_{ideal} is the ideality factor of the LED; k is the Boltzmann constant; and T is the junction temperature of the LED. The fitted SRRS and ideality factor after model fitting are shown in Figure 4-3 (b) as a function of the chip mesa area ratio for the 08 × 20 mil^2, 10 × 30 mil^2, and 20 × 40 mil^2 LED samples.

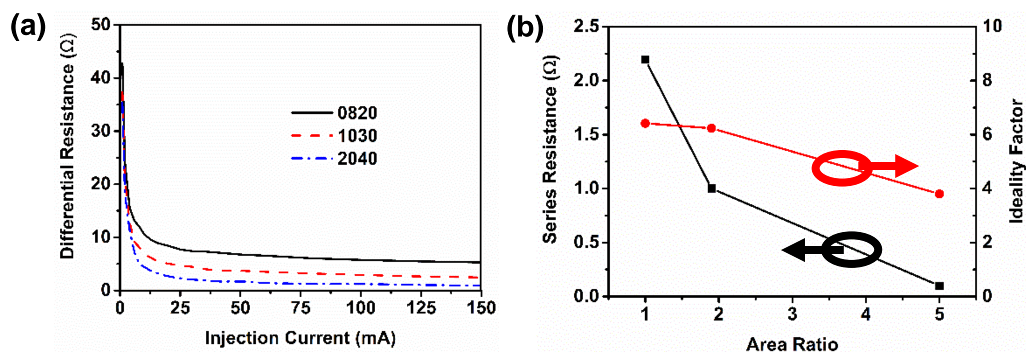

Figure 4-3 (a) Differential resistance (DFRS) as a function of injection current for the 08 × 20 mil^2, 10 × 30 mil^2, and 20 × 40 mil^2 blue LED samples; (b) fitted series resistance (SRRS) and ideality factor as a function of mesa area ratio for the three LED samples.

The slopes of the two lines indicated that both the SRRS and ideality factor of the LEDs decreased as the mesa dimension increased. This implied that the I-V characteristics of a real LED appproach that of an ideal LED as the chip mesa dimension increases. The slopes also indicated that the SRRS decreased faster with a larger mesa dimension, whereas the ideality factor was slower. The SRRS is related to the mesa area of the LED as follows:[16]

$$R_s = r_d|_{I\to\infty} = \frac{dV}{AdJ}|_{J\to\infty} \tag{4-4}$$

where A is the mesa area of the LED and J is the current density injected into the LED. Under a large injection current density, the derivative on the right side approaches a constant, and thus the SRRS is inversely propotional to the mesa area.

4.4 Summary

Efficiency droop behaviors were compared for GaN-based blue LED devices with different mesa dimensions. This study found that the EQE and WPE droop started at higher current injections for LED devices with larger mesa dimensions because of reduced injection current density; however, the EQE droop began at a lower injection current density for LEDs with larger mesa dimensions because of increased current crowding. However, the WPE droop began at slightly higher injection current densities as the mesa dimension of LEDs was further enlarged. This was ascribed to the shallowed slope of the I-V characteristics around the position of the EQE peak. Moreover, the SRRS and ideality factor were derived for the LED devices with different mesa dimensions by fitting the measured I-V characteristics to the diode I-V model. Both the SRRS and ideality factor decreased as the mesa dimensions of the LEDs increased. This implies that the I-V characteristics of a real LED approach those of an ideal LED as the mesa dimension of the LEDs increases. The SRRS and ideality factor were derived by

model fitting.

Chapter 5 Near-UV Micro-LEDs for Enhanced Efficiency and Reduced Droop

5.1 Introduction

Visible micro-pixelated LEDs (micro-LEDs) can be found in a wide range of applications, including visible light communication,[84-94] micro-displays,[95-102] and neuron stimulation.[103] Compared with conventional LEDs, micro-LEDs have exhibited improved optical transitions,[73] LEE,[74] current spreading,[75] and thermal effects.[71] Beyond the visible spectrum, near UV (ultraviolet) micro-LEDs have found their way into the applications[82,84,104-114] such as UV curing[115], pumping sources for full-color displays[116] and near-UV light communications.[117] They have also been proven effective at reducing current crowding,[118] enhancing output power density,[117] and increasing power roll-over current density.[82] In these previous micro-LED studies, device size reduction was not applied to enhance the efficiency or reduce the efficiency droop. Thus, no systematic investigations have been conducted on the size effect on the efficiency enhancement and the efficiency droop reduction. As a result, the physical mechanism that determines the performance enhancement through size reduction in micro-LEDs, especially in the near-UV regime, remains largely unclear. Moreover, whether size reduction increases the forward voltage of near-UV LEDs in the reported findings[117] and what determines such size-dependent voltage remain controversial.

In this study, we clarified these lingering questions using a systematic investigation of the effect of mesa size on the performance of our developed flip chip (FC) 395 nm micro-LEDs. The mesa geometry of the micro-LEDs were tailored into square shapes with increasing side lengths of 25 (0.98), 50 (1.97), 100 (3.94), and 200 (7.87) μm (mil). The p-contact pad of the micro-LEDs was kept away from the mesa edge to prevent

surface recombination on the edge.[82,119,120] The applied injection current and measured optical power of the micro-LEDs were normalized to current and power density by dividing the corresponding mesa areas, thereby separating the size effect from the trivial amplifying effect. Moreover, we kept the gaps between the n-contact pads and mesa edges of the micro-LEDs the same through all the samples, because the current conduction between them influences the current spreading, and thus the performance of micro-LEDs.[82] We measured the size dependent optical power density and forward voltages as a function of the injection current density of the micro-LEDs and observed that those with smaller mesa sizes exhibited EQE enhancement as well as voltage increases. We attributed the voltage increases to the effect of contact resistance on current spreading and derived the relationship between the injection current density and forward voltage from the current spreading model.[121] We attributed the EQE enhancement to the alleviation of the polarization field effect through the strain relaxation,[122,123] which was controlled by mesa sizes. Both the EQE enhancement and voltage increase were supported by numerical simulations using the Crosslight software package's APSYS package.

5.2 Experimental and simulation conditions

The UV LED epitaxial wafers were grown on c-axis sapphire substrate using the MOCVD system. The LED structure consisted of a 30-nm GaN buffer layer; a 4-μm unintentionally doped GaN (u-GaN) layer; a 4-μm Si-doped n-type GaN (n-GaN) layer with a doping concentration of 5×10^{18} cm^{-3}; five pairs of $In_{0.07}Ga_{0.93}N$/GaN MQWs with 3-nm-thick InGaN quantum wells and 12-nm-thick GaN quantum barriers; a 20-nm-thick p-type $Al_{0.15}Ga_{0.85}N$ (p-AlGaN) EBL; and then a 200-nm-thick Mg doped p-type GaN (p-GaN) with an effective hole concentration of approximately 3×10^{17} cm^{-3}.

After MOCVD epitaxial growth, the LED wafers were further fabricated into FC UV micro-LEDs with mesa sizes of 25 × 25 μm^2, 50 × 50 μm^2, 100 × 100 μm^2, and 200 × 200 μm^2 following the standard fabrication process of mesa definition, mirror formation, mirror annealing, passivation and n–p contact definition, and n–p contact formation. The LED mesas were defined on the same wafer using a standard photolithography process, and then the patterns were transferred by ICP etching. Ni/Ag mirrors were deposited using e-beam evaporation and served as the CSL after subsequent annealing. The current spreading region was tailored into square shapes with sizes of 15 × 15 μm^2, 40 × 40 μm^2, 90 × 90 μm^2, and 190 × 190 μm^2, respectively. Ti/Au served as the n and p contact pads of the LEDs. The electrical characteristics of the micro-LEDs were measured using an LED tester (M2442S-9A Quatek Group), whereas the EL light output powers of the micro-LEDs were measured using an integrating sphere attached to an Ocean Optics spectrometer (QE65000) that had been calibrated using a standard light source.

In addition, numerical simulation was performed to reveal the size effect of UV micro-LEDs on their electrical and optical properties. In the simulation, APSYS was used to solve the Poisson's equation, continuity equation, and Schrödinger equation with proper boundary conditions self-consistently. The self-consistent six-band k·p theory was employed to handle the carrier screening effect in the InGaN quantum wells.[124] The Auger recombination coefficient was set as 1×10^{-30} $cm^6 \cdot s^{-1}$ and the Shockley–Read–Hall (SRH) lifetime was set as 43 ns for electrons and holes.[125] Initially, the polarization induced sheet charge density was set as 40% of the theoretical value at the heterointerfaces because of crystal relaxation through dislocation generation during

growth.[126] Moreover, the energy band offset ratio was set at 70/30 in the InGaN/GaN quantum well regions.[127] The other simulation parameters can be found elsewhere.[128]

5.3 Results and discussion

As shown in Figure 5-1 (a), the injection current density-forward voltage (*J*-*V*) characteristics were measured for the UV micro-LEDs with different mesa side lengths, and they exhibited size-dependent behavior. Those with smaller mesa sizes exhibited higher forward voltages under the same injection current density. However, the simulation results presented quite the opposite picture, as shown in Figure 5-1 (b).

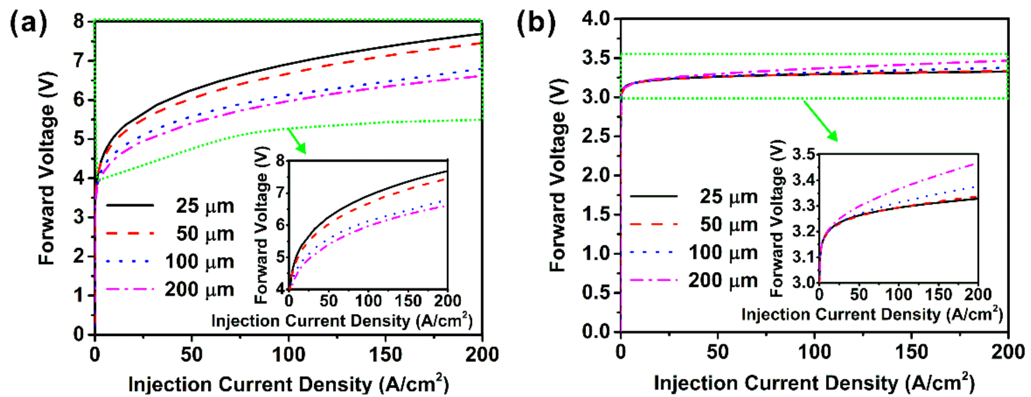

Figure 5-1 Forward voltage as a function of injection current density for (a) experimental measurement and (b) numerical simulation of the micro-LEDs with increasing mesa side lengths.

The greater the mesa size, the higher the forward voltage was under the same injection current density. Furthermore, all sizes exhibited remarkably lower forward voltages under the same injection current density, as compared with that of the experimental results. Moreover, the *J*-*V* curves were quite close to each other.

To resolve the inconsistency between the experimental measurement and numerical simulation, the current spreading model[121] was discussed. A schematic of the LED

structure is presented in Figure 5-2 (a). The mesa size of the LED structure is denoted as $L_m \times L_m$; the size of the p-contact pad is denoted as $L \times L$; L_0 denotes the gap between the p- and n-contact pad edges; t_p and t_n represent the thicknesses of p-GaN and n-GaN, whereas ρ_p and ρ_n denote their resistivity, respectively. Moreover, ρ_c stands for the specific contact resistivity of the p-contact. We also ignored the lateral current spreading in p-GaN above a medium level of injection.[129] Accordingly, an equivalent circuit model of Figure 5-2 (a) is shown in Figure 5-2 (b) and the current density under the p-contact, which extends from the edge of p-contact, can be expressed as[121]

$$J(x) = J(0)\exp(-x/L_s) \tag{5-1}$$

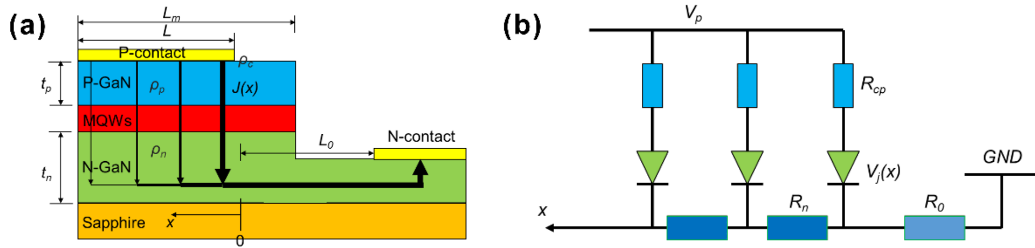

Figure 5-2 (a) Schematic micro-LED structure with current spreading and (b) a corresponding equivalent circuit.

where x is the distance from the edge of the p-contact and L_s denotes the current spreading length; that is

$$L_s = \sqrt{(\rho_c + \rho_p t_p) t_n / \rho_n} \tag{5-2}$$

The forward voltage of the LED can be written as

$$V_p = V_j(0) + R_{cp} I_0 \left\{ \exp\left[eV_j(0)/kT \right] - 1 \right\} + LR_0 \int_0^L J(x)dx + V_{on} \tag{5-3}$$

where $V_j(0)$ is the voltage drop cross junction at the edge of the p-contact; I_0 is the junction saturation current; V_{on} is the junction turn-on voltage; e is the elementary charge; k is the Boltzmann constant; T is the absolute temperature; and R_{cp} is the sum of the contact resistance of the p-contact and p-GaN resistance of the area element Ldx; that is

$$R_{cp} = \frac{\rho_c}{Ldx} + \frac{\rho_p t_p}{Ldx} \tag{5-4}$$

R_0 is the n-GaN resistance corresponding to gap L_0; that is

$$R_0 = \frac{\rho_n L_0}{L t_n} \tag{5-5}$$

Moreover, the average current density J_{ave} can be expressed as follows:

$$J_{ave} = \frac{1}{L}\int_0^L J(x)dx \tag{5-6}$$

Inserting Equations (5-1), (5-4), and (5-5) into Equation (5-3) and substituting J_{ave} for J(x) yields

$$V_p = \left\{ \frac{(\rho_c + \rho_p t_p)L}{L_s\left[1 - \exp(-L/L_s)\right]} + \frac{\rho_n L_0 L}{t_n} \right\} J_{ave} + V_{on} \tag{5-7}$$

Given the device dimensions and material properties from our GaN LED devices: ρ_p = 3 Ω·cm, ρ_n = 5 ×10^{-3} Ω·cm, ρ_c = 0.08 Ω·cm^2, t_n = 4 μm, t_p = 0.2 μm, and L_0 = 25 μm; thus, L_s = 800 μm, $\rho_p t_p$ = 6 ×10^{-5} Ω·cm^2, $\rho_n L_0/t_n$ = 0.03 Ω·cm, and $L << L_s$, $\rho_n L_0 L/t_n << \rho_c + \rho_p t_p$, $\rho_c + \rho_p t_p \approx \rho_c$, Equation (5-7) is simplified to

$$V_p = \rho_c J_{ave} + V_{on} \tag{5-8}$$

Substituting the average current density under the mesa J_{mave} for the average current density under the p-contact J_{ave} and denoting α as the ratio of L_m to L yields

$$V_p = \alpha \rho_c J_{mave} + V_{on} \tag{5-9}$$

Equation (5-9) illustrates that the forward voltage of the micro-LED is directly related to the ratio of the mesa size to that of the p-contact and p-contact resistivity. Since the mesa size is the only viable in our model, the junction turn-on voltage was assumed to be the same for the micro-LEDs with different mesa sizes. Moreover, given the four values of mesa size of $L_m \times L_m$ (25 × 25 μm^2, 50 × 50 μm^2, 100 × 100 μm^2, and 200 × 200 μm^2) and corresponding p-contact size of $L \times L$ (15 × 15 μm^2, 40 × 40 μm^2, 90 × 90

μm^2, and 190 × 190 μm^2), α was calculated as 1.67, 1.25, 1.11, and 1.05, respectively. Therefore, the smaller sizes would exhibit a higher forward voltage under the same injection current density, as was observed in our experiment.

Equation (5-9) also predicts that the p-contact resistance assumes responsibility for the increase in the forward voltage of the micro-LEDs, but this was not added into the aforementioned simulation, probably causing the difference between the simulated and experimental results in Figure 5-1. To substantiate this inference, the contact resistance was added into the simulation and the simulation result showed a similar picture to the experimental result, as shown in Figure 5-3. The greater the mesa size, the higher the forward voltage under the same injection current density. Furthermore, the forward voltages had similar values to the experimental results for all LEDs with different mesa sizes because of the extra voltage drop on the contact resistance and different J-V curves separated from each other. However, forward voltage differences between 25 × 25 μm^2 and 50 × 50 μm^2 micro-LEDs as well as between 100 × 100 μm^2 and 200 × 200 μm^2 micro-LEDs seemed larger than the experimental results, which could probably be attributed to dry-etching induced damage[130] on the micro-LEDs in the experiment, which is difficult to account for in the simulation.

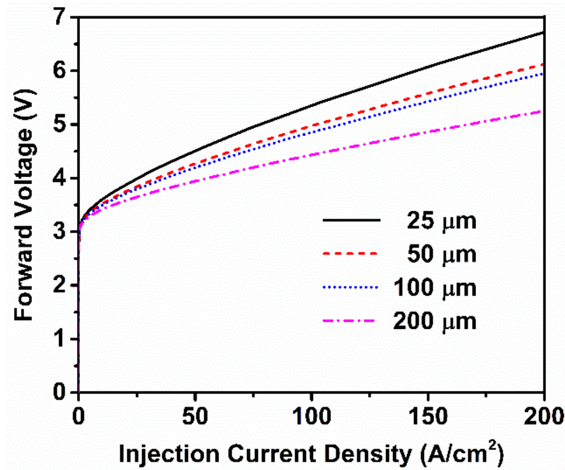

Figure 5-3 Re-simulated forward voltage as a function of the injection current density with p-contact resistance considered.

As shown in Figure 5-4 (a), the light output power density–injection current density (*LD-J*) characteristics were measured for the UV micro-LEDs with different mesa side lengths and the corresponding EQE-injection current density (*EQE-J*) characteristics were extracted from the *LD-J* curves. The *LD-J* characteristics showed size dependent behavior in that the smaller sizes could provide higher light output power densities (LOPDs) under the same injection current density. In other words, the LOPD could be enhanced by decreasing the mesa size of the micro-LED. However, this enhancement became marginal as the mesa size was further scaled down from 50 × 50 μm^2 to 25 × 25 μm^2. Specifically, the 25 × 25 μm^2, 50 × 50 μm^2, 100 × 100 μm^2, and 200 × 200 μm^2 micro-LEDs exhibited LOPDs of 72.8 W/cm^2, 71.4 W/cm^2, 66.3 W/cm^2, and 51.0 W/cm^2, respectively, under an injection current density of 200 A/cm^2. Therefore, at this injection current density, the LOPD could be improved by 40% when the mesa size of the micro-LED decreased from 200 × 200 μm^2 to 50× 50 μm^2. However, further size shrinking from 50 × 50 μm^2 to 25 × 25 μm^2 only resulted in a 2% LOPD improvement at the same injection current density.

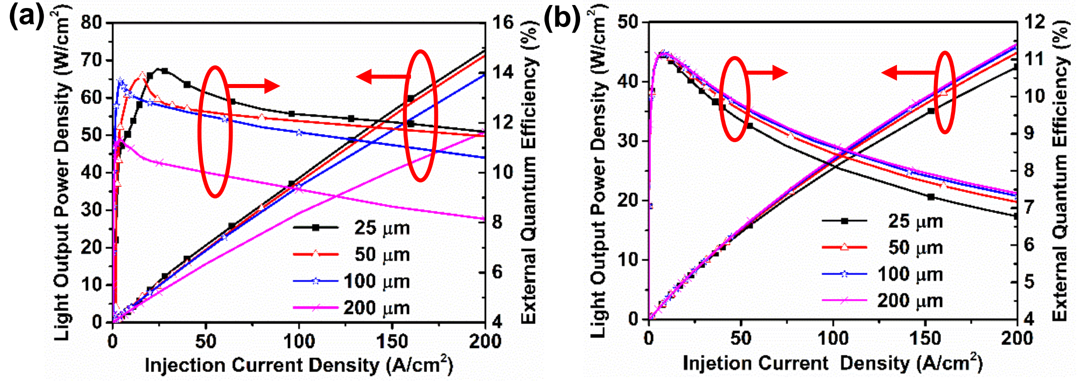

Figure 5-4 LOPD and EQE as functions of the injection current density for (a) experimental measurements and (b) numerical simulations of the micro-LEDs with increasing mesa side lengths.

The EQE-J characteristics indicated that the EQE could be enhanced by decreasing the mesa size of the micro-LEDs above an injection current density of 50 A/cm^2; however, at a low injection current density, the smaller micro-LEDs exhibited lower EQEs. The efficiency droop could be improved as well. The EQE droop at 200 A/cm^2 was defined as[76]

$$\eta_{droop} = \frac{\eta_{peak} - \eta_{200}}{\eta_{peak}} \tag{5-10}$$

where η_{200} and η_{peak} are the EQEs of the micro-LEDs at the injection current density of 200 A/cm^2 and where the EQE reached the peak, respectively. However, all these improvements became marginal when the mesa size further shrank below 50 × 50 μm^2. In addition, the injection current density where the EQE reached the peak shifted to higher current densities. In brief, under an injection current density of 200 A/cm^2, the micro-LEDs of 25 × 25 μm^2, 50 × 50 μm^2, 100 × 100 μm^2, and 200 × 200 μm^2 in size exhibited EQEs of 11.6%, 11.5%, 10.6%, and 8.1%, respectively, and thus the EQE could be enhanced by 30.9% when the mesa size was reduced to 100 × 100 μm^2; however, decreasing the size further only resulted in an 8.5% enhancement from 100 ×

100 μm^2 to 50 × 50 μm^2 and even only 0.9% from 50 × 50 μm^2 to 25 × 25 μm^2. Similarly, the efficiency droops were 18.3%, 17.3%, 22.6%, and 28.3% for the 25 × 25 μm^2, 50 × 50 μm^2, 100 × 100 μm^2, and 200 × 200 μm^2 micro-LEDs, respectively; thus, the efficiency droop could be improved by 38.9% when the mesa size decreased to 50 × 50 μm^2, but further size reductions resulted in degradation. Moreover, the 25 × 25 μm^2, 50 × 50 μm^2, 100 × 100 μm^2, and 200 × 200 μm^2 micro-LEDs reached their EQE peak at 24 A/cm^2, 16 A/cm^2, 4 A/cm^2, and 4 A/cm^2, respectively, and thus the EQE peak shifted from 4 A/cm^2 to 24 A/cm^2 as the mesa size decreased.

These observations seemed to confirm the size effect on the EQE and efficiency droop of the micro-LEDs, and this size effect could probably be attributed to the current spreading effect.[76] More uniform current spreading in the smaller micro-LEDs yielded higher EQEs at a high injection current density. To verify this qualitative analysis, we performed a numerical simulation, the results of which are shown in Figure 5-4 (b). Although the 25 × 25 μm^2 micro-LED exhibited slightly lower LOPDs and EQEs compared with the others under the same injection current density, the other LOPD and EQE curves were quite close to each other. This suggested that the current spreading effect was not the root of the size effect on the EQE and efficiency droop of the micro-LEDs. However, shrinking the size of micro-LEDs also contributes to strain relaxation.[122,123] As reported by Xie *et al.*[123] and Shen *et al.*[122], mesa size reductions release strain, and thus reduce polarization-induced sheet charge density in the MQWs of micro-LEDs. Therefore, in the simulation, we changed the polarization-induced sheet charge density in the MQWs accordingly from a uniform 2.34 × 10^{12} /cm^2 to 1.64 × 10^{12} /cm^2, 1.82 × 10^{12} /cm^2, 1.99 × 10^{12} /cm^2, and 2.34 × 10^{12} /cm^2 for 25 × 25 μm^2, 50 × 50 μm^2, 100 × 100 μm^2, and 200 × 200 μm^2, respectively. The simulation results are

presented in Figure 5-5 (a) and present a similar picture to the experimental results. The smaller the mesa size, the higher the EQE and the lower the efficiency droop under the same injection current density. Moreover, different *LD-J* and *EQE-J* curves separated from each other. However, the simulation showed smaller EQE peak shifts than in the experiment for smaller micro-LEDs, and the EQE differences were also smaller at low injection current densities. To resolve this discrepancy, the injection current density where the IQE reached its maximum could be expressed as[131]

$$J_{\max} = \frac{qdA}{C}\left(B + 2\sqrt{AC}\right) \tag{5-11}$$

where J is injection current density; q is the elementary charge; d is the total quantum well thickness; A is the SRH recombination coefficient; B is the radiative recombination coefficient; and C is the Auger recombination coefficient. It seems that the efficiency peak shifted to higher injection current densities as the defect-related SRH recombination increased. As reported by Tian *et al.*,[76] sidewall defect-related SRH recombination dictates the efficiency peak shift. The SRH recombination coefficient A increases as the ratio of the sidewall perimeter to the mesa area increases. Therefore, we made modifications to the SRH lifetime τ_{SRH} that determined A in the simulation and changed τ_{SRH} from a uniform 43 ns to 40 ns, 43 ns, 53 ns, and 53 ns for the 25×25 μm^2, 50×50 μm^2, 100×100 μm^2, and 200×200 μm^2 LEDs, respectively. The simulation results are presented in Figure 5-5 (b) and present a similar picture to the experimental results, although with slight differences that were probably caused by the dependency of the SRH and Auger recombination coefficients on the carrier concentration as well as the effect of potential fluctuation of InGaN alloys on localized states.[132]

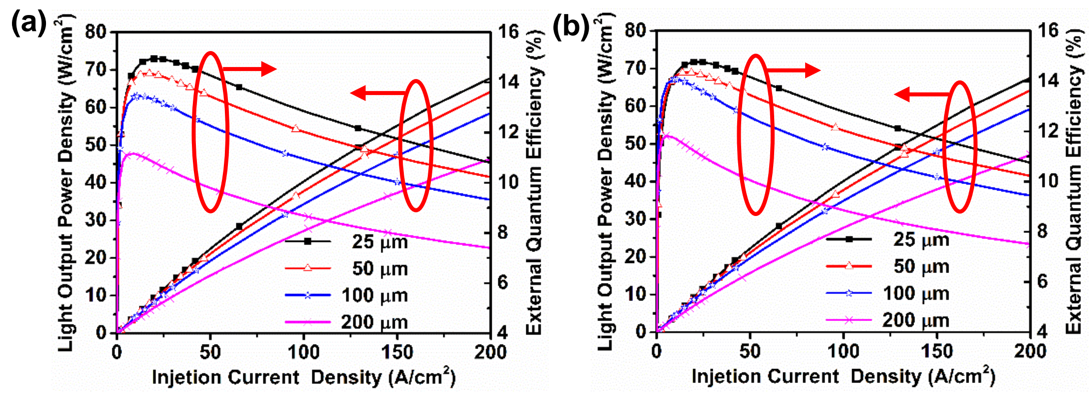

Figure 5-5 Re-simulated LOPD and EQE as functions of the injection current density with (a) strain relaxation and (b) strain relaxation plus sidewall defects considered.

Figure 5-6 (a) and (b) demonstrates the simulated electron and hole concentration profiles along the MQWs under an injection current density of 200 A/cm^2 for the UV micro-LEDs with different mesa side lengths. The electron and hole concentrations in the quantum wells increased as the mesa size of the micro-LEDs decreased. These results suggested that as the mesa size reduction alleviated the polarization field effect in MQWs, more electrons and holes were confined in the quantum wells, and thus fewer of them could escape and form leakage.[65] As a result, the radiative recombination in the quantum wells was enhanced, as shown in Figure 5-6 (c). Therefore, the EQE and efficiency droops of the micro-LEDs were improved, as shown in Figure 4 (a).

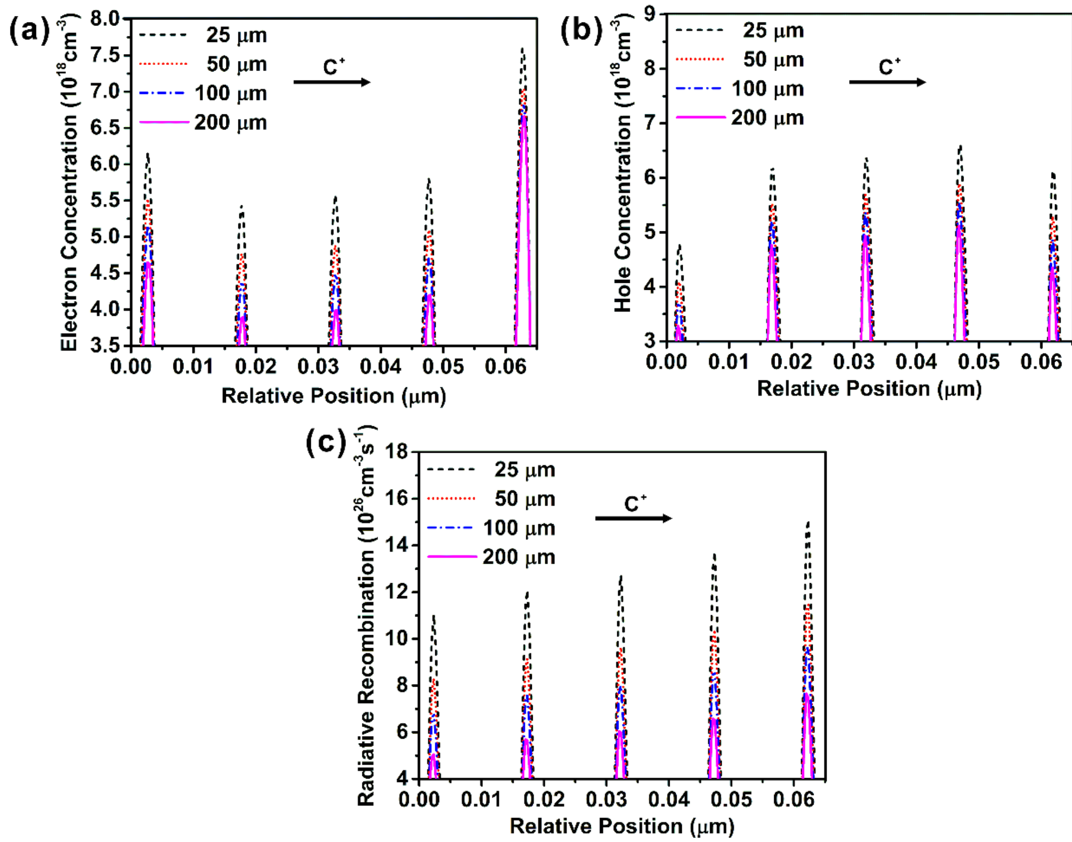

Figure 5-6 Simulated (a) electron concentration, (b) hole concentration, and (c) radiative recombination along the MQWs under an injection current density of 200 A/cm^2.

The observations in the experiment were well supported by the numerical simulation with the introduction of p-contact resistance, strain relaxation, and sidewall defects. Although current spreading effect plays a crucial role in the electrical and optical characteristics of micro-LEDs, it makes little contribution to forward voltage increases, EQE enhancement, efficiency droop alleviation, and efficiency peak shifts of UV micro-LEDs as their mesa size decreases. Instead, p-contact resistance, strain relaxation, and sidewall defects turned out to be the root of the size effect on the electrical and optical characteristics of the UV micro-LEDs.

5.4 Summary

In summary, we investigated the size effect on the electrical and optical characteristics of near UV micro-LEDs. We observed that smaller mesa sizes exhibited higher forward voltages, and we found that the p-contact resistance was responsible for such an observation. Moreover, we observed EQE enhancement and efficiency droop alleviation as the mesa size decreased. These improvements were attributed to strain relaxation in the smaller micro-LEDs, which alleviated the polarization field effect in the MQWs. In turn, this enhanced the confinement of the quantum wells, in which more electrons and holes were confined and thus fewer of them escaped to form leakage. Moreover, the EQE peak shifted to higher injection current densities as the mesa size decreased. We found that sidewall defect-related SRH recombination dictated the efficiency peak shift. The SRH recombination coefficient A increased as the ratio of the sidewall perimeter to the mesa area increased. With the introduction of p-contact resistance, strain relaxation, and sidewall defects, the experimental observations were well supported by the numerical simulation. This report provides insights into the physical mechanism underlying the size effect on the electrical and optical characteristics of near UV micro-LEDs; furthermore, it proposes avenues for enhancing the efficiency and suppressing the efficiency droop of near-UV LEDs. Moreover, we demonstrated that 50×50 μm^2 micro-LEDs produce the optimal performance in terms of efficiency and efficiency droop, which could be used to guide the design of UV LEDs.

Chapter 6 Influence of AlN Composition in Quantum Barriers on the Performance of Near-UV LEDs

6.1 Introduction

The structure of MQWs is a critical component that determines the performance of near-UV LEDs. As the emission wavelength shifts from blue to near-UV, *In* incorporation in the MQWs decreases, and thus the QWs become shallow. This weakens the confinement of the MQWs and increases the carrier overflow.[16] Therefore, the efficiency of near-UV LEDs suffers from low carrier injection. To improve the efficiency of near-UV LEDs, a straightforward approach is to increase the confinement capability of QBs by raising the barrier height. This requires larger band gap differences between the QWs and QBs. By incorporating *Al* into the QBs and increasing the composition of AlN, the barrier height can be increased within the MQW region.[16] Therefore, the carrier concentration in the QWs increases as the AlN composition in the QBs grows and the injection efficiency improves.[133,134] However, higher barrier heights also impede the transport of carriers in the MQW region, thereby aggravating the nonuniform distribution of carriers in MQWs and increasing nonradiative recombination.[16] Moreover, a higher AlN composition increases the polarization charges at the QW/QB interface, thereby increasing the polarization field in the QWs. The polarization field tilts QWs and separate electrons and holes, thereby reducing the radiative efficiency.[133,134] Moreover, a higher AlN composition increases the lattice mismatch between QWs and QBs, and thus degrades the QWs' crystal quality, thereby increasing nonradiative recombination.[16] Therefore, it is necessary to symmetrically investigate the influence of AlN composition in QBs on the performance of near-UV LEDs and determine a device architecture with the optimal AlN composition, which could be used to guide the design of near-UV LEDs.

In this study, the impact of AlN composition in QBs on the performance of near-UV LEDs was systematically studied by adopting multilayer QB structures. The corresponding LED epitaxial wafers were further fabricated into lateral LED devices with a mesa size of 07 $\times$ 09 mil^2. The optical power and forward voltages were measured as a function of the injection current for the corresponding LED devices. The applied injection current and measured optical power were normalized to current and power density by dividing the mesa area. In addition to the electrical characteristics, both the efficiency and efficiency droop behaviors were compared for LED devices with different QB structures.

6.2 Experiments

Near-UV LED epitaxial wafers were grown on c-axis sapphire substrate using the MOCVD system. The LED structure consisted of a 30-nm GaN buffer layer; a 4-μm unintentionally doped GaN (u-GaN) layer; a 4-μm Si-doped n-type GaN (n-GaN) layer with a doping concentration of 5 $\times$ 10^{18} cm^{-3}; eight pairs of $In_{0.08}Ga_{0.82}N$/(Al)GaN MQWs with 2-nm-thick InGaN QWs; a 20-nm-thick p-type $Al_{0.15}Ga_{0.85}N$ (p-AlGaN) EBL; and then a 200-nm-thick Mg-doped p-type GaN (p-GaN) with an effective hole concentration of approximately 3 $\times$ 10^{17} cm^{-3}. The GaN QBs were grown at 1035°C with a pressure of 320 mbar. The TEGa and ammonia flow were set as 48.8 standard cubic centimeters per minute (sccm) and 6500 sccm, respectively, and the growth time was set as 240 s for the GaN QBs.

After MOCVD epitaxial growth, the LED wafers were further fabricated into lateral 390 nm LED devices with a mesa size of 07 $\times$ 09 mil^2 following a standard fabrication

process. ITO was sputtered as a transparent CSL. The electrical characteristics of the LEDs were collected using an LED tester (M2442S-9A Quatek Group), whereas the EL light output power of the LEDs was measured using an integrating sphere attached to an Ocean Optics spectrometer (QE65000) that had been calibrated using a standard light source.

6.3 Results and discussion

6.3.1 GaN-delta-AlGaN QBs for QB6–QB8

In this study, we investigated three structures of the near-UV LED devices with different QB structures for the QB6–QB8. Figure 6-1 presents schematics of the studied LED device structures.

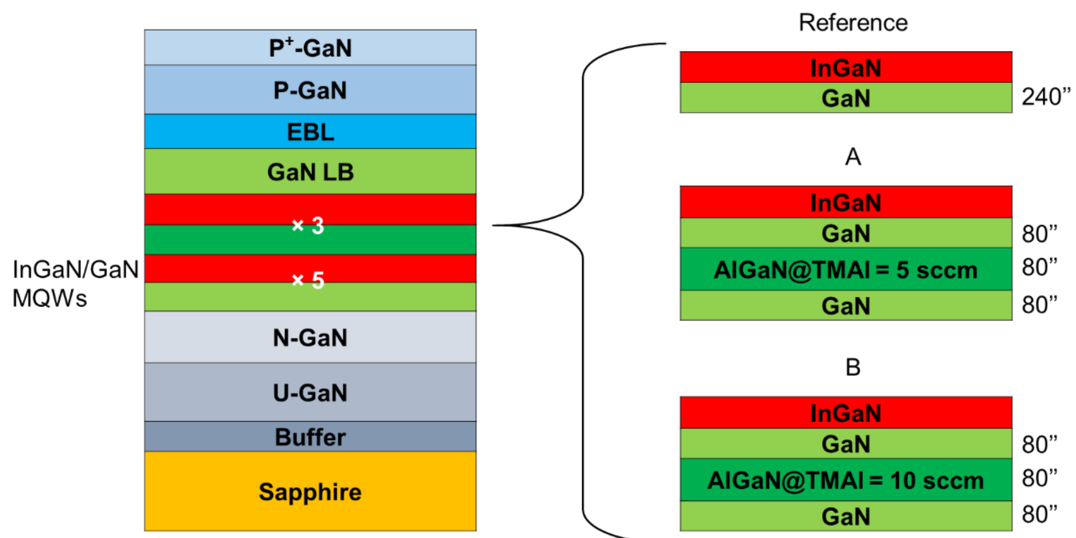

Figure 6-1 Schematics of the studied near-UV LED structures with different QB structures for QB6–QB8: Reference device used GaN as QBs, Device A adopted GaN-delta-AlGaN QBs with AlGaN grown at a TMAl flow of 5 sccm, and Device B used similar QB structures but with AlGaN grown at a TMAl flow of 10 sccm.

The three LED devices were named Reference, A, and B. They have the same structure but differ only in the QB6–QB8. Among the three devices, the Reference device used

GaN as the QBs, whereas Device A featured GaN-delta-AlGaN QBs with AlGaN grown at a TMAl flow of 5 sccm and Device B used similar QBs but with AlGaN grown at a TMAl flow of 10 sccm. The growth of each QB was divided into three 80-s steps under the same temperature, pressure, TEGa, and ammonia flow. AlGaN was grown in the middle step with TMAl supplied.

The schematic band diagrams of the studied Reference device, Device A, and Device B are shown in Figure 6-2 (a), (b) and (c), respectively.

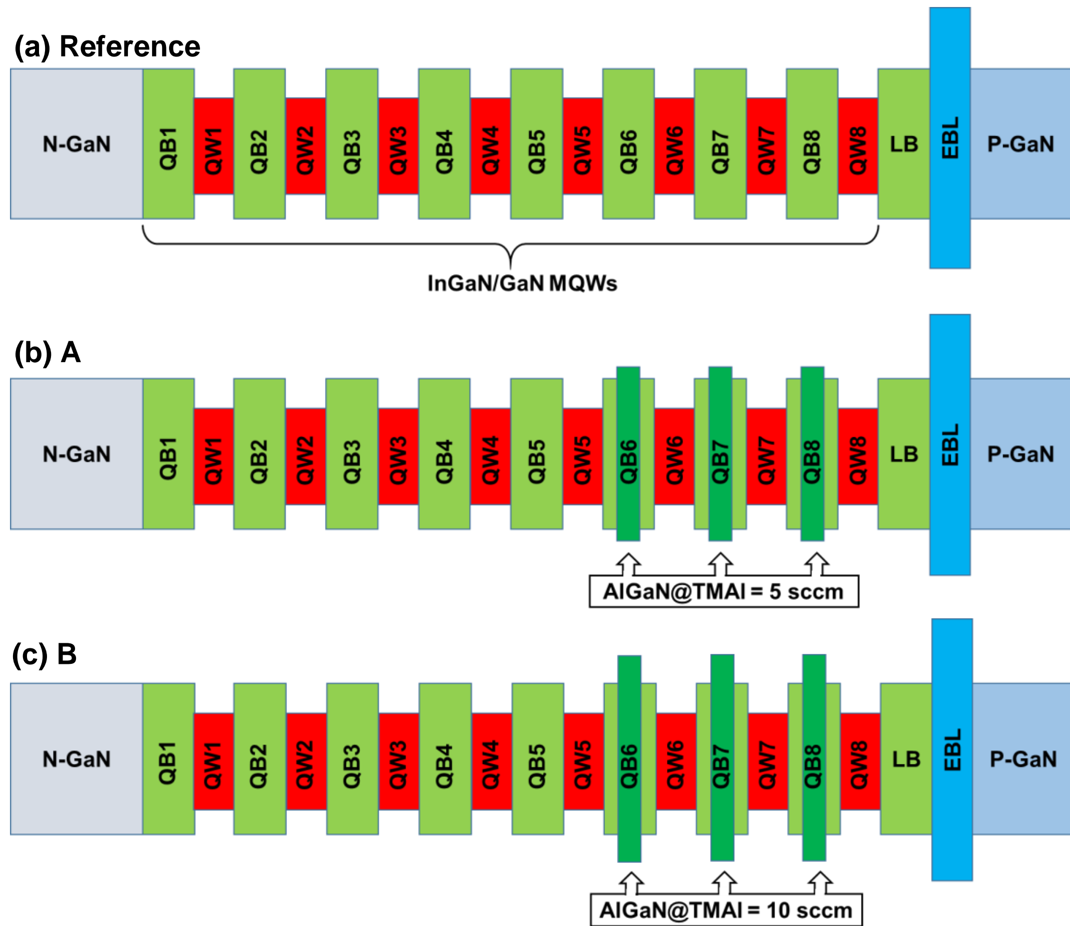

Figure 6-2 Schematic energy band diagrams for the (a) Reference device, (b) Device A, and (c) Device B.

The higher bandgap delta-AlGaN layer can contribute to the confinement capability of the QBs of the QB6–QB8, and thus increase the injection efficiency; however, even

higher AlN composition delta-AlGaN layers could impede the transport of the carriers in the MQW region and deteriorate the nonuniform distribution of carriers in the MQWs, thereby increasing nonradiative recombination.[16,133-135]

As shown in Figure 6-3 (a), the injection current density-forward voltage (*J-V*) characteristics were measured for the Reference device, Device A, and Device B. Devices A and B exhibited higher forward voltages under the same injection current density, indicating that the higher bandgap delta-AlGaN layer might have impeded the carrier transport in the MQWs. At a current injection density of 196.8 A/cm^2, the forward voltages were 3.86 , 3.95, and 3.96 V for Reference, A, and B, respectively.

LOPD–injection current density (*LD-J*) characteristics were measured for the Reference device, Device A, and Device B, and are shown in Figure 6-3 (b). EQE-injection current density (*EQE-J*) characteristics were extracted from the *LD-J* curves. The *LD-J* characteristics showed that Device B could provide the highest LOPD among the three devices under the same injection current density. In other words, the LOPD could be enhanced by adopting GaN-delta-AlGaN QBs for QB6–QB8. However, further increasing the AlN composition of the delta-AlGaN layer resulted in a drop in LOPD at higher injection current densities, although at small current injection densities, Device B still exhibited superior performance. Specifically, the Reference device, Device A, and Device B exhibited LOPDs of 26.9, 29.3, and 25.3 W/cm^2, respectively, under an injection current density of 196.8 A/cm^2; therefore, at this density, the LOPD can be improved by 9.2% when LED devices use GaN-delta-AlGaN QBs with AlGaN grown at a TMAl flow of 5 sccm. The *EQE-J* characteristics also indicated that the EQE could be enhanced by adopting Device B's structure above injection current densities of 50

A/cm^2; however, at low injection current densities, Device B exhibited higher EQEs. In addition, the injection current density where the EQE reached its peak shifted to a lower current density. The EQE droop at 196.8 A/cm^2 was defined as

$$\eta_{droop} = \frac{\eta_{peak} - \eta_{200}}{\eta_{peak}} \tag{6-1}$$

where $\eta_{196.8}$ and η_{peak} are the EQEs of the LED devices at the injection current density of 196.8 A/cm^2 and where the EQE reached its peak. In brief, under an injection current density of 196.8 A/cm^2, the Reference device, Device A, and Device B exhibited EQEs of 4.3, 4.7, and 4.1%, respectively; thus the EQE can be enhanced by 9.3% when LED devices use GaN-delta-AlGaN QBs with AlGaN grown at a TMAl flow of 5 sccm, but further increasing the TMAl flow to 10 sccm would result in slight EQE degradation. Similarly, the peak efficiencies were 5.9, 6.5, and 6.7% for the Reference device, Device A, and Device B, respectively, and thus the peak efficiency can be improved by using GaN-delta-AlGaN QBs. The peak efficiency also increased as the TMAl flow increased. Using the peak efficiency and efficiency at an injection current density of 196.8 A/cm^2, we calculated the efficiency droops to be 27.1, 27.7, and 38.8% for the Reference device, Device A, and Device B, respectively; thus, the efficiency droop will be aggravated when LEDs use GaN-delta-AlGaN QBs. Moreover, the Reference device, Device A, and Device B reached EQE peaks at 39.4, 39.4, and 19.7 A/cm^2, respectively; thus, the EQE peak shifted from 39.4 A/cm^2 to 19.7 A/cm^2 as the TMAl flow increased from 5 sccm to 10 sccm.

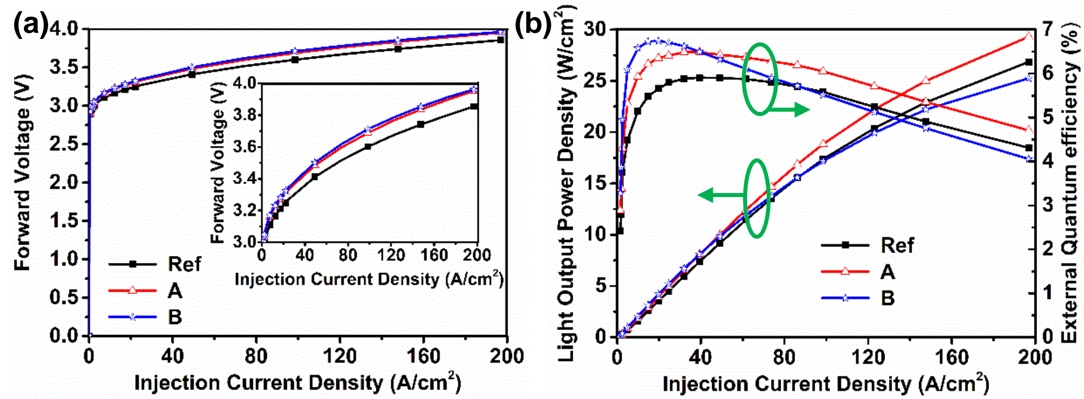

Figure 6-3 Measured (a) forward voltage and (b) LOPD and EQE as functions of injection current density for the Reference device, Device A and Device B.

6.3.2 AlN step composition QBs for QB6–QB8

Based on our study of GaN-delta-AlGaN QBs, the LEDs that used GaN-delta-AlGaN QBs with AlGaN grown at a TMAl flow of 5 sccm exhibited the highest efficiency at high current injection densities, with similar efficiency droops and forward voltages compared with the other two LED structures. Therefore, this LED device structure was used as the reference for investigating another three structures of near-UV LED devices with different QB structures for QB6–QB8. Figure 6-4 present schematics of the studied LED device structures. The four LED devices were named Reference, A, B, and C and differed only in QB6–QB8. For these QBs, Device A featured AlN step composition QBs with AlGaN grown at a TMAl flow of 5 sccm; Device B used similar QBs but with AlGaN grown at a TMAl flow of 10 sccm; and Device C used AlGaN QBs with AlGaN grown at a TMAl flow of 5 sccm. The growth of each QB was divided into three 80-s steps under the same temperature, pressure, TEGa, and ammonia flow. AlGaN was grown in the last two steps for Devices A and B with TMAl supplied, whereas TMAl was supplied throughout the QBs for Device C.

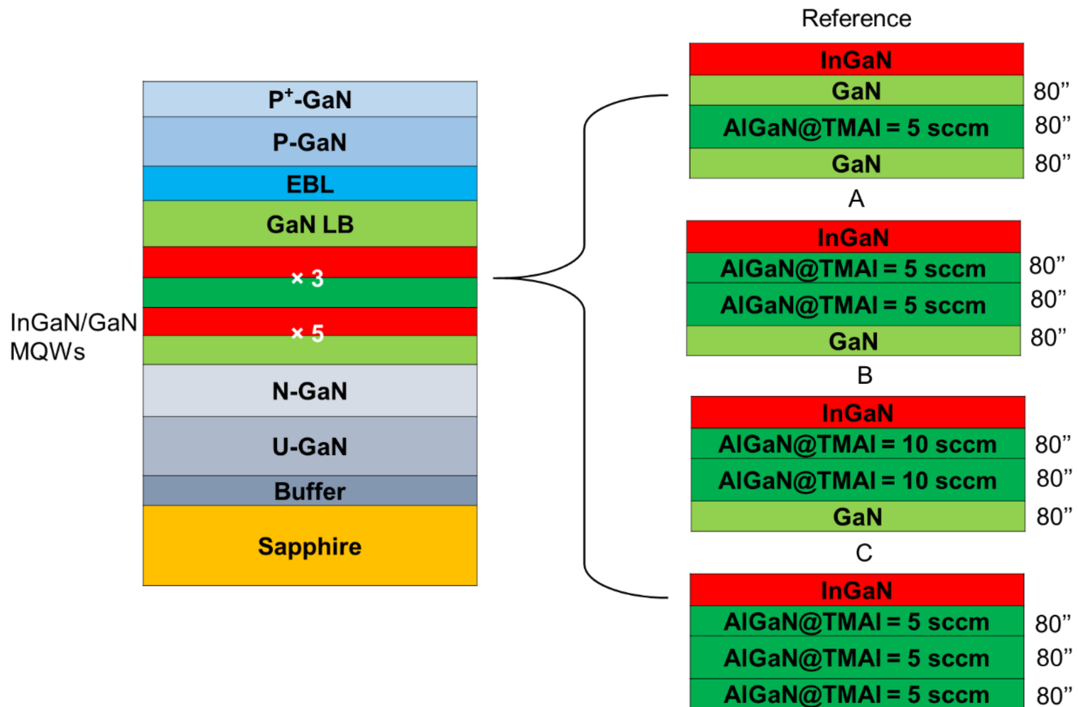

Figure 6-4 Schematics of the studied near-UV LED structures with different QB structures for QB6–QB8: the Reference device used GaN-delta-AlGaN QBs with AlGaN grown at a TMAl flow of 5 sccm; Device A adopted AlN step composition QBs with AlGaN grown at a TMAl flow of 5 sccm; Device B used similar QBs but with AlGaN grown at a TMAl flow of 10 sccm; and Device C used AlGaN QBs with AlGaN grown at a TMAl flow of 5 sccm.

The schematic band diagrams of the studied Reference device, Device A, Device B, and Device C are shown in Figure 6-5 (a), (b), (c), and (d), respectively. The AlN step composition QBs contributed to the confinement capability of the QBs from QB6–QB8, and thus increased the injection efficiency; however, even higher AlN compositions could impede the transport of carriers in the MQW region and deteriorate the nonuniform distribution of carriers in the MQWs, thereby increasing nonradiative recombination.[16,133,134] AlGaN QBs could further increase the confinement capability of QBs.[16]

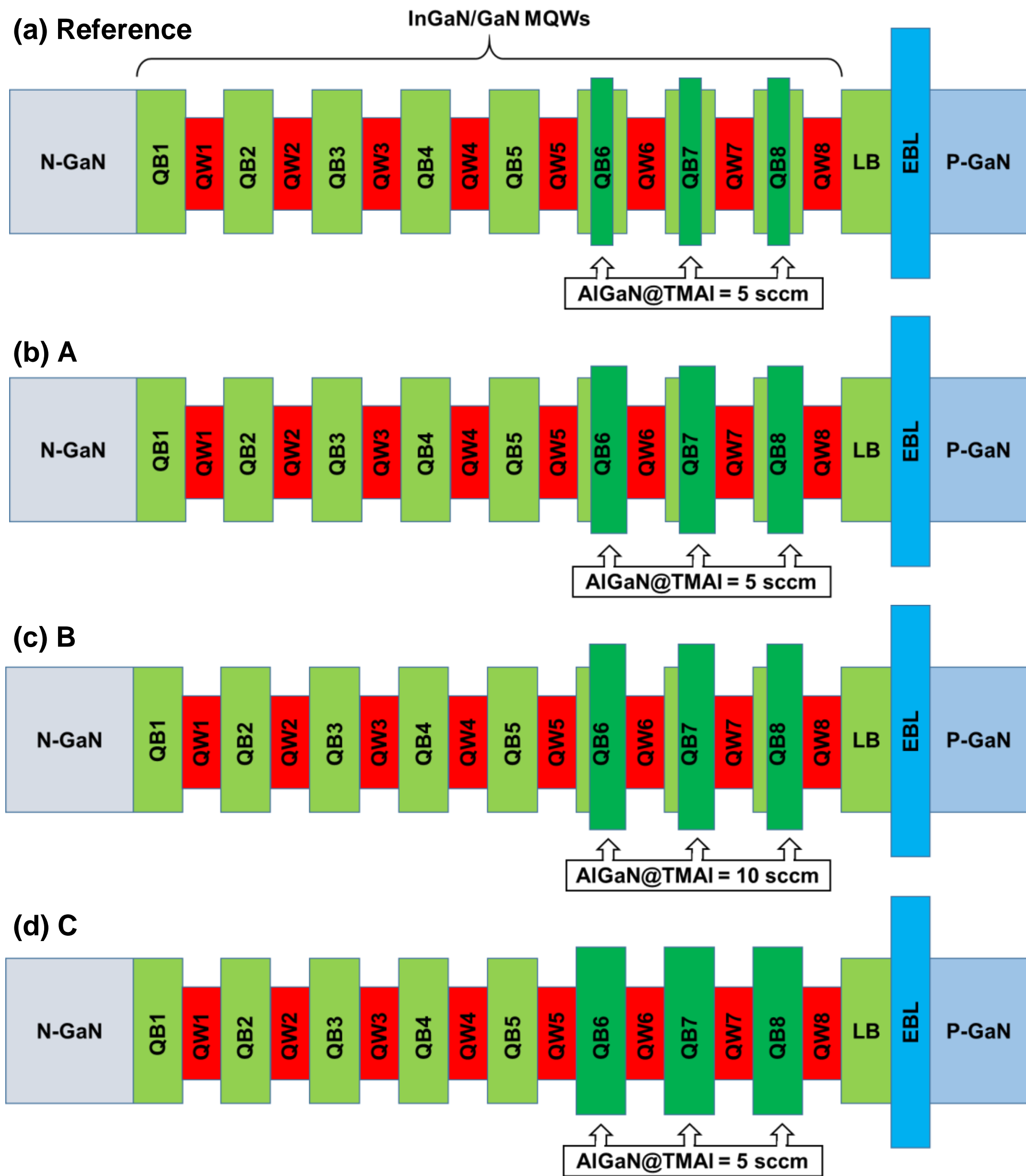

Figure 6-5 Schematic energy band diagrams for the (a) Reference device, (b) Device A, (c) Device B, and (d) Device C.

As shown in Figure 6-6 (a), the *J-V* characteristics were measured for all four devices. Device A exhibited a higher forward voltage under the same injection current density. At a current injection density of 196.8 A/cm^2, the forward voltages were 3.67, 3.91, 3.72, and 3.72 V for the Reference device, Device A, Device B, and Device C, respectively.

As shown in Figure 6-6 (b), the *LD-J* characteristics were measured for all four devices, and *EQE-J* characteristics were extracted from the *LD-J* curves. The *LD-J* characteristics revealed that Device C provided the highest LOPD among the four devices under the same injection current density. In other words, the LOPD can be enhanced by adopting AlGaN QBs for QB6–QB8. However, AlN step composition QBs' structure still slightly improved the efficiency droop. Specifically, the Reference device, Device A, Device B, and Device C exhibited LOPDs of 21.9, 27.5, 25.9, and 33.1 W/cm^2, respectively, under an injection current density of 196.8 A/cm^2. Therefore, at this density, the LOPD can be improved by 25.8% when an LED uses AlN step composition QBs with AlGaN grown at a TMAl flow of 5 sccm. However, AlGaN QBs' structure could further enhance the LOPD by 19.6%. The *EQE-J* characteristics also indicated that the EQE could be enhanced by adopting Device C's structure, whereas Device A exhibited alleviated efficiency droop. In addition, the injection current density where the EQE reached its peak shifted to a lower current density for Device C. In brief, under an injection current density of 196.8 A/cm^2, the Reference device, Device A, Device B, and Device C exhibited EQEs of 3.5, 4.4, 4.2, and 5.3%, respectively; thus the EQE can be enhanced by 25.7% when an LED uses AlN step composition QBs with AlGaN grown at a TMAl flow of 5 sccm; however, AlGaN QBs' structure further improved the EQE by 20.5%. Similarly, the peak efficiencies were 6.0, 5.3, 5.2, and 8.2% for the Reference device, Device A, Device B, and Device C, respectively, and thus, the peak efficiency can be improved by using the AlGaN QB structure.

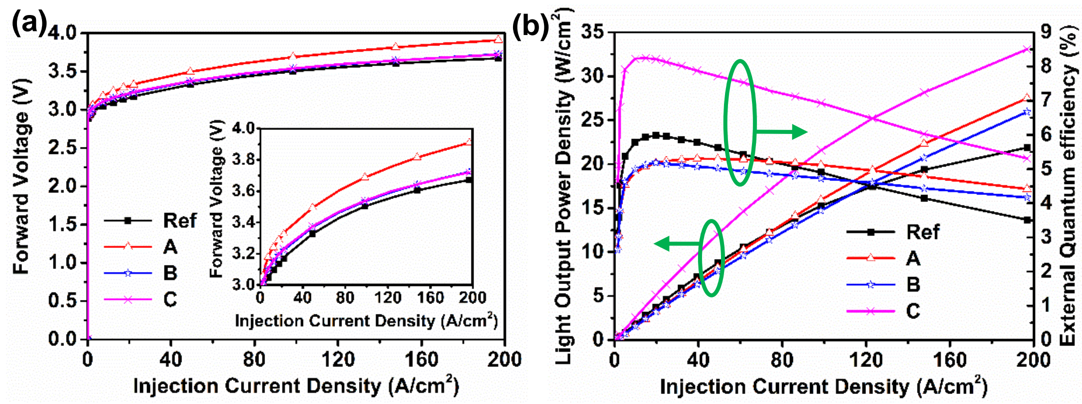

Figure 6-6 Measured (a) forward voltage and (b) LOPD and EQE as functions of the injection current density for the Reference device, Device A, Device B, and Device

Using the peak efficiency and efficiency at an injection current density of 196.8 A/cm^2, the efficiency droops were calculated as 41.7, 17.0, 19.2, and 35.4% for the Reference device, Device A, Device B, and Device C, respectively; thus, the efficiency droop was alleviated in the LEDs that used AlN step composition QBs and AlGaN QBs. Moreover, the Reference device, Device A, Device B, and Device C reached EQE peaks at 19.7, 39.4, 19.7, and 14.8 A/cm^2, respectively; thus the EQE peak shifted from 19.7 A/cm^2 to 14.8 A/cm^2 as the LEDs' QB structure shifted from GaN-delta-AlGaN QBs to AlGaN QBs.

6.3.3 GaN/AlGaN last QB

Based on the previous study, the LED that used AlGaN QBs with AlGaN grown at a TMAl flow of 5 sccm exhibited the highest efficiency, alleviated efficiency droop, and a similar forward voltage. Therefore, we used this LED device structure as a reference and investigated another two near-UV LED devices with different QB structures for the last QB. Figure 6-7 presents schematics of the studied LED device structures.

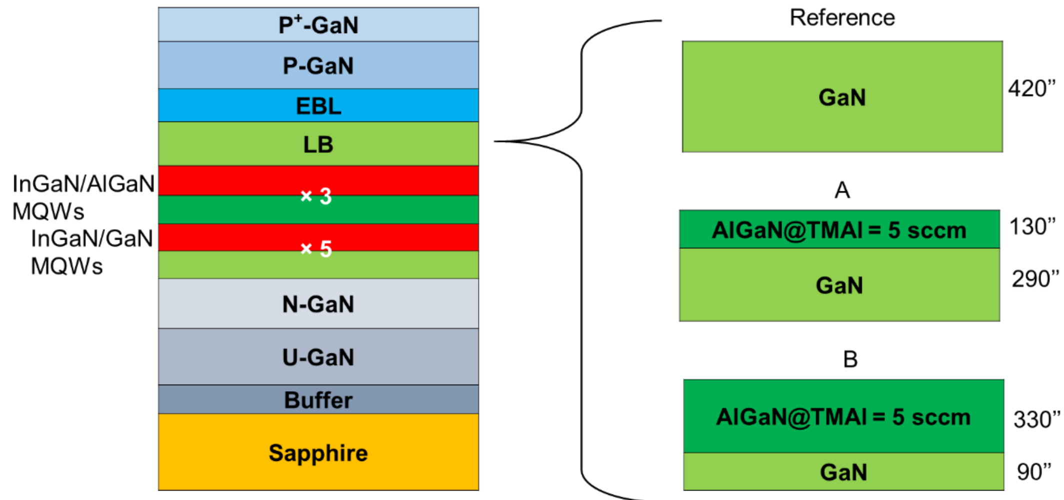

Figure 6-7 Schematics of the studied near-UV LED structures with different QB structures for the last QB: the Reference device used GaN last QB, Device A adopted GaN/AlGaN last QB with AlGaN grown at a TMAl flow of 5 sccm in the last 130 s, and Device B used a similar last QB but with AlGaN grown in the last 330 s.

The three LED devices were named Reference, A, and B and differed only in the last QB. Devices A and B featured GaN/AlGaN last QB with AlGaN grown at a TMAl flow of 5 sccm. The growth of each QB was 420 s in total under the same temperature, pressure, TEGa, and ammonia flow. AlGaN was grown in the last 130 s for Device A and the last 330 s for Device B with TMAl supplied.

The schematic band diagrams of the studied Reference device, Device A, and Device B are shown in Figure 6-8 (a), (b), and (c), respectively. The GaN/AlGaN last QB could contribute to the confinement capability of the last QB and increase the injection efficiency.[136]

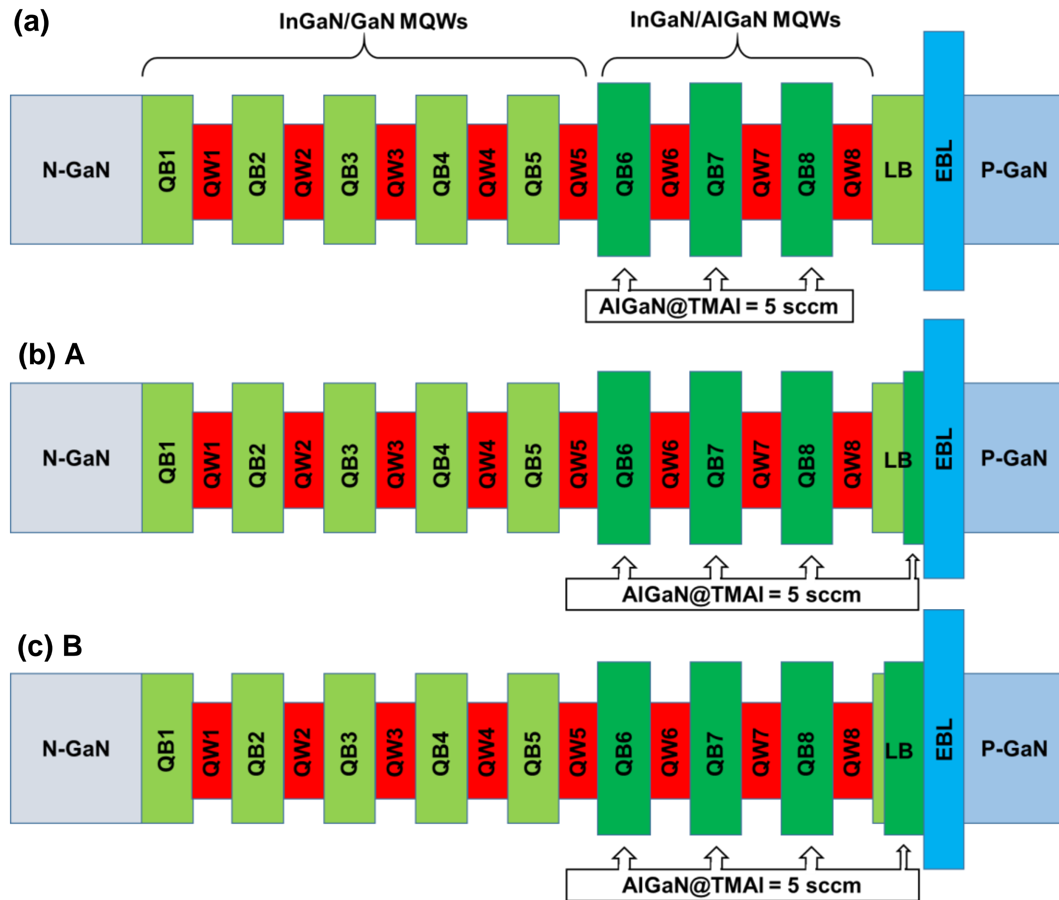

Figure 6-8 Schematic energy band diagrams for the (a) Reference device, (b) Device A, and (c) Device B.

As shown in Figure 6-9 (a), the *J-V* characteristics were measured for all three devices. Devices A and B exhibited similar forward voltages but slightly ones than that of the Reference Device under the same injection current density. At a current injection density of 196.8 A/cm^2, the forward voltages were 3.72, 3.78, and 3.76 V for the Reference device, Device A, and Device B, respectively.

As shown in Figure 6-9 (b), *LD-J* characteristics were measured for the three LEDs, and *EQE-J* characteristics were extracted from the *LD-J* curves. The *LD-J* characteristics revealed that Device B provided a slightly higher LOPD than did the other two devices under the same injection current density below 120 A/cm^2; however, at a high current injection density, Device A still exhibited slightly superior performance. In other words,

the LOPD can be enhanced by adopting GaN/AlGaN last QB. Specifically, the Reference device, Device A, and Device B exhibited LOPDs of 33.1, 34.7, and 33.5 W/cm^2, respectively, under an injection current density of 196.8 A/cm^2. Therefore, at this density, the LOPD can be improved by 5.2% if an LED device uses GaN/AlGaN last QB with AlGaN grown at a TMAl flow of 5 sccm in the last 130 s, but further increasing the growth time of AlGaN from 130 s to 330 s would increase the LOPD of the LED by only 1.5%. The *EQE-J* characteristics of the LEDs also indicated that the EQE could be enhanced by adopting GaN/AlGaN last QB. In addition, the injection current density where the EQE reached its peak shifted to a lower current density for Devices A and B. In brief, under an injection current density of 196.8 A/cm^2, the Reference device, Device A, and Device B exhibited EQEs of 5.3, 5.6, and 5.4%, respectively; thus, the EQE can be enhanced by 5.7% if an LED device uses GaN/AlGaN last QB with AlGaN grown at a TMAl flow of 5 sccm in the last 130 s, but further increasing the growth time of AlGaN from 130 s to 330 s would only increase the EQE by 1.9%. Similarly, the peak efficiencies were 8.2, 8.3, and 8.7% for the Reference device, Device A, and Device B, respectively; thus, the peak efficiency can be improved by using the GaN/AlGaN last QB structure. Using the peak efficiency and efficiency at an injection current density of 196.8 A/cm^2, the efficiency droops were calculated as 35.4, 32.5, and 37.9% for the Reference device, Device A, and Device B, respectively; thus, the efficiency droop would be alleviated when an LED device uses GaN/AlGaN last QB with AlGaN grown at a TMAl flow of 5 sccm in the last 130 s. Moreover, the Reference device, Device A, and Device B reached EQE peaks at 14.8, 9.8, and 9.8 A/cm^2, respectively; thus, the EQE peak shifted from 14.8 A/cm^2 to 9.8 A/cm^2 as the LED QB structure shifted from GaN last QB to GaN/AlGaN last QB.

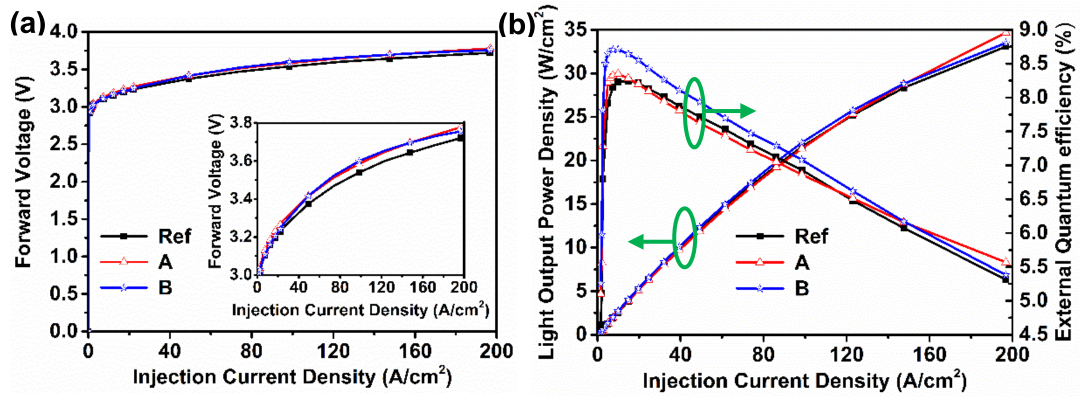

Figure 6-9 Measured (a) forward voltage and (b) LOPD and EQE as functions of injection current density for the Reference device, Device A, and Device B.

6.3.4 Extending AlN composition from QB6–QB8 to QB1–QB5

Based on the previous investigation, the LED device that used GaN/AlGaN last QB with AlGaN grown at a TMAl flow of 5 sccm in the last 330 s exhibited the highest efficiency below current injection densities of 120 A/cm^2 and a similar forward voltage. Therefore, we used this LED device structure as a reference and investigated another two near-UV LED devices with extended AlN compositions from QB6–QB8 to QB1–QB5. Figure 6-10 shows schematics of the studied LED device structures. The three LED devices were named Reference, A, and B and differed only in the QBs of their MQWs. Device A adopted AlN step composition QBs with AlGaN grown at a TMAl flow of 5 sccm for QB3–QB5 and AlGaN QBs for QB6–QB8, whereas Device B used an AlGaN QB structure with AlGaN grown at a TMAl flow of 5 sccm for QB1–QB8. The growth of each QB was 240 s in total under the same temperature, pressure, TEGa, and ammonia flow. AlGaN was grown in the last 160 s in QB3–QB5 for Device A and throughout the QBs in QB1–QB8 for Device B with TMAl supplied.

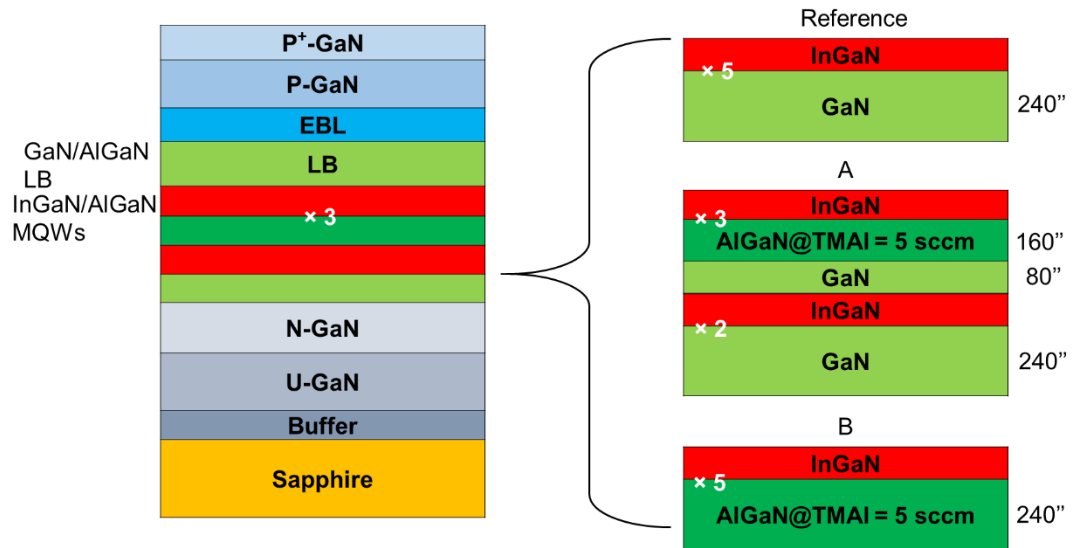

Figure 6-10 Schematics of the studied near-UV LED structures with different QB structures: the Reference device used AlGaN as QBs for QB6–QB8, Device A adopted AlN step composition QBs with AlGaN grown at a TMAl flow of 5 sccm for QB3–QB5 and AlGaN QBs for QB6–QB8, and Device B used the AlGaN QB structure with AlGaN grown at a TMAl flow of 5 sccm for QB1–QB8.

Schematic band diagrams of the studied Reference device, Device A, and Device B are shown in Figure 6-11 (a), (b), and (c), respectively. The extended AlN composition from QB6–QB8 to QB1–QB5 could contribute to the confinement capability of MQWs because of the larger bandgap of AlGaN, thereby increasing the injection efficiency.[133,134,137]

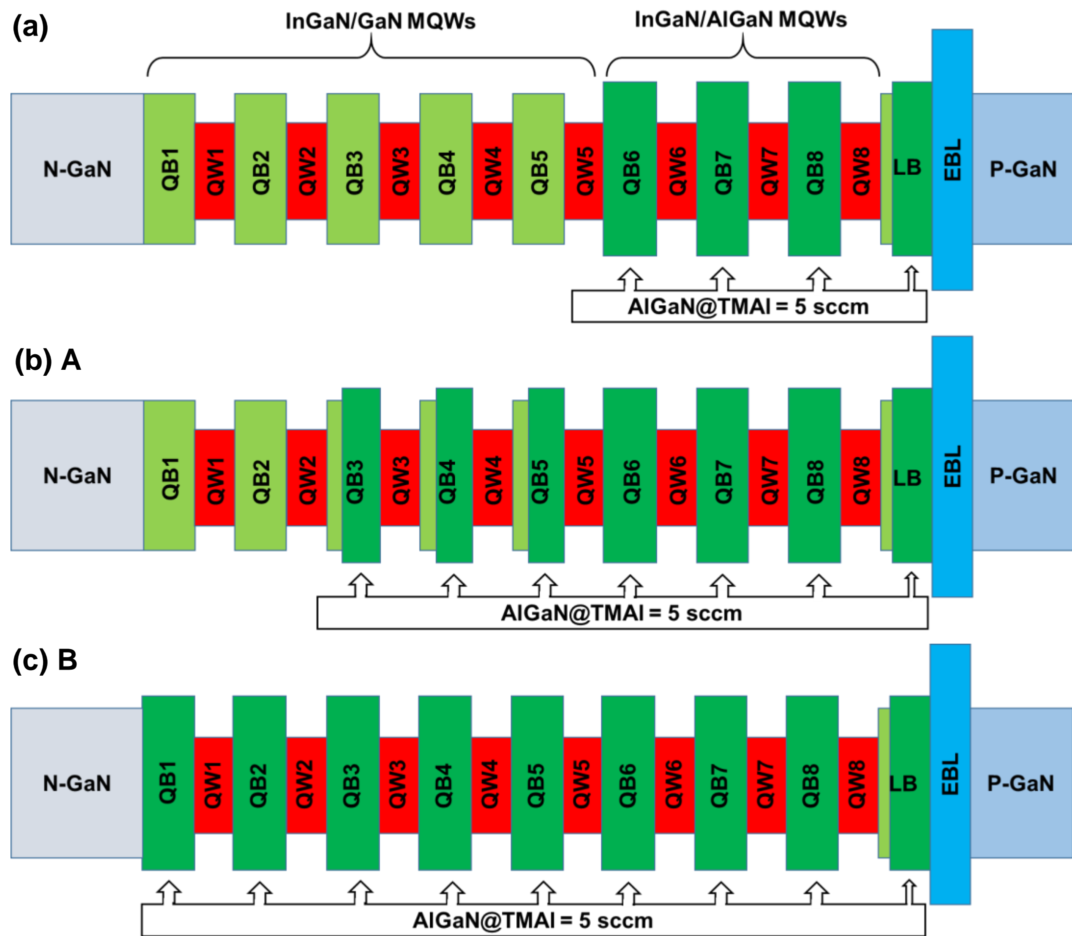

Figure 6-11 Schematic energy band diagrams for the (a) Reference device, (b) Device A, and (c) Device B.

As shown in Figure 6-12 (a), the *J-V* characteristics were measured for the three devices. Devices A and B exhibited similar forward voltages but ones than did the Reference Device under the same injection current density. At a current injection density of 196.8 A/cm^2, the forward voltages were 3.76, 3.85, and 3.84 V for the Reference device, Device A, and Device B, respectively.

As shown in Figure 6-12 (b), *LD-J* characteristics were measured for the Reference device, Device A, and Device B. *EQE-J* characteristics were extracted from the *LD-J* curves. The *LD-J* characteristics revealed that Device B provided the highest LOPD among the three devices under the same injection current density. In other words, the

LOPD could be enhanced by extending the AlN composition from QB6–QB8 to QB1–QB5. Specifically, the Reference device, Device A, and Device B exhibited LOPDs of 33.5, 35.9, and 42.6 W/cm^2, respectively, under an injection current density of 196.8 A/cm^2. Therefore, at this injection current density, the LOPD could be improved by 7.4% when we extended the AlN composition from QB6–QB8 to QB3–QB5; moreover, further extending the AlN composition to QB1–QB2 increased the LOPD by 18.5%. The *EQE-J* characteristics also indicated that the EQE could be enhanced by extending the AlN composition. In addition, the injection current density where the EQE reached its peak shifted to a lower current density for Devices A and B. In brief, under an injection current density of 196.8 A/cm^2, the Reference device, Device A, and Device B exhibited EQEs of 5.4, 5.8, and 6.8%, respectively; thus, the EQE could be enhanced by 7.4% when we extended the AlN composition from QB6–QB8 to QB3–QB5, and further extending the AlN composition to QB1–QB2 increased the EQE by 17.2%. Similarly, the peak efficiencies were 8.7, 9.7, and 11.0% for the Reference device, Device A, and Device B, respectively; thus, the peak efficiency could be improved by extending the AlN composition in the MQWs. From the peak efficiency and efficiency at an injection current density of 196.8 A/cm^2, the efficiency droops were calculated as 37.9, 40.2, and 38.2% for the Reference device, Device A, and Device B, respectively. Moreover, the Reference device, Device A, and Device B reached EQE peaks at 9.8, 4.9, and 4.9 A/cm^2, respectively; thus, the EQE peak shifted from 9.8 A/cm^2 to 4.9 A/cm^2 when the AlN composition was extended in the MQWs.

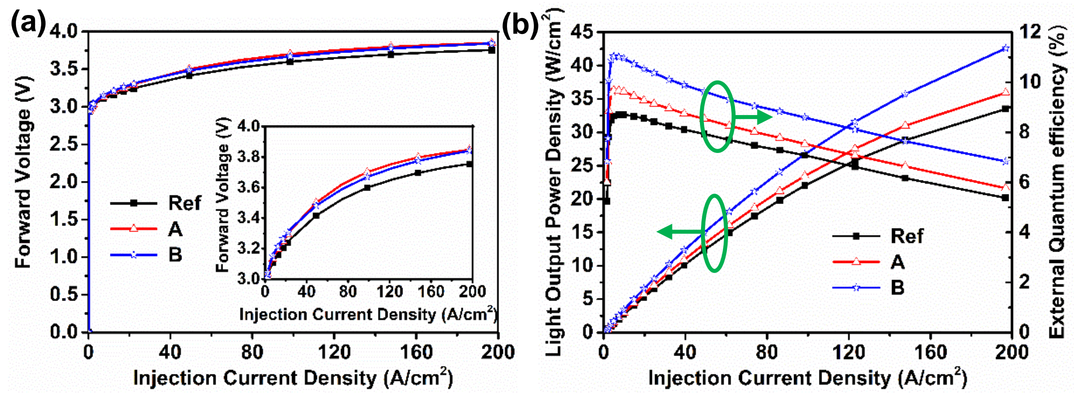

Figure 6-12 Measured (a) forward voltage and (b) LOPD and EQE as functions of injection current density for the Reference device, Device A and Device B.

6.3.5 AlN composition graded AlGaN ILs

Based on the previous study, the LED device that used the AlGaN QB structure with AlGaN grown at a TMAl flow of 5 sccm for QB1–QB8 exhibited the highest efficiency, a similar efficiency droop, and a slightly higher forward voltage. Therefore, we used this LED device structure as a reference and investigated another three structures of near-UV LED devices with different QB structures. Figure 6-13 shows schematics of the studied LED device structures.

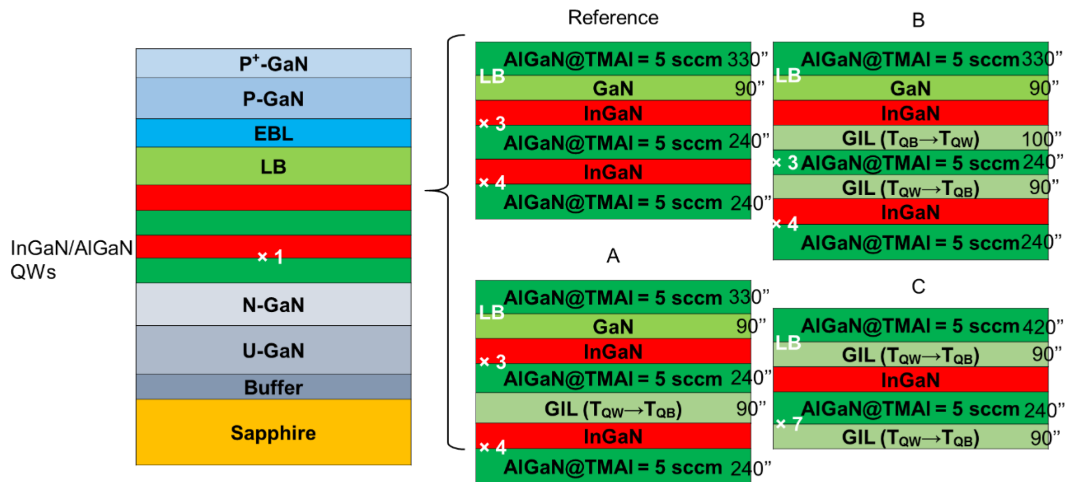

Figure 6-13 Schematic diagrams of the studied near-UV LED structures with different QB structures: Reference device uses the AlGaN QBs structure with AlGaN grown at TMAl flow of 5 sccm for QB1-QB8, Device A incorporates AlN composition graded AlGaN ILs with graded AlGaN ILs grown at temperature ramp up from QWs to QBs for QB6-QB8, Device B also incorporates AlN composition graded AlGaN ILs but with graded AlGaN ILs grown both at temperature ramp up from QWs to QBs and ramp down from QBs to QWs for QB6-QB8, and Device C incorporates AlN composition graded AlGaN ILs with graded AlGaN ILs grown at temperature ramp up from QWs to QBs for QB2 to the last QB.

The four LED devices were named Reference, A, B, and C and differed only in QB structures. Device A incorporated AlN composition graded AlGaN ILs with graded AlGaN ILs grown at a temperature ramp up from QWs to QBs for QB6–QB8; Device B also incorporated AlN composition graded AlGaN ILs but with graded AlGaN ILs grown at a temperature ramp up from QWs to QBs as well as a ramp down from QBs to QWs for QB6–QB8; Device C incorporated AlN composition graded AlGaN ILs with graded AlGaN ILs grown at a temperature ramp up from QWs to QBs for QB2 to the last QB. The growth of each AlGaN QB was 240 s in total under the same temperature, pressure, TEGa, and ammonia flow. AlN composition graded AlGaN ILs were grown under the same conditions except growth temperature; furthermore, the growth time was

90 s for the ramp-up AlN composition graded AlGaN ILs and 100 s for the ramp-down ones.

Schematic band diagrams of the studied Reference device, Device A, Device B, and Device C are shown in Figure 6-14 (a), (b), (c), and (d), respectively. The AlN composition graded AlGaN ILs could improve the carrier transport in the MQWs as well as the lattice mismatch, and thus increased the injection efficiency.[16,138]

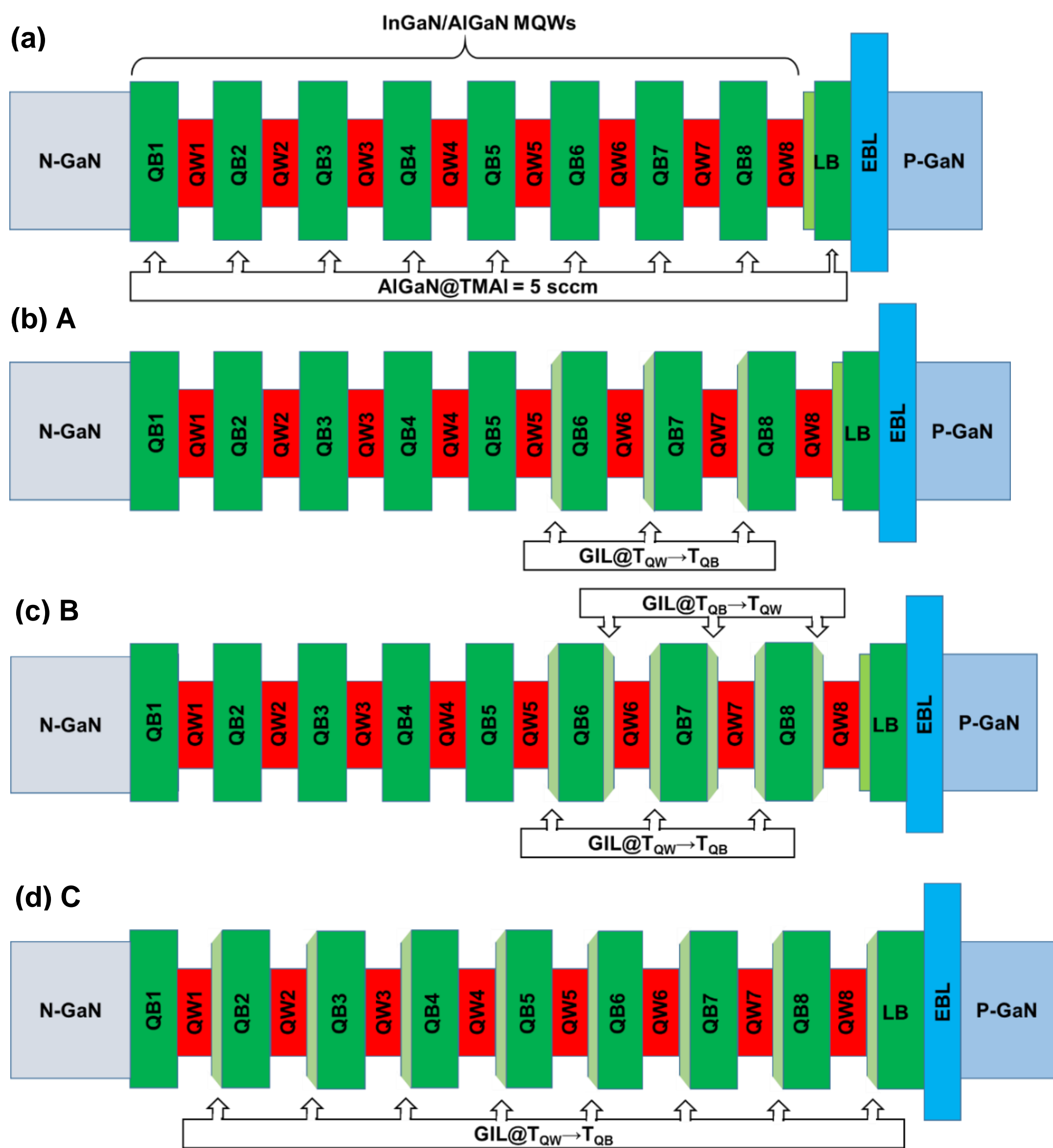

Figure 6-14 Schematic energy band diagrams for (a) Reference device, (b) Device A, (c) Device B and (d) Device C.

As shown in Figure 6-15 (a), the *J-V* characteristics were measured for the four devices. Device A exhibited a slightly higher forward voltage under the same injection current density. At a current injection density of 196.8 A/cm^2, the forward voltages were 3.89, 3.95, 3.84, and 3.89 V for the Reference device, Device A, Device B, and Device C, respectively.

As shown in Figure 6-15 (b), *LD-J* characteristics were measured for the four devices. *EQE-J* characteristics were extracted from the *LD-J* curves. The *LD-J* characteristics revealed that Device C provided the highest LOPD among the four devices under the same injection current density. In other words, the LOPD could be enhanced by adopting AlN composition graded AlGaN ILs for QB2 to the last QB. However, incorporating AlN composition graded AlGaN ILs for QB6–QB8 still improved the efficiency droop. Specifically, the Reference device, Device A, Device B, and Device C exhibited LOPDs of 22.7, 26.4, 28.1, and 30.7 W/cm^2, respectively, under an injection current density of 196.8 A/cm^2. Therefore, at this density, the LOPD could be improved by 35.9% when the LED device used AlN composition graded AlGaN ILs for QB2 to the last QB. The *EQE-J* characteristics also indicated that the EQE could be enhanced by adopting Device C's structure, whereas Devices A and B exhibited alleviated efficiency droops. In addition, the injection current density where the EQE reached its peak shifted to a lower current density for Device C. In brief, under an injection current density of 196.8 A/cm^2, the Reference device, Device A, Device B, and Device C exhibited EQEs of 3.6, 4.2, 4.5, and 4.9%, respectively; thus, the EQE could be enhanced by 36.1% when the LED device used AlN composition graded AlGaN ILs for QB2 to the last QB. Similarly, the peak efficiencies were 6.9, 6.6, 5.8, and 7.6% for the Reference device, Device A, Device B, and Device C, respectively; thus, the peak efficiency could be improved by

using AlN composition graded AlGaN ILs for QB2 to the last QB. From the peak efficiency and efficiency at an injection current density of 196.8 A/cm^2, we calculated the efficiency droops as 47.8, 36.4, 22.4, and 35.5% for the Reference device, Device A, Device B, and Device C, respectively; thus, the efficiency droop can be alleviated when an LED device uses AlN composition graded AlGaN ILs. Moreover, the Reference device, Device A, Device B, and Device C reached EQE peaks at 14.8, 14.8, 19.7, and 9.8 A/cm^2, respectively; thus, the EQE peak shifted from 14.8 A/cm^2 to 9.8 A/cm^2 as the LED device QB structure shifted from AlGaN QBs to AlN composition graded AlGaN ILs incorporated QBs.

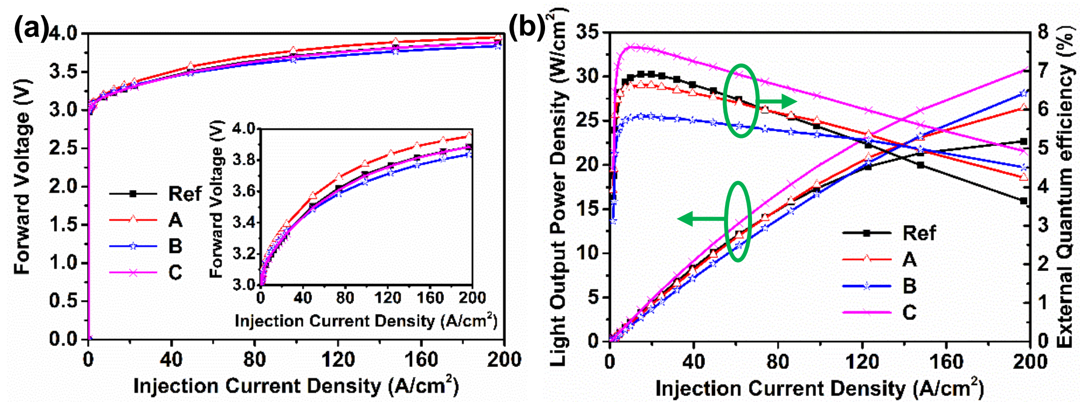

Figure 6-15 Measured (a) forward voltage and (b) LOPD and EQE as a function of injection current density for Reference device, Device A, Device B and Device C.

6.4 Summary

In summary, we systematically studied the influence of AlN composition in QBs on the performance of near-UV LEDs by adopting multilayer QB structures, including GaN-delta-AlGaN QBs for QB6–QB8 with varying AlN compositions; AlN step composition QBs for QB6–QB8 with varying AlN compositions; and GaN/AlGaN last QB with varying AlGaN thicknesses, extending the AlN composition from QB6–QB8 to QB1–QB5, and AlN composition graded AlGaN ILs between QWs and QBs. In addition to

the electrical characteristics, both the efficiency and efficiency droop behaviors were compared for LED devices with different QB structures. Based on our study, we designed, grew, and fabricated an optimal near-UV LED device. This device had a QB structure that adopted AlGaN QBs in QB1 to the last QB and incorporated AlN composition graded AlGaN ILs with graded AlGaN ILs grown at a temperature ramp up from QWs to QBs for QB2 to the last QB. The optimized LED device exhibited a peak efficiency of 7.6% at an injection current density of 9.8 A/cm^2, as well as an EQE of 4.9% and efficiency droop of 35.5% at an injection current density of 196.8 A/cm^2.

Chapter 7 Correlation Between Carrier Diffusion and Efficiency of Deep-UV Structures Based on E-Beam Pumped Deep-UV MQWs

7.1 Introduction

As the emission wavelength shifts further from near-UV to deep-UV, the performance of GaN-based UV LEDs is held back by the low doping efficiency of p-AlGaN (p-type doped AlGaN), and thus non-Ohmic p-contact and electron leakage.[62,139] Therefore, e-beam pumping was proposed as a potential technique[140-154] for the next-generation UV light sources with great environmental and economic benefits.[155] We have started developing e-beam pumped CL structures in the near-UV range and applied our findings to deep-UV structures based on e-beam pumping. The CL power efficiency is defined as the ratio of CL light output power to the e-beam irradiated power. The turning acceleration voltage refers to the experimental acceleration voltage where the CL power efficiency reaches its maximum, or the simulated acceleration voltage where the absorbed energy reaches its maximum.

Cathodoluminescence (CL) from e-beam-pumped MQWs has been reported by several groups.[140,148,156-161] Hospodková et al.[156] compared two curves of the electron acceleration voltage dependent QW CL peak intensity from InGaN/GaN MQW structures with 10 and 30 quantum wells. They observed that the CL intensity decreased after it reached its maximum value, and claimed that the electron beam plunged under the MQWs after the CL intensity achieved its maximum. They also observed higher CL intensity from the MQW structure with a higher QW number and attributed it to the different size of V-pits in the structure with a different QW number. They[157] also compared the CL spectra from these two structures at different acceleration voltages, observing that the QW and defect CL peak intensity increased simultaneously with the

acceleration voltage, although their integral intensity ratio decreased after it reached its maximum, and they suggested that the electrons had penetrated into the deeper part of the MQWs after the ratio reached its maximum. However, they did not explain why the incident-accelerated electrons penetrated below the MQWs after the CL output reached its peak or indicate the factors that could maximize the light output power. We clarified these questions by correlating the carrier diffusion with the CL efficiency of UV InGaN/GaN MQWs and establishing the relationship between the carrier diffusion length and turning CL acceleration voltage. This finding could apply to deep-UV structures based on e-beam pumped MQWs, such as the 100 mW deep-UV structures demonstrated by Oto et al.[140] Moreover, we demonstrated that the MQW structure with 10 QWs produced the optimal efficiency, which could be used to guide the structural design of UV structures based on e-beam pumping.

In this report, we measured the CL characteristics from 380 nm InGaN/AlGaN MQW structures with 8, 10, 15, and 20 QWs and recorded the turning acceleration voltage where the CL power efficiency (PE) reached its maximum. We then attempted to support these observations by simulating the electron trajectories in the MQWs using the Monte Carlo method. However, the simulation results showed a much lower turning acceleration voltage than did the experiment results. We resolved this inconsistency by including the carrier diffusion for carriers that were generated below the MQWs. These carriers then diffused back to the MQWs and contributed to the MQW absorption. Moreover, we demonstrated that the MQW structure with 10 QWs yielded the optimal performance. In this study, we also tested and demonstrated GaN-based deep-UV CL structures, which will be critical for the development of efficient deep-UV emitters.

7.2 Experiments

All epitaxial wafers were grown on c-plane sapphire substrate using a AIXTRON close-coupled showerhead MOCVD system. The epitaxial structure started with a 30-nm-thick GaN buffer layer, followed by a 3-μm-thick unintentionally doped GaN (u-GaN) layer, and then a 3-μm-thick Si-doped n-type GaN (n-GaN) layer with a doping concentration of 5×10^{18} cm^{-3}. Finally, several pairs of $In_{0.03}Ga_{0.97}N/Al_{0.05}Ga_{0.95}N$ MQWs were grown with 2-nm-thick $In_{0.03}Ga_{0.97}N$ QWs and 7.3-nm-thick $Al_{0.05}Ga_{0.95}N$ quantum barriers. A deep-UV LED wafer was purchased from the market with an emission wavelength of 280 nm. The wafer was split into two sample wafers and one was etched off the p-GaN and p-EBL to the MQWs.

We comparatively investigated four structures of MQWs with 8, 10, 15, and 20 pairs of QWs, and schematics of the structures are shown in Figure 7-1 (b). Figure 7-1 (a) depicts the CL measurement setup.

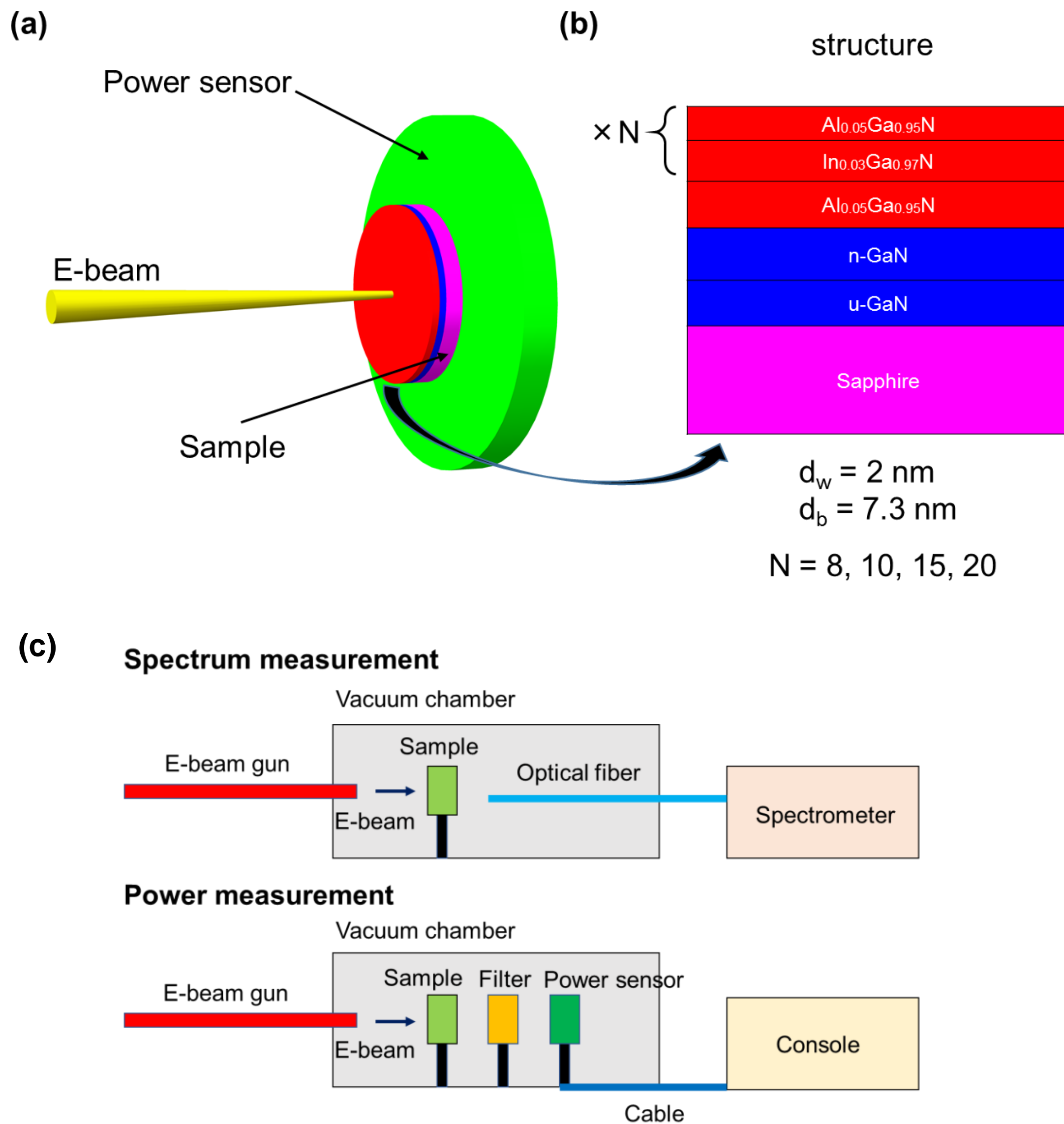

Figure 7-1 Schematic diagram of (a) CL measurement setup (filter not shown), (b) InGaN/AlGaN MQW structures on sapphire substrate and (c) system setup (not to scale)

First, the samples and e-beam gun were loaded in the same vacuum chamber, as shown in Figure 7-1 (c). An optical fiber was placed in close proximity behind the samples and connected to an Avantes spectrometer. A Thorlabs photodiode power sensor (S120VC) was put in place of the spectrometer after CL spectra measurement and connected to the console for power reading display. Furthermore, a UV transparent glass substrate (UG5) was placed between the samples and power sensor and served as a filter. After loading,

the chamber was evacuated to approximately 5×10^{-7} hPa. Subsequently, the samples were irradiated on the surface by e-beam with a spot diameter of 3 mm. The CL spectra of the samples were recorded using the spectrometer and the CL optical power through the filter was measured using the power sensor. A numerical simulation was performed to reveal the variation in the deposited energy in the MQWs with different acceleration voltages using the Monte Carlo method. For the simulation, the CASINO program was used to simulate numerous electron trajectories in the MQWs under various acceleration voltages.[162]

7.3 Results and discussion

Figure 7-2 shows the CL spectra of the MQW structure with eight pairs of QWs over a range of acceleration voltages at an irradiated current of 5 μA. We noted a UV sharp peak at 380 nm and a broad band from 500 nm to 625 nm. Initially, the CL intensity of the broad band grew simultaneously with that of the UV peak as the beam energy increased and rose more rapidly after the acceleration voltage reached 4 kV. The UV sharp peak and the broad band could be attributed to the QW and defect band luminescence, and furthermore, the strong increase of the defect band's CL intensity implied that the incident energetic electrons had penetrated into the deeper part of the MQWs.[157]

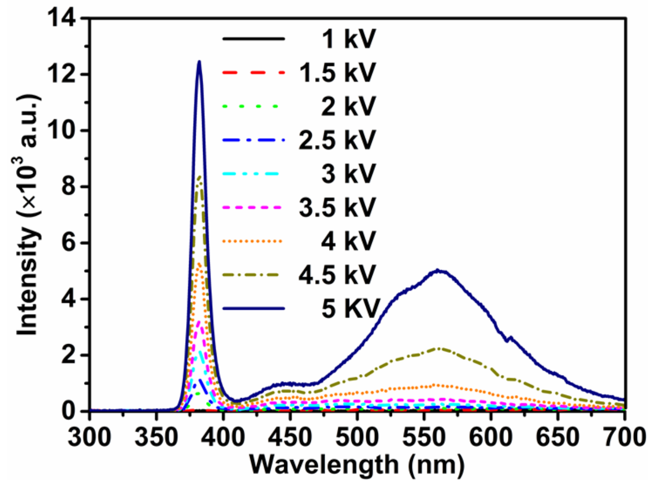

Figure 7-2 Measured CL spectra as a function of acceleration voltage for the MQW structure with 8 pairs of QWs at irradiated current of 5 μA.

Figure 7-3 (a) shows the measured CL PE as a function of acceleration voltage at an irradiated current of 50 μA for the four MQW structures with 8, 10, 15, and 20 pairs of QWs; the four structures exhibited maximum PEs of 0.27, 0.29, 0.23, and 0.19% and reached those maximums at 9, 9, 10, and 13 kV, respectively. Figure 7-3 (b) shows the extracted maximum PE and turning acceleration voltages as a function of the QW number. Therefore, the PE can be improved by increasing the QW number from 8 to 10, but further increasing the QW number will result in a deterioration in efficiency. The MQW structure with 10 QWs demonstrated the optimal efficiency; moreover, the turning acceleration voltage shifted from 9 kV to 13 kV when the QW number increased from 8 to 20.

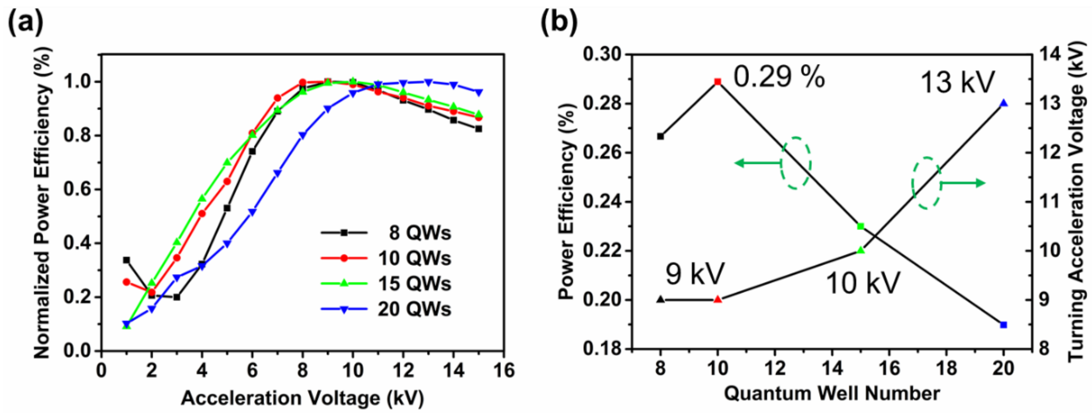

Figure 7-3 (a) Measured CL PE as a function of acceleration voltage at an irradiated current of 50 μA for the four MQW structures with 8, 10, 15 and 20 pairs of QWs and (b) extracted maximum PE and turning acceleration voltages as a function of QW number.

These observations seemed to suggest a connection between the turning acceleration voltage and QW number. To establish this relationship, we simulated the electron trajectories in the MQWs as a function of acceleration voltage using the Monte Carlo method. Figure 7-4 (a) shows the simulation results for the MQW structure with eight QWs; the vertical axis corresponds to the electron energy absorbed in the MQWs and the absorbed energy reached a maximum at 5 kV. To elucidate this absorption maximum, we plotted the depth profiles of the cumulative absorbed energy from the MQWs top at acceleration voltages of 3, 5, and 9 kV (Figure 7-4 (b)). The vertical dashed line in the figure marks the bottom of the MQWs.

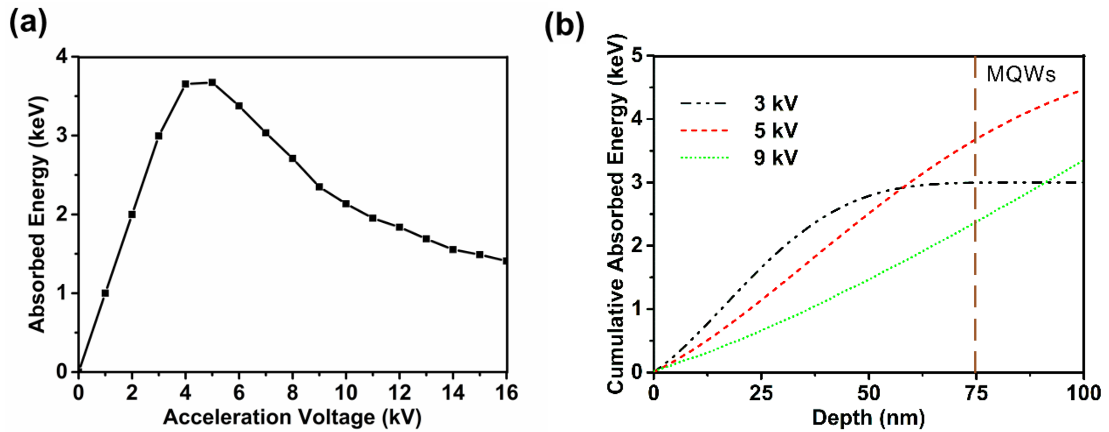

Figure 7-4 (a) Simulated absorbed energy as a function of acceleration voltage for the MQW structure with 8 pairs of QWs. The vertical dashed line marks the bottom of MQWs. (b) Simulated depth profiles of the cumulative absorbed energy from the MQWs top.

The depth profiles revealed that most of the electron energy was absorbed in the MQWs when the acceleration voltage reached 5 kV, and less electron energy was absorbed in the MQWs with either higher or lower acceleration voltages. Because the electrons generally penetrated deeper with higher acceleration voltages, this suggested that if the electrons only reached the QWs close to the surface, the other QWs would not have received sufficient electrons; by contrast, if the electrons penetrated into the MQWs, the they would pass through the MQWs and not be absorbed in the MQWs. Therefore, 5 kV should be the optimal acceleration voltage in terms of maximizing the PE in Figure 7-3 (b). However, the simulation result provided a much lower turning acceleration voltage than in the experiment.

In fact, the carriers generated below the MQWs could diffuse back to the MQWs and contribute to the energy absorbed in them.[161] In other words, the electrons absorbed within the diffusion length below the MQWs generated free carriers, and these carriers still had the chance to travel back and recombine into the MQWs. Therefore, we had to

incorporate an additional segment below the MQWs into the MQW region as well as combine both contributions. Furthermore, we parameterized the contribution from the carrier diffusion from below the MQWs by varying the diffusion length and redid the simulation. The simulation results are shown in Figure 7-5 (a) with the one without diffusion length plotted as a reference; next, the turning acceleration voltages were extracted as a function of diffusion length and are plotted in Figure 7-5 (b). As the diffusion length increased, the turning acceleration voltage shifted to a higher value, and with a diffusion length of 160 nm, the simulation predicted the same turning acceleration voltage as the experiment.

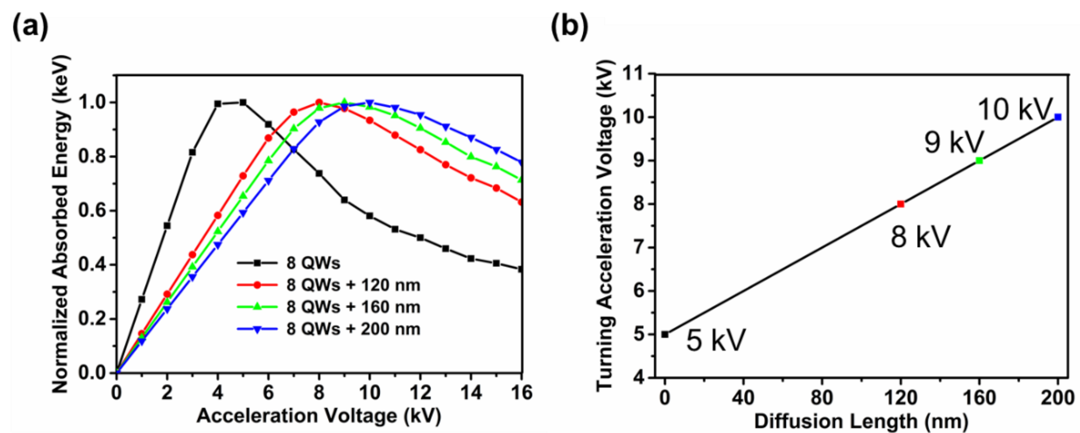

Figure 7-5 (a) Simulated absorbed energy as a function of acceleration voltage for the MQW structure with eight pairs of QWs with and without diffusion lengths, and (b) turning acceleration voltage as a function of diffusion length.

To clarify the effect of diffusion length on the shift in turning acceleration voltage, we plotted the depth profiles of the cumulative absorbed energy from the MQWs' top at acceleration voltages of 5, 8, 9, and 10 kV (Figure 7-6 (a)). The first vertical dashed line in the figure marks the depth of the MQWs and the rest extends an additional 120, 160, and 200 nm as the diffusion length, respectively. Moreover, the cumulative absorbed energies were extracted at these locations for acceleration voltages of 5, 8, 9, and 10 kV, and are shown in Figure 7-6 (b). The electrons penetrated the MQWs at a higher acceleration voltage and were absorbed into the layer below them, which revealed that the MQWs' absorption benefitted from this absorbed energy being converted back into the MQWs by carrier diffusion; thus, the turning acceleration voltage shifted to higher values.

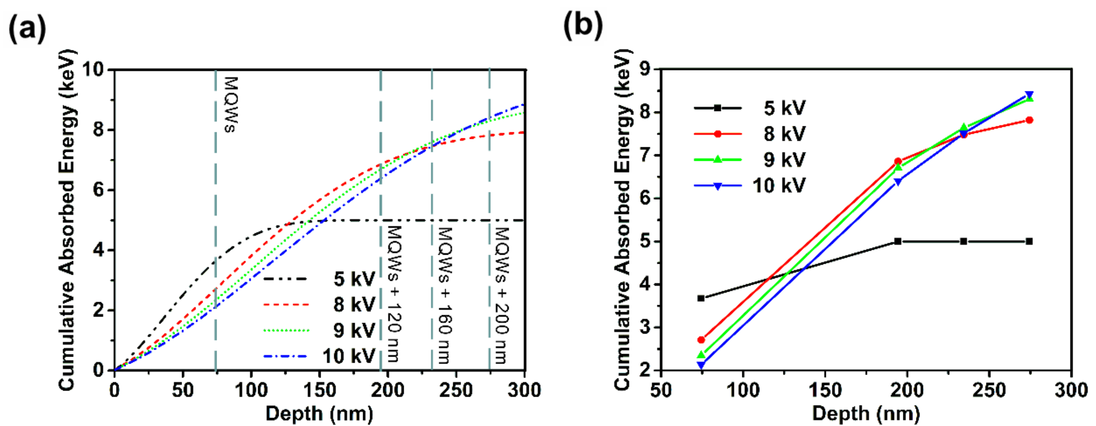

Figure 7-6 (a) Simulated depth profiles of the cumulative absorbed energy from the MQWs' top at acceleration voltages of 5, 8, 9, and 10 kV. The first vertical dashed line marks the depth of the MQWs and the rest extends an additional 120, 160, and 200 nm as the diffusion length, respectively; (b) extracted cumulative absorbed energy at these locations for acceleration voltages of 5, 8, 9, and 10 kV.

With this knowledge, we also simulated the electron trajectories in the MQWs as a function of acceleration voltage for the MQW structures with 10, 15, and 20 QWs; the simulation results are shown in Figure 7-7 (a) along with the one for the MQW structure with eight QWs. We noted that the turning acceleration voltage shifted from 9 kV to 11 kV when the QW number increased from 8 to 20. The turning acceleration voltages were extracted as a function of the QW number and are shown in Figure 7-7 (b) along with the experimental data from Figure 7-1 (b) for comparison. A good agreement was found between the experimental and simulated dependency of the turning acceleration voltage on the QW number before the QW number reached 20; however, the simulated turning acceleration voltage deviated from the experimental value at 20 QWs. The crystal quality of MQWs is anticipated to have already deteriorated when the QW number surpasses a certain critical value.[163,164]

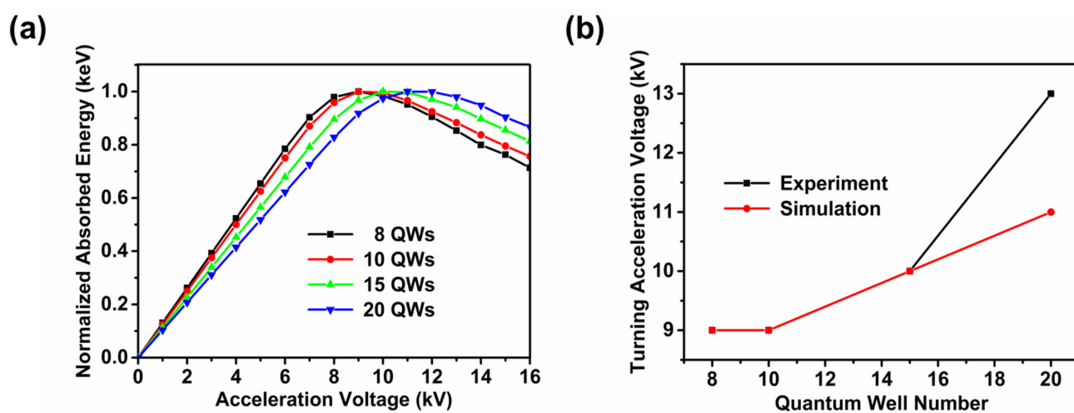

Figure 7-7 (a) Simulated absorbed energy as a function of acceleration voltage for the MQW structures with 8, 10, 15, and 20 pairs of QWs with diffusion length, and (b) extracted turning acceleration voltage as a function of QW number along with the experiment data from Figure 7-1 (b).

Based on our understanding, we measured the CL light output power and PE as a function of irradiated power for the 280 nm deep-UV reference and etched wafer samples; the results are shown in Figure 7-8. At an irradiated power of 360 mW, the reference and etched samples exhibited light output powers of 0.45 and 0.66 mW, respectively. At the same irradiated power, the PE was 0.13 and 0.18%, respectively. Therefore, the light output power was enhanced by 47% and the PE was improved by 38%. As the electrons generally penetrate deeper with a larger acceleration voltage, the incident accelerated electrons need more energy to reach the MQWs of the reference sample due to its additional p-GaN and p-EBL layers. Therefore, at the same irradiated power, more incident electrons can reach the MQWs of the etched sample, resulting in performance enhancement.

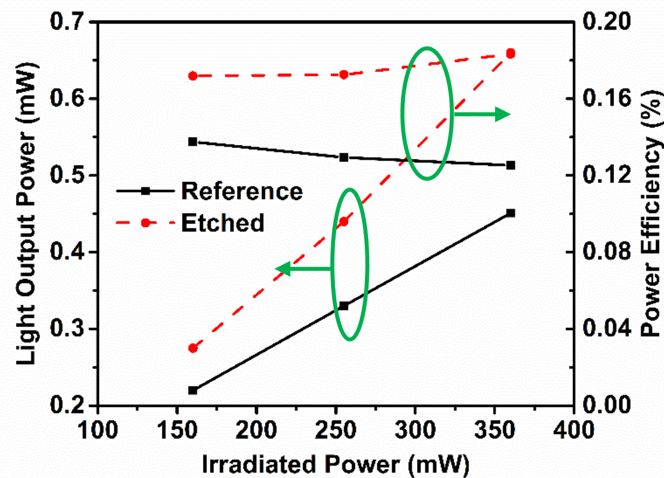

Figure 7-8 Measured CL light output power and PE as functions of irradiated power for the 280 nm deep-UV reference and etched wafer samples.

7.4 Summary

In summary, we measured the CL characteristics from UV InGaN/AlGaN MQW structures with 8, 10, 15, and 20 QWs and recorded the turning acceleration voltage where the CL power efficiency (PE) reached its maximum value. We found that the turning acceleration voltage shifted from 9 kV to 13 kV when the QW number increased from 8 to 20. We then attempted to establish the relationship between the turning acceleration voltage and QW number by simulating the electron trajectories in the MQWs using the Monte Carlo method. However, the simulation result predicted a much lower turning acceleration voltage than the experimental result. We resolved this inconsistency by including the contribution to MQWs' absorption from carriers generated within the diffusion length below the MQWs. With this knowledge, we achieved a good agreement between our experimental observations and simulation predictions before the QW number reached 20. Moreover, we demonstrated that the MQW structure with 10 QWs yielded the optimal performance. This new understanding will assist researchers in designing efficient CL-based UV structures. Finally, we applied our findings to deep-UV structures based on e-beam pumping and enhanced the light output power by 47% and PE by 38%.

Chapter 8 Conclusions and Recommendations

8.1 Conclusion

For this thesis, we successfully developed and established a GaN-based UV LED material and device platform. This platform allowed us to grow high-quality GaN-based epitaxial wafers and demonstrate state-of-the-art devices with lateral, flip chip, and vertical architectures. Our epitaxial wafers covered emission wavelengths from blue to UV with high uniformities of 0.6% at 447.7 nm, 0.492% at 393.6 nm, 0.582% at 386 nm, and 1.445% at 378 nm, which are comparable if not better than the industry standard. Furthermore, our LEDs have respectable performance compared with the industry; for example, our 455-nm flip-chip 20×40 mil^2 LED devices demonstrated a peak efficiency of 31.82% and that of our 393-nm vertical 43×43 mil^2 LED devices reached 28.35%.

Based on this platform, various structures were designed, grown, and fabricated to enhance the performance of InGaN/(Al)GaN blue and near-UV LEDs. In an important study, we designed and investigated near-UV micro-LEDs to enhance their efficiency and reduce their efficiency droop. We found that in addition to the current spreading effect as reported in the blue LEDs by many groups, the strain relaxation, sidewall defect, and p-contact resistance were the root causes of the size effect on the near-UV LEDs' performance. Our work provides insights into the physical mechanisms underlying the size effect and suggests avenues for enhancing efficiency, which could serve as a design rule-of-thumb for UV LEDs.

In a separate study, the low confinement capability of near-UV MQWs, and thus also low carrier injection, were alleviated by raising the barrier height of the QBs of our LED

designs. By incorporating *Al* into the QBs and increasing the composition of Al, the barrier height could be increased within the MQW region. Furthermore, the carrier concentration in the QWs increased as the AlN composition in the QBs grew, leading to improved injection efficiency. The influence of AlN composition in QBs on the performance of near-UV LEDs was systematically studied in this work by adopting multilayer QB structures, including GaN-delta-AlGaN QBs for QB6–QB8 with varying AlN compositions; AlN step composition QBs for QB6–QB8 with varying AlN compositions; GaN/AlGaN last QB with varying AlGaN thicknesses, extending AlN composition from QB6–QB8 to QB1–QB5, and AlN composition graded AlGaN ILs between QWs and QBs. Based on our studies, the optimized near-UV LED device that we developed exhibited the optimal performance. This device uses AlGaN from QB1 to the last QB and incorporates AlN composition graded AlGaN ILs, with graded layers grown while ramping up temperature from QWs to QBs in the case of QB2 to the last QB.

In this thesis, we also explored the possibility of pumping MQWs using e-beam and demonstrated e-beam pumped UV structures. The correlation between the carrier diffusion and efficiency of light sources based on e-beam pumped MQWs was established by including the contribution to MQW absorption from carriers generated within the diffusion length below the MQWs. Based on this physical model, we uncovered the physical mechanism underlying the MQW structure and demonstrated that the device with 10 QWs yielded the optimal performance. Furthermore, we extended our findings and experiments to deep-UV structures based on e-beam pumping and successfully enhanced the light output power substantially. This work shows promising results and could be a potential solution for deep-UV LEDs, which have

notorious problems with epitaxial quality, p-AlGaN, and ohmic contact.

8.2 Recommendations for further research

Through this thesis, we have already improved the performance of near-UV LEDs through novel structural and device solutions, including the size effect and Al incorporated QBs. However, as the emission wavelength shifts further from near-UV to deep-UV, the performance of GaN-based UV LEDs is held back by the low doping efficiency of the p-AlGaN, and thus non-Ohmic p-contact of the LEDs and the electron leakage. Therefore, to improve the doping efficiency of p-AlGaN, it is necessary to lower the effective activation energy of Mg acceptor by designing special structures, such as p-type SLs and polarization doping.

Moreover, because of strong anisotropic emissions from the Al rich AlGaN MQWs, most of the light emitted they emit propagates in the emission plane, where it is reabsorbed and converted into heat. Therefore, to enhance the LEE, facilitating the extraction of TM polarization dominant emissions is critical, which can be achieved by designing light extraction structures such as photonic crystals and inclined sidewalls.

Furthermore, deep-UV LEDs suffer low efficiency, and thus thermal dissipation is a major concern. To reduce the thermal droop, it is desirable to transfer deep-UV LEDs from sapphire to other bonding substrates with high thermal conductivity, such as copper and nickel. Therefore, vertical-structured deep-UV LEDs could provide superior thermal management as well as improve current spreading.

In addition, e-beam pumping has been proposed as a potential technique to bypass the low doping efficiency of p-AlGaN at a high Al mole fraction. Based on our

understanding of the developed e-beam pumped CL structures in the near-UV range, we shall extend our findings to deep-UV structures where p-doping and ohmic contact formation are extremely difficult for GaN-based LEDs. Along with GaN-based deep-UV LEDs, we also propose the promising alternative of e-beam pumped GaN-based MQWs as next-generation, highly efficient, deep-UV structures.

Author's contributions to literature

- **H. Y. Zheng**, S. P. Lu, X. L. Zhang, Y. P. Zhang, P. C. Tsai, S. T. Tan, and H. V. Demir*, Near-UV micro-LEDs for enhanced efficiency and reduced droop: size matters*, (submitted).
- **H. Y. Zheng,** V. K. Sharma, P. C. Tsai, Y. P. Zhang, S. P. Lu, X. L. Zhang, S. T. Tan, and H. V. Demir, *Correlation between carrier diffusion and efficiency of light sources based on e-beam pumped deep-UV MQWs*, (submitted).
- Y. Gao, M. J. Li, S. Delikanli, **H. Y. Zheng**, B. Q. Liu, C. Dang, T. C. Sum, and H. V. Demir, *Low-threshold lasing from colloidal CdSe/CdSeTe core/alloyed-crown type-II heteronanoplatelets*, *Nanoscale*, **10**, 9466 (2018).
- Y. P. Zhang, S. P. Lu, Z. H. Zhang, S. T. Tan, X. L. Zhang, **H. Y. Zheng**, P. C. Tsai, C. Dang, and H. V. Demir, *Experimental observation of electroluminescent cooling in InGaN/GaN light-emitting diodes*, (in submission).

Bibliography

1 S. Nakamura, Rev Mod Phys **87** (4), 1139 (2015).

2 S. Nakamura, T. Mukai, and M. Senoh, Jpn J Appl Phys 2 **32** (1a-B), L16 (1993).

3 T. Mukai, D. Morita, and S. Nakamura, J Cryst Growth **189**, 778 (1998).

4 J. Han, M. H. Crawford, R. J. Shul, J. J. Figiel, M. Banas, L. Zhang, Y. K. Song, H. Zhou, and A. V. Nurmikko, Appl Phys Lett **73** (12), 1688 (1998).

5 A. Kinoshita, H. Hirayama, M. Ainoya, Y. Aoyagi, and A. Hirata, Appl Phys Lett **77** (2), 175 (2000).

6 T. Nishida, H. Saito, and N. Kobayashi, Appl Phys Lett **79** (6), 711 (2001).

7 V. Adivarahan, S. Wu, J. P. Zhang, A. Chitnis, M. Shatalov, V. Mandavilli, R. Gaska, and M. A. Khan, Appl Phys Lett **84** (23), 4762 (2004).

8 H. Hirayama, T. Yatabe, N. Noguchi, T. Ohashi, and N. Kamata, Appl Phys Lett **91** (7) (2007).

9 H. Hirayama, S. Fujikawa, N. Noguchi, J. Norimatsu, T. Takano, K. Tsubaki, and N. Kamata, Phys Status Solidi A **206** (6), 1176 (2009).

10 H. Hirayama, Y. Tsukada, T. Maeda, and N. Kamata, Appl Phys Express **3** (3) (2010).

11 J. R. Grandusky, S. R. Gibb, M. C. Mendrick, C. Moe, M. Wraback, and L. J.

Schowalter, Appl Phys Express **4** (8) (2011).

[12] T. Kinoshita, K. Hironaka, T. Obata, T. Nagashima, R. Dalmau, R. Schlesser, B. Moody, J. Q. Xie, S. Inoue, Y. Kumagai, A. Koukitu, and Z. Sitar, Appl Phys Express **5** (12) (2012).

[13] M. Shatalov, W. H. Sun, A. Lunev, X. H. Hu, A. Dobrinsky, Y. Bilenko, J. W. Yang, M. Shur, R. Gaska, C. Moe, G. Garrett, and M. Wraback, Appl Phys Express **5** (8) (2012).

[14] Noritoshi Maeda and Hideki Hirayama, physica status solidi (c) **10** (11), 1521 (2013).

[15] S. Nakamura, T. Mukai, and M. Senoh, Appl Phys Lett **64** (13), 1687 (1994).

[16] E. Fred Schubert, (Cambridge University Press,, Cambridge, 2006), p. 1 online resource (432 p.).

[17] E. M. Bourim and J. I. Han, Electron Mater Lett **12** (1), 67 (2016).

[18] EnergyStar http://www.energystar.gov/ia/partners/promotions/change_light/downloads/Fact%20Sheet_Lighting%20Technologies.pdf, (2013).

[19] Y. Muramoto, M. Kimura, and S. Nouda, Semicond Sci Tech **29** (8), 084004 (2014).

[20] ElectronicGadgtes http://electronicgadgtes.wordpress.com, (2013).

[21] All-Accesspries-for-Your-Vehicle http://accessories-for-acar.info/led-automotive, (2013).

[22] https://en.wikipedia.org/wiki/Ultraviolet.

[23] A. Zukauskas, M. S. Shue, and R. Gaska, *Introduction to Solid-State Lighting*. (Wiley, New York, 2002).

[24] H. Hirayama, J Appl Phys **97** (9), 091101 (2005).

[25] Joachim Piprek and Wiley InterScience (Online service), (Wiley-VCH; John Wiley distributor, Weinheim Chichester, 2007), pp. 1 online resource (xxi.)

[26] Hadis Morko©*, (Wiley-VCH,, Weinheim, 2013), p. 1 online resource.

[27] M. Suzuki, T. Uenoyama, and A. Yanase, Phys Rev B **52** (11), 8132 (1995).

[28] X. H. Jiang, J. J. Shi, M. Zhang, H. X. Zhong, P. Huang, Y. M. Ding, T. J. Yu, B. Shen, J. Lu, and X. Wang, New J Phys **16** (2014).

[29] J. S. Speck, (2006).

[30] T. Gessmann, Y. L. Li, E. L. Waldron, J. W. Graff, E. F. Schubert, and J. K. Sheu, Appl Phys Lett **80** (6), 986 (2002).

[31] Tae-Yeon Seong, in *Topics in applied physics,* (Springer,, Dordrecht, 2013), pp. 1 online resource (xiii.

[32] S. I. Inoue, N. Tamari, and M. Taniguchi, Appl Phys Lett **110** (14), 5 (2017).

[33] J. R. Grandusky, J. F. Chen, S. R. Gibb, M. C. Mendrick, C. G. Moe, L. Rodak, G. A. Garrett, M. Wraback, and L. J. Schowalter, Appl Phys Express **6** (3), 3 (2013).

[34] M. Kneissl, T. Kolbe, C. Chua, V. Kueller, N. Lobo, J. Stellmach, A. Knauer, H. Rodriguez, S. Einfeldt, Z. Yang, N. M. Johnson, and M. Weyers, Semicond Sci Tech **26** (1), 6 (2011).

[35] G. F. Yang, Q. Zhang, J. Wang, S. M. Gao, R. Zhang, and Y. D. Zheng, IEEE Photonics J. **7** (6), 7 (2015).

[36] J. Yun, J. I. Shim, and H. Hirayama, Appl Phys Express **8** (2), 3 (2015).

[37] T. Kinoshita, K. Hironaka, T. Obata, T. Nagashima, R. Dalmau, R. Schlesser, B. Moody, J. Q. Xie, S. Inoue, Y. Kumagai, A. Koukitu, and Z. Sitar, Appl Phys Express **5** (12), 3 (2012).

[38] Y. Muramoto, M. Kimura, and S. Nouda, Semicond Sci Tech **29** (8), 8 (2014).

[39] H. Hirayama, T. Yatabe, N. Noguchi, and N. Kamata, Electr Commun Jpn **93** (3), 24 (2010).

[40] C. Pernot, S. Fukahori, T. Inazu, T. Fujita, M. Kim, Y. Nagasawa, A. Hirano, M. Ippommatsu, M. Iwaya, S. Kamiyama, I. Akasaki, and H. Amano, Phys Status Solidi A **208** (7), 1594 (2011).

[41] S. Nagai, K. Yamada, A. Hirano, M. Ippommatsu, M. Ito, N. Morishima, K. Aosaki, Y. Honda, H. Amano, and I. Akasaki, Jpn. J. Appl. Phys. **55** (8), 7 (2016).

[42] J. H. Park, G. B. Lin, D. Y. Kim, J. W. Lee, J. Cho, J. Kim, J. Lee, Y. I. Kim, Y. Park, E. F. Schubert, and J. K. Kim, Opt. Express **23** (12), 15398 (2015).

[43] F. Mehnke, C. Kuhn, J. Stellmach, T. Kolbe, N. Lobo-Ploch, J. Rass, M. A. Rothe, C. Reich, N. Ledentsov, M. Pristovsek, T. Wernicke, and M. Kneissl, J Appl Phys **117** (19), 5 (2015).

[44] M. Jo, N. Maeda, and H. Hirayama, Appl Phys Express **9** (1), 3 (2016).

[45] M. Shatalov, R. Jain, A. Dobrinsky, W. H. Sun, Y. Bilenko, J. W. Yang, M. Shur, and R. Gaska, in *Gallium Nitride Materials and Devices X*, edited by J. I. Chyi, H. Fujioka, and H. Morkoc (Spie-Int Soc Optical Engineering, Bellingham, 2015), Vol. 9363.

[46] M. Shatalov, W. H. Sun, R. Jain, A. Lunev, X. H. Hu, A. Dobrinsky, Y. Bilenko, J. W. Yang, G. A. Garrett, L. E. Rodak, M. Wraback, M. Shur, and R. Gaska, Semicond Sci Tech **29** (8), 6 (2014).

[47] J. Rass, T. Kolbe, N. L. Ploch, T. Wernicke, F. Mehnke, C. Kuhn, J. Enslin, M. Guttmann, C. Reich, A. Mogilatenko, J. Glaab, C. Stoelmacker, M. Lapeyrade, S. Einfeldt, M. Weyers, and M. Kneissl, in *Gallium Nitride Materials and Devices X*, edited by J. I. Chyi, H. Fujioka, and H. Morkoc (Spie-Int Soc Optical Engineering, Bellingham, 2015), Vol. 9363.

[48] A. Fujioka, K. Asada, H. Yamada, T. Ohtsuka, T. Ogawa, T. Kosugi, D. Kishikawa, and T. Mukai, Semicond Sci Tech **29** (8), 5 (2014).

[49] C. G. Moe, J. R. Grandusky, J. F. Chen, K. Kitamura, M. C. Mendrick, M. Jamil, M. Toita, S. R. Gibb, and L. J. Schowalter, in *Gallium Nitride Materials and Devices Ix*, edited by J. I. Chyi, Y. Nanishi, H. Morkoc et al. (Spie-Int Soc Optical Engineering, Bellingham, 2014), Vol. 8986.

[50] C. Pernot, M. Kim, S. Fukahori, T. Inazu, T. Fujita, Y. Nagasawa, A. Hirano, M. Ippommatsu, M. Iwaya, S. Kamiyama, I. Akasaki, and H. Amano, Appl Phys Express **3** (6), 3 (2010).

[51] A. Fujioka, T. Misaki, T. Murayama, Y. Narukawa, and T. Mukai, Appl Phys Express **3** (4), 3 (2010).

[52] N. Maeda, H. Hirayama, and Ieee, *Improvement of Light-Extraction Efficiency of Deep-UV LEDs using Transparent p-AlGaN Contact Layer*. (Ieee, New York, 2013).

[53] S. Tan, T. Egawa, X. D. Luo, L. Sun, Y. H. Zhu, and J. C. Zhang, J Phys D Appl Phys **49** (12), 5 (2016).

[54] T. Kinoshita, T. Obata, T. Nagashima, H. Yanagi, B. Moody, S. Mita, S. Inoue, Y. Kumagai, A. Koukitu, and Z. Sitar, Appl Phys Express **6** (9), 3 (2013).

[55] D. Jena, J. Simon, A. Wang, Y. Cao, K. Goodman, J. Verma, S. Ganguly, G. W. Li, K. Karda, V. Protasenko, C. X. Lian, T. Kosel, P. Fay, and H. L. Xing, Phys Status Solidi A **208** (7), 1511 (2011).

[56] A. Fujioka, K. Asada, H. Yamada, T. Ohtsuka, T. Ogawa, T. Kosugi, D. Kishikawa, and T. Mukai, in *Gallium Nitride Materials and Devices X*, edited by J. I. Chyi, H. Fujioka, and H. Morkoc (Spie-Int Soc Optical Engineering, Bellingham, 2015), Vol. 9363.

[57] N. Maeda and H. Hirayama, in *Physica Status Solidi C: Current Topics in Solid State Physics, Vol 10, No 11*, edited by H. Yamaguchi and K. Kumakura (Wiley-V C H Verlag Gmbh, Weinheim, 2013), Vol. 10, pp. 1521.

[58] H. Hirayama, N. Maeda, S. Fujikawa, S. Toyoda, and N. Kamata, Jpn. J. Appl. Phys. **53** (10), 10 (2014).

[59] H. Hirayama, S. Fujikawa, and N. Kamata, Electr Commun Jpn **98** (5), 1 (2015).

[60] Michael Kneissl, Jens Rass, and SpringerLink (Online service), in *Springer Series in Materials Science,* (2017), pp. 1 online resource (XIX.

[61] M. A. Khan, Phys Status Solidi A **203** (7), 1764 (2006).

[62] Y. Taniyasu, M. Kasu, and T. Makimoto, Nature **441** (7091), 325 (2006).

[63] B. Neuschl, K. Thonke, M. Feneberg, R. Goldhahn, T. Wunderer, Z. Yang, N. M. Johnson, J. Xie, S. Mita, A. Rice, R. Collazo, and Z. Sitar, Appl Phys Lett **103** (12) (2013).

[64] J. H. Park, J. W. Lee, D. Y. Kim, J. Cho, E. F. Schubert, J. Kim, J. Lee, Y. I. Kim, Y. Park, and J. K. Kim, J Appl Phys **119** (2) (2016).

[65] M. H. Kim, M. F. Schubert, Q. Dai, J. K. Kim, E. F. Schubert, J. Piprek, and Y. Park, Appl Phys Lett **91** (18) (2007).

[66] K. B. Nam, J. Li, M. L. Nakarmi, J. Y. Lin, and H. X. Jiang, Appl Phys Lett **84** (25), 5264 (2004).

[67] B. Cheng, S. Choi, J. E. Northrup, Z. Yang, C. Knollenberg, M. Teepe, T. Wunderer, C. L. Chua, and N. M. Johnson, Appl Phys Lett **102** (23) (2013).

[68] M. Bosi and R. Fornari, J Cryst Growth **265** (3-4), 434 (2004).

[69] Y. Guo, X. L. Liu, H. P. Song, A. L. Yang, X. Q. Xu, G. L. Zheng, H. Y. Wei, S. Y. Yang, Q. S. Zhu, and Z. G. Wang, Appl. Surf. Sci. **256** (10), 3352 (2010).

[70] J. H. Ryou, P. D. Yoder, J. P. Liu, Z. Lochner, H. Kim, S. Choi, H. J. Kim, and R. D. Dupuis, IEEE J. Sel. Top. Quantum Electron. **15** (4), 1080 (2009).

[71] Z. Gong, S. R. Jin, Y. J. Chen, J. McKendry, D. Massoubre, I. M. Watson, E. Gu, and M. D. Dawson, J Appl Phys **107** (1), 6 (2010).

[72] P. G. Eliseev, P. Perlin, J. Y. Lee, and M. Osinski, Appl Phys Lett **71** (5), 569 (1997).

[73] L. Dai, B. Zhang, J. Y. Lin, and H. X. Jiang, J Appl Phys **89** (9), 4951 (2001).

[74] S. X. Jin, J. Li, J. Y. Lin, and H. X. Jiang, Appl Phys Lett **77** (20), 3236 (2000).

[75] T. I. Kim, Y. H. Jung, J. Z. Song, D. Kim, Y. H. Li, H. S. Kim, I. S. Song, J. J. Wierer, H. A. Pao, Y. G. Huang, and J. A. Rogers, Small **8** (11), 1643 (2012).

[76] P. F. Tian, J. J. D. McKendry, Z. Gong, B. Guilhabert, I. M. Watson, E. D. Gu, Z. Z. Chen, G. Y. Zhang, and M. D. Dawson, Appl Phys Lett **101** (23) (2012).

[77] F. Olivier, S. Tirano, L. Dupre, B. Aventurier, C. Largeron, and F. Templier, J Lumin **191**, 112 (2017).

[78] D. Hwang, A. Mughal, C. D. Pynn, S. Nakamura, and S. P. DenBaars, Appl Phys Express **10** (3) (2017).

[79] P. Royo, R. P. Stanley, M. Ilegems, K. Streubel, and K. H. Gulden, J Appl Phys **91** (5), 2563 (2002).

[80] S. S. Konoplev, K. A. Bulashevich, and S. Y. Karpov, Phys Status Solidi A **215** (10) (2018).

[81] S. P. Lu, W. Liu, Z. H. Zhang, S. T. Tan, Z. G. Ju, Y. Ji, X. L. Zhang, Y. P. Zhang, B. B. Zhu, Z. Kyaw, N. Hasanov, X. W. Sun, and H. V. Demir, Opt. Express **22** (26), 32200 (2014).

[82] Z. Gong, H. X. Zhang, E. Gu, C. Griffin, M. D. Dawson, V. Poher, G. Kennedy, P. M. W. French, and M. A. A. Neil, Ieee T Electron Dev **54** (10), 2650 (2007).

[83] J. Cho, E. F. Schubert, and J. K. Kim, Laser Photonics Rev **7** (3), 408 (2013).

[84] J. J. D. McKendry, R. P. Green, A. E. Kelly, Z. Gong, B. Guilhabert, D. Massoubre, E. D. Gu, and M. D. Dawson, Ieee Photonic Tech L **22** (18), 1346 (2010).

[85] Z. J. Lu, P. F. Tian, H. Chen, I. Baranowski, H. Q. Fu, X. Q. Huang, J. Montes, Y. Y. Fan, H. Y. Wang, X. Y. Liu, R. Liu, and Y. J. Zhao, Opt. Express **25** (15), 17971 (2017).

[86] H. Qian, S. Zhao, S. Z. Cai, and T. Zhou, IEEE Photonics J. **7** (3), 8 (2015).

[87] L. X. Zhao, S. C. Zhu, C. H. Wu, C. Yang, Z. G. Yu, H. Yang, and L. Liu, Sci. China-Phys. Mech. Astron. **59** (10), 10 (2016).

[88] X. Y. Liu, P. F. Tian, Z. X. Wei, S. Y. Yi, Y. X. Huang, X. L. Zhou, Z. J. Qiu, L. G. Hu, Z. L. Fang, C. X. Cong, L. R. Zheng, and R. Liu, IEEE Photonics J. **9** (6), 9 (2017).

[89] P. F. Tian, X. Y. Liu, S. Y. Yi, Y. X. Huang, S. L. Zhang, X. L. Zhou, L. G. Hu, L. R. Zheng, and R. Liu, Opt. Express **25** (2), 1193 (2017).

[90] E. Y. Xie, X. Y. He, M. S. Islim, A. A. Purwita, J. J. D. McKendry, E. D. Gu, H. Haas, and M. D. Dawson, J. Lightwave Technol. **37** (4), 1180 (2019).

[91] P. F. Tian, Z. Y. Wu, X. Y. Liu, Z. L. Fang, S. L. Zhang, X. L. Zhou, K. F. Liu, M. G. Liu, S. J. Chen, C. Y. Lee, C. X. Cong, L. G. Hu, Z. J. Qiu, L. R. Zheng, and R. Liu, Appl Phys Express **11** (4), 4 (2018).

[92] Z. W. Zheng, H. Yu, B. C. Ren, L. M. Zhou, H. Y. Fu, X. Cheng, L. Y. Ying, H. Long, and B. P. Zhang, ECS J. Solid State Sci. Technol. **6** (9), R135 (2017).

[93] M. S. Islim, R. X. Ferreira, X. Y. He, E. Y. Xie, S. Videv, S. Viola, S. Watson, N. Bamiedakis, R. V. Penty, I. H. White, A. E. Kelly, E. D. Gu, H. Haas, and M. D. Dawson, Photonics Res. **5** (2), A35 (2017).

[94] J. J. D. McKendry, D. Massoubre, S. L. Zhang, B. R. Rae, R. P. Green, E. Gu, R. K. Henderson, A. E. Kelly, and M. D. Dawson, J. Lightwave Technol. **30** (1), 61 (2012).

[95] J. Day, J. Li, D. Y. C. Lie, C. Bradford, J. Y. Lin, and H. X. Jiang, Appl Phys Lett **99** (3) (2011).

[96] X. Zhang, P. A. Li, X. B. Zou, J. M. Jiang, S. H. Yuen, C. W. Tang, and K. M. Lau, Ieee Photonic Tech L **31** (11), 865 (2019).

[97] J. G. Um, D. Y. Jeong, Y. Jung, J. K. Moon, Y. H. Jung, S. Kim, S. H. Kim, J. S. Lee, and J. Jang, Adv. Electron. Mater. **5** (3), 8 (2019).

[98] F. W. Gou, E. L. Hsiang, G. J. Tan, P. T. Chou, Y. L. Li, Y. F. Lan, and S. O. Wu, Opt. Express **27** (12), A746 (2019).

[99] S. L. Zhang, J. J. D. McKendry, Z. Gong, B. R. Rae, S. Watson, E. Y. Xie, P. F. Tian, E. Richardson, E. D. Gu, Z. Z. Chen, G. Y. Zhang, A. E. Kelly, R. K. Henderson, M. D. Dawson, and Ieee, in *2012 Ieee Photonics Conference* (Ieee, New York, 2012), pp. 435.

[100] C. J. Chen, H. C. Chen, J. H. Liao, C. J. Yu, and M. C. Wu, Ieee J Quantum Elect **55** (2), 6 (2019).

[101] C. M. Kang, D. J. Kong, J. P. Shim, S. Kim, S. B. Choi, J. Y. Lee, J. H. Min, D. J. Seo, S. Y. Choi, and D. S. Lee, Opt. Express **25** (3), 2489 (2017).

[102] K. Ding, V. Avrutin, N. Izyumskaya, U. Ozgur, and H. Morkoc, Appl. Sci.-Basel **9** (6), 15 (2019).

[103] V. Poher, N. Grossman, G. T. Kennedy, K. Nikolic, H. X. Zhang, Z. Gong, E. M. Drakakis, E. Gu, M. D. Dawson, P. M. W. French, P. Degenaar, and M. A. A. Neil, J Phys D Appl Phys **41** (9) (2008).

[104] Z. Gong, B. Guilhabert, Z. Chen, and M. D. Dawson, Nano Res. **7** (12), 1849 (2014).

[105] Z. Gong, E. Gu, S. R. Jin, D. Massoubre, B. Guilhabert, H. X. Zhang, M. D. Dawson, V. Poher, G. T. Kennedy, P. M. W. French, and M. A. A. Neil, J Phys D Appl Phys **41** (9), 6 (2008).

[106] K. Zhang, D. Peng, K. M. Lau, and Z. J. Liu, J. Soc. Inf. Disp. **25** (4), 240 (2017).

[107] F. W. Gou, E. L. Hsiang, G. J. Tan, Y. F. Lan, C. Y. Tsai, and S. T. Wu, J. Soc. Inf. Disp. **27** (4), 199 (2019).

[108] C. W. Jeon, H. W. Choi, E. R. Gu, and M. D. Dawson, Ieee Photonic Tech L **16** (11), 2421 (2004).

[109] B. Guilhabert, E. Richardson, D. Massoubre, E. Gu, I. M. Watson, M. D. Dawson, and Ieee, *Maskless Fabrication of GaN-Based Light-Emitting Diodes*. (Ieee, New York, 2010), pp.649.

[110] D. Elfstrom, B. Guilhabert, J. McKendry, S. Poland, Z. Gong, D. Massoubre, E. Richardson, B. R. Rae, G. Valentine, G. Blanco-Gomez, E. Gu, J. M. Cooper, R. K. Henderson, and M. D. Dawson, Opt. Express **17** (26), 23522 (2009).

[111] V. Poher, N. Grossman, G. T. Kennedy, K. Nikolic, H. X. Zhang, Z. Gong, E.

M. Drakakis, E. Gu, M. D. Dawson, P. M. W. French, P. Degenaar, and M. A. A. Neil, J Phys D Appl Phys **41** (9), 9 (2008).

[112] L. Zhu, P. T. Lai, and H. W. Choi, Ieee Photonic Tech L **23** (15), 1067 (2011).

[113] C. W. Jeon, E. Gu, C. Liu, J. M. Girkin, and M. D. Dawson, Ieee Photonic Tech L **17** (9), 1887 (2005).

[114] L. Zhu, P. T. Lai, and H. W. Choi, in *Physica Status Solidi C: Current Topics in Solid State Physics, Vol 7, No 7-8* (Wiley-V C H Verlag Gmbh, Weinheim, 2010), Vol. 7.

[115] Show Report https://www.ledinside.com/showreport/2015/10/hpl_outlook_for_uv_led_curing_market, (LEDinside, 2015).

[116] Tingzhu Wu, Chin-Wei Sher, Yue Lin, Chun-Fu Lee, Shijie Liang, Yijun Lu, Sung-Wen Huang Chen, Weijie Guo, Hao-Chung Kuo, and Zhong Chen, Applied Sciences **8** (9) (2018).

[117] M. P. Lin, C. J. Chen, L. W. Shan, and M. C. Wu, Solid-State Electron. **135**, 49 (2017).

[118] N. L. Ploch, H. Rodriguez, C. Stolmacker, M. Hoppe, M. Lapeyrade, J. Stellmach, F. Mehnke, T. Wernicke, A. Knauer, V. Kueller, M. Weyers, S. Einfeldt, and M. Kneissl, Ieee T Electron Dev **60** (2), 782 (2013).

[119] S. X. Jin, J. Shakya, J. Y. Lin, and H. X. Jiang, Appl Phys Lett **78** (22), 3532 (2001).

[120] S. X. Jin, J. Li, J. Z. Li, J. Y. Lin, and H. X. Jiang, Appl Phys Lett **76** (5), 631 (2000).

[121] X. Guo and E. F. Schubert, J Appl Phys **90** (8), 4191 (2001).

[122] C. Shen, T. K. Ng, Y. Yang, D. Cha, and B. S. Ooi, in *2013 IEEE Photonics Conference (IPC)* (2013), pp. 174.

[123] E. Y. Xie, Z. Z. Chen, P. R. Edwards, Z. Gong, N. Y. Liu, Y. B. Tao, Y. F. Zhang, Y. J. Chen, I. M. Watson, E. Gu, R. W. Martin, G. Y. Zhang, and M. D. Dawson, J Appl Phys **112** (1) (2012).

[124] H. P. Zhao, R. A. Arif, Y. K. Ee, and N. Tansu, Ieee J Quantum Elect **45** (1-2), 66 (2009).

[125] M. Meneghini, N. Trivellin, G. Meneghesso, E. Zanoni, U. Zehnder, and B. Hahn, J Appl Phys **106** (11) (2009).

[126] V. Fiorentini, F. Bernardini, and O. Ambacher, Appl Phys Lett **80** (7), 1204 (2002).

[127] J. Piprek and S. Nakamura, Iee P-Optoelectron **149** (4), 145 (2002).

[128] I. Vurgaftman and J. R. Meyer, J Appl Phys **94** (6), 3675 (2003).

[129] E. Fred Schubert, *Light-Emitting Diodes*. (Cambridge University Press,, Cambridge, 2006), p.1 online resource (432 p.).

[130] H. W. Choi, M. D. Dawson, P. R. Edwards, and R. W. Martin, Appl Phys Lett **83** (22), 4483 (2003).

[131] H. Y. Ryu, H. S. Kim, and J. I. Shim, Appl Phys Lett **95** (8) (2009).

[132] T. Deguchi, A. Shikanai, K. Torii, T. Sota, S. Chichibu, and S. Nakamura, Appl Phys Lett **72** (25), 3329 (1998).

[133] H. P. Zhao, G. Y. Liu, R. A. Arif, and N. Tansu, Solid-State Electron. **54** (10), 1119 (2010).

[134] H. P. Zhao, G. Y. Liu, J. Zhang, R. A. Arif, and N. Tansu, J. Disp. Technol. **9** (4), 212 (2013).

[135] W. W. Guo, F. J. Xu, Y. H. Sun, L. Lu, Z. X. Qin, T. J. Yu, X. Q. Wang, and B. Shen, Superlattices Microstruct. **100**, 941 (2016).

[136] L. F. He, W. Zhao, K. Zhang, C. G. He, H. L. Wu, N. Y. Liu, W. D. Song, Z. T. Chen, and S. T. Li, Opt. Lett. **43** (3), 515 (2018).

[137] Z. H. Zhang, C. S. Chu, C. H. Chiu, T. C. Lu, L. P. Li, Y. H. Zhang, K. K. Tian, M. Q. Fang, Q. Sun, H. C. Kuo, and W. G. Bi, Opt. Lett. **42** (21), 4533 (2017).

[138] Y. Shen, Y. W. Zhang, L. Yu, K. Li, H. Pi, J. S. Diao, W. X. Hu, W. D. Song, C. Z. Zhang, and S. T. Li, J. Disp. Technol. **11** (9), 677 (2015).

[139] M. L. Nakarmi, N. Nepal, C. Ugolini, T. M. Altahtamouni, J. Y. Lin, and H. X. Jiang, Appl Phys Lett **89** (15), 3 (2006).

[140] T. Oto, R. G. Banal, K. Kataoka, M. Funato, and Y. Kawakami, Nat. Photonics **4** (11), 767 (2010).

[141] Y. R. Chen, Z. W. Zhang, G. Q. Miao, H. Jiang, Z. M. Li, and H. Song, J. Alloy. Compd. **820**, 7 (2020).

[142] W. Z. Tawfik, C. M. M. Kumar, J. Park, S. K. Shim, H. Lee, J. Lee, J. H. Han, S. W. Ryu, N. Lee, and J. K. Lee, J. Mater. Chem. C **7** (37), 11540 (2019).

[143] Y. X. Wang, X. Rong, S. Ivanov, V. Jmerik, Z. Y. Chen, H. Wang, T. Wang, P. Wang, P. Jin, Y. N. Chen, V. Kozlovsky, D. E. Sviridov, M. Zverev, E. Zhdanova, N. Gamov, V. Studenov, H. Miyake, H. W. Li, S. P. Guo, X. L. Yang, F. J. Xu, T. J. Yu, Z. X. Qin, W. K. Ge, B. Shen, and X. Q. Wang, Adv. Opt. Mater. **7** (10), 7 (2019).

[144] T. Hayashi, Y. Kawase, N. Nagata, T. Senga, S. Iwayama, M. Iwaya, T. Takeuchi, S. Kamiyama, I. Akasaki, and T. Matsumoto, Sci Rep **7**, 5 (2017).

[145] F. Tabataba-Vakili, T. Wunderer, M. Kneissl, Z. H. Yang, M. Teepe, M. Batres, M. Feneberg, B. Vancil, and N. M. Johnson, Appl Phys Lett **109** (18), 5 (2016).

[146] S. V. Ivanov, V. N. Jmerik, D. V. Nechaev, V. I. Kozlovsky, and M. D. Tiberi, Phys Status Solidi A **212** (5), 1011 (2015).

[147] F. Fukuyo, S. Ochiai, H. Miyake, K. Hiramatsu, H. Yoshida, and Y. Kobayashi, Jpn. J. Appl. Phys. **52** (1), 3 (2013).

[148] T. Matsumoto, S. Iwayama, T. Saito, Y. Kawakami, F. Kubo, and H. Amano, Opt. Express **20** (22), 24320 (2012).

[149] V. N. Jmerik, D. V. Nechaev, A. A. Toropov, E. A. Evropeitsev, V. I. Kozlovsky, V. P. Martovitsky, S. Rouvimov, and S. V. Ivanov, Appl Phys Express **11** (9), 5 (2018).

[150] X. Rong, X. Q. Wang, S. V. Ivanov, X. H. Jiang, G. Chen, P. Wang, W. Y. Wang, C. G. He, T. Wang, T. Schulz, M. Albrecht, V. N. Jmerik, A. A. Toropov, V. V. Ratnikov, V. I. Kozlovsky, V. P. Martovitsky, P. Jin, F. J. Xu, X. L. Yang, Z. X. Qin, W. K. Ge, J. J. Shi, and B. Shen, Adv. Mater. **28** (36), 7978 (2016).

[151] S. T. Yoo, B. So, H. I. Lee, O. Nam, and K. C. Park, AIP Adv. **9** (7), 5 (2019).

[152] Y. J. Park, T. Detchprohm, K. Mehta, J. L. Wang, H. Jeong, Y. S. Liu, P. Chen, S. Wang, S. C. Shen, P. D. Yoder, F. Ponce, and R. D. Dupuis, in *Vertical-Cavity Surface-Emitting Lasers Xxiii*, edited by K. D. Choquette and L. A. Graham (Spie-Int Soc Optical Engineering, Bellingham, 2019), Vol. 10938.

[153] N. A. Gamov, E. V. Zhdanova, M. M. Zverev, D. V. Peregoudov, V. B. Studenov, A. V. Mazalov, V. A. Kureshov, D. R. Sabitov, A. A. Padalitsa, and A. A. Marmalyuk, Quantum Electron. **45** (7), 601 (2015).

[154] T. Wunderer, J. Jeschke, Z. H. Yang, M. Teepe, M. Batres, B. Vancil, and N. Johnson, Ieee Photonic Tech L **29** (16), 1344 (2017).

[155] A. Khan, K. Balakrishnan, and T. Katona, Nat. Photonics **2** (2), 77 (2008).

[156] A. Hospodkova, T. Hubacek, J. Oswald, J. Pangrac, K. Kuldova, M. Hyvl, F. Dominec, G. Ledoux, and C. Dujardin, Phys Status Solidi B **255** (5) (2018).

[157] A. Hospodkova, J. Oswald, M. Zikova, J. Pangrac, K. Kuldova, K. Blazek, G. Ledoux, C. Dujardin, and M. Nikl, J Appl Phys **121** (21) (2017).

[158] T. Hubacek, A. Hospodkova, K. Kuldova, J. Oswald, J. Pangrac, V. Jary, F. Dominec, M. S. Zikova, F. Hajek, E. Hulicius, A. Vetushka, G. Ledoux, C. Dujardin, and M. Nikl, Crystengcomm **21** (2), 356 (2019).

[159] J. Yang, D. G. Zhao, D. S. Jiang, P. Chen, J. J. Zhu, Z. S. Liu, L. C. Le, X. G. He, X. J. Li, H. Wang, H. Yang, and U. Jahn, J Vac Sci Technol A **32** (5) (2014).

[160] P. S. Vergeles, N. M. Shmidt, E. E. Yakimov, and E. B. Yakimov, Phys Status

Solidi C **8** (4) (2011).

[161] F. Tabataba-Vakili, T. Wunderer, M. Kneissl, Z. H. Yang, M. Teepe, M. Batres, M. Feneberg, B. Vancil, and N. M. Johnson, Appl Phys Lett **109** (18) (2016).

[162] D. Drouin, A. R. Couture, D. Joly, X. Tastet, V. Aimez, and R. Gauvin, Scanning **29** (3), 92 (2007).

[163] M. Leyer, J. Stellmach, C. Meissner, M. Pristovsek, and M. Kneissl, J Cryst Growth **310** (23), 4913 (2008).

[164] D. Holec, P. M. F. J. Costa, M. J. Kappers, and C. J. Humphreys, J Cryst Growth **303** (1), 314 (2007).